CARDIAC FUNCTION MONITORING DURING VENOARTERIAL EXTRA-CORPOREAL MEMBRANE OXYGENATION IN THE INTENSIVE CARE UNIT

MAAIKE WÖSTEN

Cardiac function monitoring during venoarterial extracorporeal membrane oxygenation in the intensive care unit

Maaike Wösten,   November 2023

Master thesis

Applied Mathematics   Systems, Analysis and Computational Sciences
Technical Medicine   Medical Sensing and Stimulation

University of Twente

Mathematics of Systems Theory (MAST)
Cardiovascular and Respiratory Physiology (CRPH)

University Medical Center Utrecht

Intensive Care Center

Graduation Committee

Chair and Technical supervisor AM   Prof. dr. H. Zwart
Technical supervisor TM   Dr. ir. L. Fresiello
Medical supervisor   Prof. dr. D.W. Donker
Process supervisor   Drs. B.J.C.C. Sweep
External member   Prof. dr. ir. B.J. Geurts

UNIVERSITY OF TWENTE.   **UMC Utrecht**

Contents

Abbreviations

AS	Aortic valve stenosis
AV	Aortic valve
AVA	Aortic valve area
BPM	Beats per minute
BSA	Body surface area
C	Compliance
CI	Cardiac index
CO	Cardiac output
CVP	Central venous pressure
dLVOT	Diameter of the left ventricular outflow tract
EDPVR	End-diastolic pressure volume relation
ESPVR	End-systolic pressure volume relation
HLM	Heart-lung machine
HR	Heart rate
ICU	Intensive care unit
LoA	Limits of Agreement
LV	Left ventricle
LVAD	Left ventricular assist device
LVEF	Left ventricular ejection fraction
LVOT	Left ventricular outflow tract
LVOTacc	Left ventricular outflow tract mean systolic acceleration
MAP	Mean arterial pressure
mPAP	Mean pulmonary artery pressure
MR	Mitral valve regurgitation
MV	Mitral valve
nRMSE	Normalized root mean squared error
OR	Operating room
PP	Pulse pressure
PV loop	Pressure-volume loop
PWA	Pulse wave analysis
PWP	Pulmonary wedge pressure
R	Resistance
RMSE	Root mean squared error
SBP	Systolic blood pressure
SV	Stroke volume
TEE	Transesophageal echocardiography
TTE	Transthoracic echocardiography
UMCU	University Medical Centre Utrecht
UT	University of Twente
VA ECMO	Venoarterial extracorporeal membrane oxygenation
VTI	Velocity time integral
WK	Windkessel

Abstract

Background: Venoarterial extracorporeal membrane oxygenation (VA ECMO) is a mechanical support modality that can be used to quickly restore the systemic circulation in patients with cardiogenic shock. However, the clinical care management of patients supported with VA ECMO is complex, mainly due to the interaction between the ECMO circuit and the patient's native hemodynamics. To improve this clinical management, it is important to gain insight in the native function of the left ventricle (LV). This thesis therefore describes the application of a lumped parameter model to continuously monitor LV flow using arterial blood pressure during VA ECMO.

Methods: Cardiovascular simulators and clinical data were used to evaluate the LV flow calculated using the two-element Windkessel model. For the cardiovascular simulators, LV flow was compared using the stroke volume (SV) and normalized root mean squared error (nRMSE). In the clinical data, the calculated SV from the left ventricle was compared to the echocardiographic measurement of SV. In addition, to compare the two-element Windkessel model to a model described by linearized one-dimensional Navier-Stokes equations, transfer functions were derived and compared using Bode plots.

Results: In two of the three cardiovascular simulators the calculation of the LV flow resulted in an average error in SV below 12%. For the third simulator, the average error was larger with an average of 26%. The nRMSE showed large differences between the different simulators, varying from 0.1 to 2.6. In the clinical data, using current patient specific parameters, the average error in stroke volume was 0.88 mL. Using patient specific parameters that are continuously estimated, the error in SV becomes larger. Comparison of the two-element Windkessel model to linearized one-dimensional Navier-Stokes equations showed no large differences for low frequencies.

Conclusion: Application of the two-element Windkessel model can be used to accurately determine SV during VA ECMO in two of the three cardiovascular simulators and in clinical data, using known patient specific parameters. We also showed that for low frequencies the linearized one-dimensional Navier-Stokes equations will not lead to large improvements in the flow calculations from arterial blood pressure. Further studies should show if more comprehensive models can improve the calculated LV flow waveform and should focus on improving the accuracy of the continuous estimation of patient specific parameters.

1 General introduction

Cardiogenic shock is the main cause of mortality in hospitalized patients with acute myocardial infarction. Between 3 and 13% of the patients with acute myocardial infarction develops cardiogenic shock, a state of end-organ hypoperfusion caused by a low cardiac output (CO) due to cardiac failure [1], [2]. It is estimated that about 50-60% of these patients survive without mechanical circulatory support. Another 15-25% of these patients could benefit from circulatory support, increasing the number of survivors [1]. Venoarterial extracorporeal membrane oxygenation (VA ECMO) is a mechanical support modality used to quickly restore the systemic circulation in a patient with cardiogenic shock, ultimately resulting in restored tissue perfusion and oxygenation [3], [4]. After the initial stabilization, the aim for the patient is to recover and wean from VA ECMO, or to use VA ECMO as bridge to transplant or long term mechanical support such as a left ventricular assist device (LVAD) [5]–[7]. Although VA ECMO supports patients in cardiogenic shock, over time the support also increases the risk of complications such as bleeding, limb ischemia and thrombosis [4]. The duration of a VA ECMO run can vary between one day to weeks. In total, about half of these critically ill patients can be successfully weaned from VA ECMO, a small part of the other patients receive heart transplantation or an LVAD. Despite the fact that the use of VA ECMO rapidly increased over the past decade, mortality within one year remains high [8], [9].

The clinical care management of a patient supported with VA ECMO is complex, mainly due to a large number of patient- and technology-related factors and mutual interaction that need to be considered. This mainly involves the complex interaction between the ECMO circuit and the patient's hemodynamics. The most commonly used configuration for VA ECMO outside the operating room is femoral cannulation. In this configuration deoxygenated blood is drained from the inferior vena cava and pumped through an oxygenator. The blood is returned with a continuous flow into the arterial circulation through a cannula in the femoral artery [3], [4]. The retrograde flow of oxygenated blood from the ECMO mixes in the aorta with the pulsatile flow from the left ventricle (LV) in the so called watershed zone. The drainage of blood from the venous system causes the venous return and therefore the preload to decrease. The return of oxygenated blood into the aorta may increase the afterload for the LV. An increased afterload can contribute to the deterioration of LV function, eventually leading to dilatation of the LV [4], [5]. Additional unloading devices can be applied to unload the LV, such as an intra-aortic balloon pump (IABP) or a ventriculo-aortic axial pump (Impella) [10]. The management of a patient supported with VA ECMO is further complicated by the many therapeutic measures that are considered, i.e. changing ECMO settings and administration of drugs or fluids.

1.1 Research aim

To improve the management of patients supported with VA ECMO in the intensive care unit (ICU) it is important to gain insight into the condition of the heart. The aim of VA ECMO support is to recover cardiac function and more specific, LV function. However, there is currently no accessible and accurate parameter to continuously describe LV function in patients supported with VA ECMO, since the available parameters are strongly influenced by ECMO flow, vascular resistance and arterial compliance. Hence, a method is needed to continuously distinguish between the contribution of the VA ECMO and the LV to the total hemodynamics of the patient. In addition, it is valuable to identify the values for resistance and compliance for a specific patient. Therefore, in this thesis we study the application of a simplified cardiovascular model, describing the relation of LV and ECMO flow with arterial blood pressure. Eventually, continuously monitoring the LV function will give a better and faster insight into the deterioration or improvement of the LV during VA ECMO.

Ultimately, it would be beneficial to support the physician with a decision support model that can interpret and weigh all different parameters to suggest the best setting for ECMO flow and additionally drugs and fluid interventions. The design of a monitoring system for LV function will be the first step towards a decision support model. The aim of this study is therefore to demonstrate the application of a simple mathematical model to continuously monitor LV flow during VA ECMO.

2 Background

Currently, a multidisciplinary team with several medical specialists and perfusionists is involved in the daily management of patients supported with VA ECMO. Daily monitoring is based on a combination of parameters, including arterial and venous saturation, lactate, diuresis, arterial pressures and pulmonary pressures when available. In daily management, a balance is desired between reducing the burden on the heart and maintaining sufficient tissue perfusion. For optimal treatment of the patient, this balance should be maintained at all times. Although there are guidelines defining target values per parameter, the ideal constellation remains difficult to find. It is extremely complex to weigh and interpret all parameters in the dynamic context of an individual patient.

While systemic perfusion is often sufficiently managed during VA ECMO, LV unloading is regularly insufficient [10]. To provide the optimal condition for the heart it is important to gain insight in the function of and burden on the LV. Ideally, we want to determine the native contractility of the LV, evaluating the current and potential function of the heart. This native contractility describes the intrinsic ability of the ventricle to create a force, independent of other factors such as preload and afterload. The contractility can be described using the pressure-volume (PV) loop. Figure 1 shows an example of a PV loop, describing the pressure and the volume in the LV during the cardiac cycle. Changing the loading conditions for the same contractility changes the PV loop, the end-systolic points however, remain on the same line. This line is the end-systolic pressure volume relation (ESPVR). The slope of this relation is Emax, the maximum elastance. Emax increases for increased intrinsic contractility. The Ees is the elastance at the moment of aortic valve closure, which occurs very shortly after maximum elastance. Therefore Ees is comparable to Emax. The advantage of Ees is that it is sensitive for changes in contractility, but is insensitive to changes in preload and afterload. However, measurement of Ees in patients supported with VA ECMO is challenging. Most measures of LV function largely depend on the loading conditions of the heart [11], [12]. In patients supported with VA ECMO, the LV contractility is often estimated using the left ventricular ejection fraction (LVEF), or by monitoring the pulse pressure (PP) [13].

LVEF is defined as the percentage of blood volume that is ejected by the LV, compared to the volume of the ventricle at the end of diastole. Echocardiography is used to determine the LVEF. However, just as most Ees estimates, LVEF does not exclusively depend on the native contractility of the LV. An isolated decrease of preload or increase of afterload will result in a decrease of LVEF. Hence, a change in LVEF is not necessarily caused by a change in the contractility of the LV. Therefore, exclusively using the load-dependent LVEF as a measure for contractility can lead to an incorrect impression of the LV function [13]–[15].

Next to LVEF, PP is also used as an indicator of the LV function in clinical practice. PP is the difference between systolic and diastolic blood pressure. Since the ECMO flow is non-pulsatile, the PP is only caused by the interaction of the native contractility of the heart with the arterial system. However, the PP depends on many variables, such as systemic vascular resistance, arterial compliance, left ventricular elastance, heart rate and blood volume [16]. Although several studies showed a
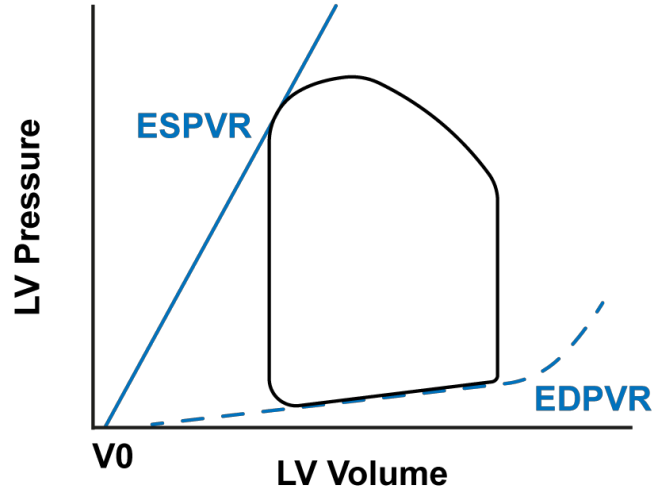
Figure 1: Pressure-volume loop, with the solid blue line indicating the end-systolic pressure volume relation (ESPVR) and dashed blue curve the end-disatolic pressure volume relation (EDPVR).

prognostic value for PP in VA ECMO, PP was never studied as a monitoring parameter for cardiac function [6], [17]–[20]. Just as for LVEF, using solely PP to determine the LV function can lead to an inaccurate assessment of the LV function. For example, PP can be high in patients with poor LV contractility and low compliant arteries, indicating good contractility of the heart, although this is not the case. Therefore, to improve the evaluation of the LV function, it is important to quantify the arterial compliance in these patients.

2.1 Arterial compliance

The arterial compliance is mainly determined in the aorta. Compliance describes the change in volume of as a consequence of a change in pressure. The aortic compliance in healthy, normotensive or hypertensive, adults between 25 and 56 can range between 0.230 and 2.719 mL/mmHg [21]. With increasing age from 19 to 83, the compliance decreases with 46%. Although this is a strong relation, there is still a large individual variability [22], [23]. There are several methods to estimate compliance. First, local compliance estimation, in which compliance is estimated as the change in volume of the aorta, due to a certain change in pressure. The change in volume of the aorta can be measured using the dissension of the aortic area due to the increase in pressure from diastolic to systolic pressure. The change is pressure is then defined as the PP. However, assuming a non-significant axial vessel movement leads to an underestimation of the total compliance [24], [25]. Moreover, in patients supported with VA ECMO, PP is generally small. Therefore, the change in diameter of the aorta is small and cannot be measured accurately. A second method is based on stroke volume (SV) derived by echocardiography. The SV is used together with the PP to calculate compliance,

$$C = \frac{\text{SV}}{\text{PP}}. \tag{1}$$

Estimation of the change of volume with SV to calculate compliance is a simplification that can lead to overestimation of C [25]. A third option to estimate compliance is to use the arterial blood pressure signal. Using the assumption of a two-element Windkessel model, the waveform of the arterial blood pressure can be used to estimate C when the total vascular resistance (R) is known [25]–[27].

2.2 Vascular resistance

The total vascular resistance is mainly determined in the peripheral arterioles. The vascular resistance can increase between 19 and 83 years old with 37% [22]. The resistance mainly depends on the total internal radius of the vessels. For a rigid tube the resistance depends on the fourth power of the internal radius of the tube [28]. During VA ECMO and especially during the use of vasoactive drugs, changes in this radius occur frequently, causing large daily changes in the systemic vascular resistance. Total peripheral resistance can range between 0.6 – 0.9 mmHg·s/ml in healthy young subjects [29]. Using Ohm's law, the systemic vascular resistance (R) can be expressed, using mean arterial pressure (MAP) and cardiac output (CO),

$$R = \frac{\text{MAP}}{\text{CO}}. \tag{2}$$

3 Left ventricular flow monitoring using arterial blood pressure during VA ECMO: a simulation study

3.1 Introduction

Cardiac function monitoring is important in critically ill patients in the ICU. Techniques for hemodynamic monitoring in these patients have been further developed in the last years and the use of minimally- and non-invasive techniques has increased [30]. Adequate hemodynamic monitoring is especially important in patients supported with VA ECMO, to monitor cardiac recovery and provide the best possible conditions for the patient. It is however difficult to determine the cardiac function in these patients. Many parameters and measurements are influenced by the interaction between the VA ECMO circuit and the patient's heart [31]. It would be beneficial to monitor the LV flow, independently from the VA ECMO flow, to differentiate between their contributions.

Monitoring LV flow in patients supported with VA ECMO is not straightforward. Methods to determine SV become reduced or unreliable when applied during VA ECMO. A possible solution would be to apply the two-element Windkessel model. This is a lumped parameter model describing the global behaviour of pressure in the arteries due to the pulsatile flow from the LV. This model and variations, are also the basis of most pulse wave analysis (PWA) methods which estimate CO from arterial blood pressure waveforms [32]–[34]. These PWA methods can be applied to non-invasive derived blood pressures, as well as to invasively obtained blood pressure from an arterial catheter. In the ICU, a radial artery catheter is used to monitor arterial blood pressure. For these invasively derived blood pressure waves, PWA methods can be classified into externally calibrated, internally calibrated and non-calibrated. Externally calibrated methods use a reference method to calibrate the PWA system, i.e. the PiCCO (Pulsion Medical Systems, Germany) system uses this type of calibration, where the system is calibrated with the CO measured using thermodilution to correct for patient specific compliance. Internally calibrated methods only use the invasively obtained arterial blood pressure waveform, together with biometric, demographic and hemodynamic data to estimate CO. These methods can be less reliable in patients with specific pathophysiologies or in specific clinical settings, such as during VA ECMO. Lastly, there are also non-calibrated PWA methods. These methods exclusively use the arterial blood pressure waveform and its features to estimate the CO [35], [36]. To the best of our knowledge, PWA methods have never been studied in patients supported with VA ECMO. Besides, we think it is important to derive an estimation of the LV flow next to estimating SV or CO, since parameters derived from LV flow can give an indication of the left ventricular contractility [37]. Therefore the Windkessel model will be applied to determine LV flow from arterial blood pressure.

The two-element Windkessel model describes the relation between blood pressure and blood flow in the arterial system. Since the arterial blood pressure is continuously measured in patients in the ICU, we hypothesized that the two-element Windkessel model can be used to continuously monitor the flow originating from the LV, during VA ECMO. In this study we therefore used three different cardiovascular simulators to evaluate the application of the Windkessel model in different hemodynamic situations, all including VA ECMO support. Besides, a method to determine patient specific arterial compliance is described and validated.

3.2 Methods

3.2.1 Windkessel model

The Windkessel model is a lumped parameter model that describes the relation between blood pressure and blood flow. The model started as a one-parameter model, only using the vascular resistance (R). Later, the model was extended towards the two-element model, which also includes the arterial compliance (C). The two-elemement Windkessel model correctly describes the system for low-frequencies. To improve the behaviour of the model for higher frequencies, the model was extended to a three-element Windkessel model by adding the characteristic impedance of the proximal aorta (Z_c) and to a four-element model, which also includes the inertia of the blood, represented by a coil with inductance (L) [38], [39]. Figure 2 shows the hemodynamic and electrical representation of the three Windkessel models [38]. In all Windkessel models, the elements are parameters that need to be estimated for the individual patient. Therefore, we selected the two-element Windkessel model, to simplify the definition of these patient specific model parameters.
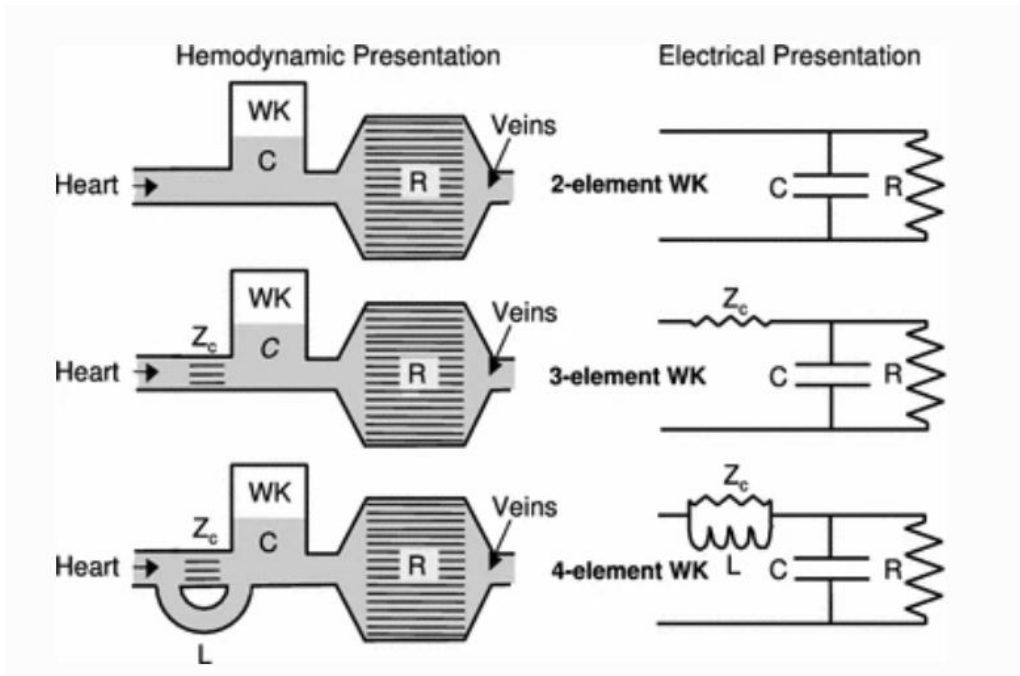
Figure 2: Hemodynamic and electrical representation of the two-, three- and four-element Windkessel (WK) model [38].

The two-element Windkessel (WK) model describes the relation between blood pressure and flow using arterial compliance and vascular resistance, as shown in the top part of Figure 2. This figure also shows the electrical representation, using a capacitor and resistor. Using Kirchhoff's law for current in this two-element WK model, we can find the relation between the total blood flow ($Q(t)$) and the arterial blood pressure ($P(t)$),

$$Q(t) = \frac{P(t)}{R} + C\frac{dP(t)}{dt}, \tag{3}$$

with parameters R and C, respectively representing vascular resistance and arterial compliance. In the usual physiological situation, the blood flow into the arterial system only originates from the LV.

When a patient is supported with VA ECMO, another source is added to the system. In this situation, the input of the WK model consists of the pulsatile flow originating from the LV ($Q_{LV}(t)$) and the constant ECMO flow ($Q_E(t)$). Figure 3 shows a schematic representation of the system,

$$Q_E(t) + Q_{LV}(t) = \frac{P(t)}{R} + C\frac{dP(t)}{dt}.$$

(4)
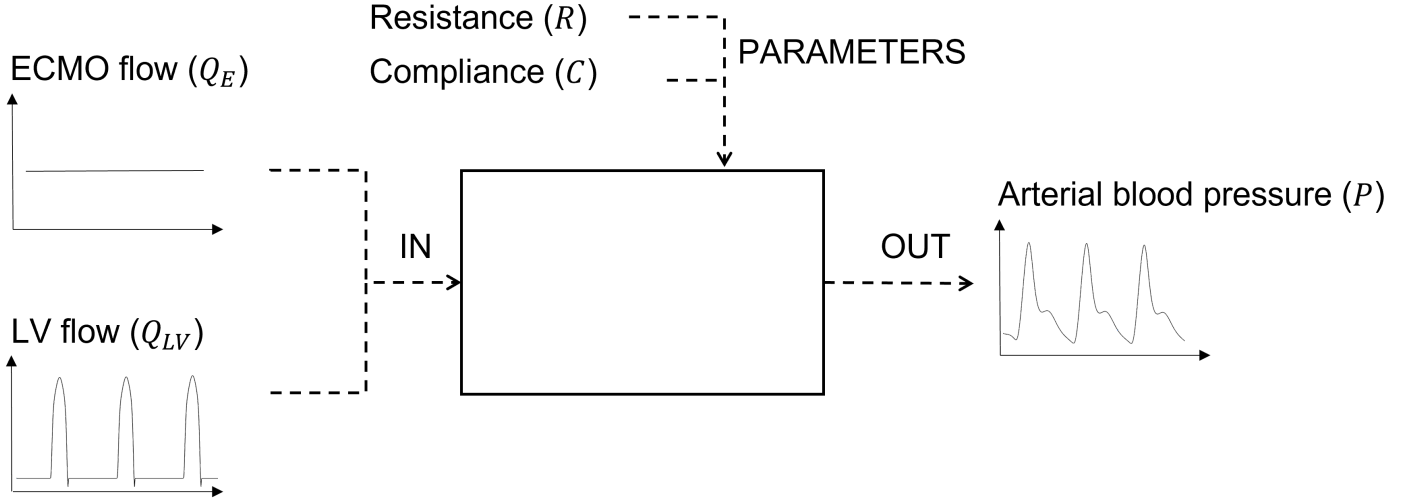
Figure 3: Schematic representation of the two-element Windkessel model with pulsatile LV flow, Q_{LV}, and constant ECMO flow, Q_E, as inputs. Patient specific vascular resistance, R and arterial compliance C as parameters and the arterial blood pressure P as output of the system.

In the clinical setting, Q_E and P are known. Together with the patient specific parameters R and C, the LV flow can be calculated from this model.

3.2.2 Simulations

In this study we used three different cardiovascular simulators: the cardiovascular simulator from the University of Twente (Enschede, The Netherlands), the cardiovascular simulator from Harvi (PVLoops LCC, New York, USA) and Aplysia CardioVascular Lab (Version 9.9.7.0, 2022, Aplysia Medical AB, Stockholm, Sweden) [40], [41]. All three simulators are cardiovascular simulators based on a comprehensive lumped parameter model. In all simulators, cardiovascular parameters can be adjusted and a VA ECMO device can be added to simulate different patients and situations. Using these cardiovascular simulators, the complex interaction between ECMO and the native hemodynamics can be simulated. We performed 25 simulations in each simulator, while the VA ECMO device was turned on according to the clinical guidelines of the University Medical Centre Utrecht (UMCU). For the University of Twente (UT) simulator, data was acquired during 30 seconds with a sampling frequency of 1kHz. Data with a duration of 60 seconds and a sampling frequency of 200Hz was obtained from the Harvi simulator and from Aplysia.

To perform the simulations, first a baseline patient was set up, which is a patient with severe LV heart failure. To create a realistic patient we used clinical data of patients supported with VA ECMO in the ICU of the UMC Utrecht. The heart rate (HR) of this baseline simulation patient was set to 100

Table 1: Simulation scenarios

	R	C	HR	RV function	AS	MR
Baseline	100%	100%	100%	100%	None	None
1	-30%					
2	-50%					
3	+30%					
4	+50%					
5		-30%				
6		-50%				
7		+30%				
8		+50%				
9	-30%	-30%				
10	+30%	-30%				
11			-60%			
12			-40%			
13			-20%			
14			+20%			
15			+40%			
16				-10%		
17				-30%		
18				-60%		
19					Mild	
20					Moderate	
21					Severe	
22						Mild
23						Moderate
24						Severe

beats per minute (BPM). The systemic vascular resistance, was calculated using $R = \frac{\text{MAP}-\text{CVP}}{\text{CO}}$, with ranges for CO, MAP and central venous pressure (CVP), obtained from the clinical data. The mean pulmonary artery pressure (mPAP), and the pulmonary wedge pressure (PWP), were used similarly to calculate the pulmonary vascular resistance [40]. Subsequently, the PV loop was adjusted by changing the LV elastance and filling properties. The ESPVR as shown in Figure 1 was fitted such that it passes through the point where the pressure equals the systolic blood pressure (SBP) and the volume equals the LV end-systolic volume from the clinical data. The EDPVR was adjusted such that it passes through the point where the pressure equals PWP and the volume equals the LV end-diastolic volume estimated from the clinical data [42].

Starting with the created baseline patient, several parameters were varied to study the accuracy of the LV flow calculations for different hemodynamic situations. Table 1 shows all the 25 simulations performed in each simulator. The R and C were varied with 30 and 50%, heart rate (HR) was varied from 40 to 140 BPM, right systolic function was impaired by decreasing right ventricular elastance to 90, 70 and 40% of the healthy situation and aortic valve (AV) stenosis (AS) and mitral valve (MV) regurgitation (MR) were introduced. To simulate no, mild, moderate and severe AV stenosis, we used guidelines from the European Association of Cardiovascular Imaging and the American Society of Echocardiography [43]. In the Harvi simulator and Aplyisa, the aortic valve area (AVA) could be set,

in the UT simulator the resistance of the AV was increased to simulate the stenosis. To simulate no, mild, moderate and severe MR, we used values for the effective regurgitation orifice area for the Harvi simulator and Aplysia. In the UT simulator the backward resistance of the MV was decreased and the severity was assessed by calculating the regurgitation volume [44]. The grading of AS and MR was performed without flow from the VA ECMO.

3.2.3   Left ventricular flow

From the simulations with all 25 different sets of parameters, we used ECMO flow, LV flow, resistance and compliance and the resulting arterial pressure waveform to determine the left ventricle flow over time by applying the two-element Windkessel model using MATLAB (Version 2022b, MathWorks Inc., Natick, USA). The LV flow calculated with the Windkessel model was compared to the corresponding LV flow from the simulators. Figure 4 shows the procedure to evaluate the LV flow calculations. For blood pressure P, we used the pressure in the ascending aorta from the UT simulator, for the Harvi simulator we used the aortic pressure and for Aplysia we used the arterial pressure. The blood pressure from the UT and Harvi simulator was filtered, since this data contained small high-frequency fluctuations in the signal that caused large errors in the derivative of the pressure. The blood pressure is filtered using a 20 Hz, 2nd order low-pass Butterworth filter, since we are interested in the frequencies below 20 Hz [45]. The P is used together with the set values for the Q_E, R and C in Equation (4), to determine Q_{LV}. Since ECMO flow is not exactly constant, but is afterload dependent, the ECMO flow changes through the cardiac cycle. However, in the clinical setting, only a constant value for ECMO flow is registered. Therefore the data from the UT simulator was used to calculate LV flow with both, the actual ECMO flow and a constant ECMO flow for Q_E.
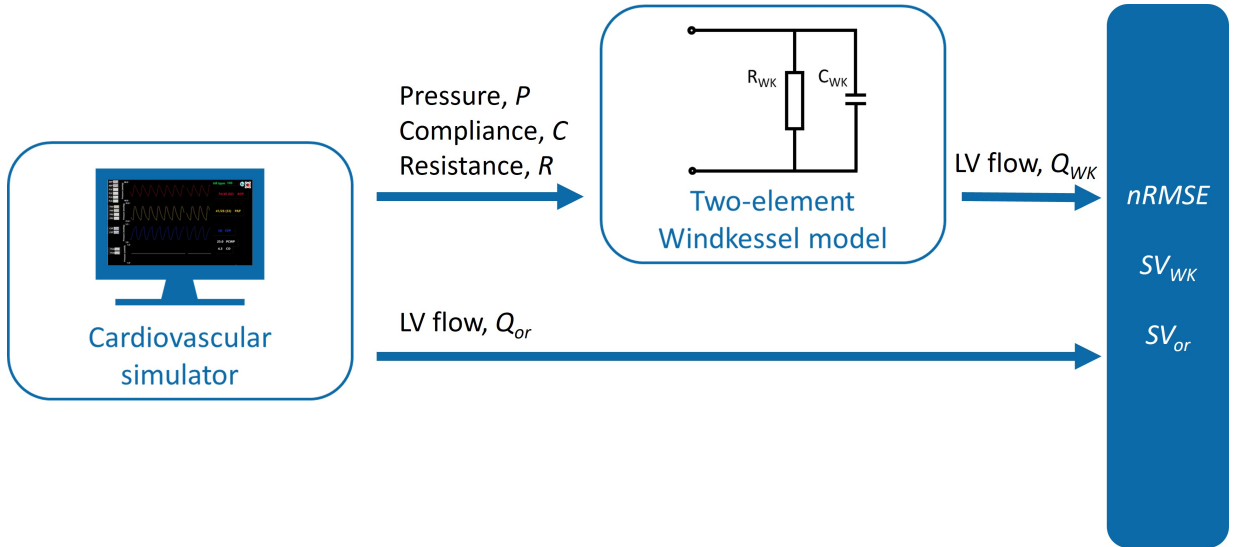

Figure 4: The method used to compare the LV flow calculated from the two-element Windkessel model (Q_{WK}), with the flow originally from the cardiovascular simulator (Q_{or}). The normalized root mean squared error (nRMSE) and the stroke volume from the simulator (SV_{or}) and from the calculated LV flow (SV_{WK}) are used to compare the two LV flows.

To evaluate the quality of the LV flow determined with the two-element WK model (Q_{WK}), it is compared to the LV flow from the simulator (Q_{or}). The Q_{or} is given by the UT simulator, for the Harvi simulator this is calculated from the LVOT velocity and LVOT diameter, for Aplysia the flow through the aortic valve is used. To compare Q_{WK} with Q_{or}, two different measures are used. First the stroke volume (SV), this is also used in the clinical practice and is therefore an important characteristic of the calculated LV flow. The SV is calculated as the mean of the integral of the LV flow over ten beats. To also define the degree of similarity of the entire LV flow signal, the second measure we used is the normalized root mean squared error (nRMSE),

$$\text{RMSE} = \sqrt{\frac{\sum_{i=1}^{N} \|Q_{or}(i) - Q_{WK}(i)\|^2}{N}} \tag{5}$$

$$\text{nRMSE} = \frac{\text{RMSE}}{\bar{Q}_{or}}, \tag{6}$$

with N the length of the signal and $\bar{Q}_{or}$ the mean of Q_{or}.

3.2.4 Adapted time-decay method

The two-element WK model requires two patient-specific parameters. Therefore the vascular resistance and arterial compliance need to be determined in patients to be able to apply the WK model. The time constant RC is also known as the time constant of the exponential decay of the blood pressure during diastole. The diastolic part of the blood pressure wave can therefore be used to estimate RC. The time-decay method uses this time constant from the arterial blood pressure curve to determine arterial compliance. In the diastolic phase, it can be assumed that there is no blood flow from the heart. Hence, the left-hand side of Equation (3) becomes zero. Solving this differential equation such that P_0 is the pressure at t_0 during the diastolic phase,

$$P(t) = P_0 e^{\frac{-(t-t_0)}{RC}}. \tag{7}$$

Assuming the pressure decay in the diastole is exponential according to the above equation, the time constant RC can be determined. For known vascular resistance or arterial compliance, respectively C or R can be estimated [25], [27]. However, for this method it is assumed that $Q = 0$, which is not true at any time for patients supported with VA ECMO. Hence, an adjustment was made to this method. Assuming Q_{LV} is indeed zero during diastole, but there still is a constant flow Q_E from the ECMO circuit, Equation (4) can be solved such that P_1 is the pressure at t_1 during the diastolic phase,

$$P(t) = (P_1 - RQ_E)e^{\frac{-(t-t_1)}{RC}} + RQ_E. \tag{8}$$

This equation can be used in patients with and without VA ECMO support, since for $Q_E = 0$ Equation (7) and Equation (8) are equal. To validate the equation, we used the blood pressure and parameters from the simulations described in Section 3.2.2. Using Equation (8) to determine C_{decay}, first the diastolic phase of the arterial blood pressure wave needed to be selected, as shown in blue in the blood pressure wave in Figure 5. Since the blood pressure in the Harvi simulator and Aplysia show a dicrotic notch, the pressure after this dicrotic notch is used as the diastolic part. For the UT simulator, the time at which flow becomes zero is used to determine the start of the diastole. This diastolic phase was selected in three consecutive beats. Next, for every beat we estimated C by the value that minimizes the RMSE between the selected diastolic blood pressure signal and Equation (8). Values of C between 0.01 and 10 mL/mmHg were tested with increments of 0.01 mL/mmHg. Finally, C_{decay} is defined as

the average of the C estimations of three consecutive beats. We compared C_{decay} with the original compliance C_{or} set in the UT simulator using actual and constant ECMO flow and in the Harvi simulator and Aplysia with actual ECMO flow, as shown in Figure 5
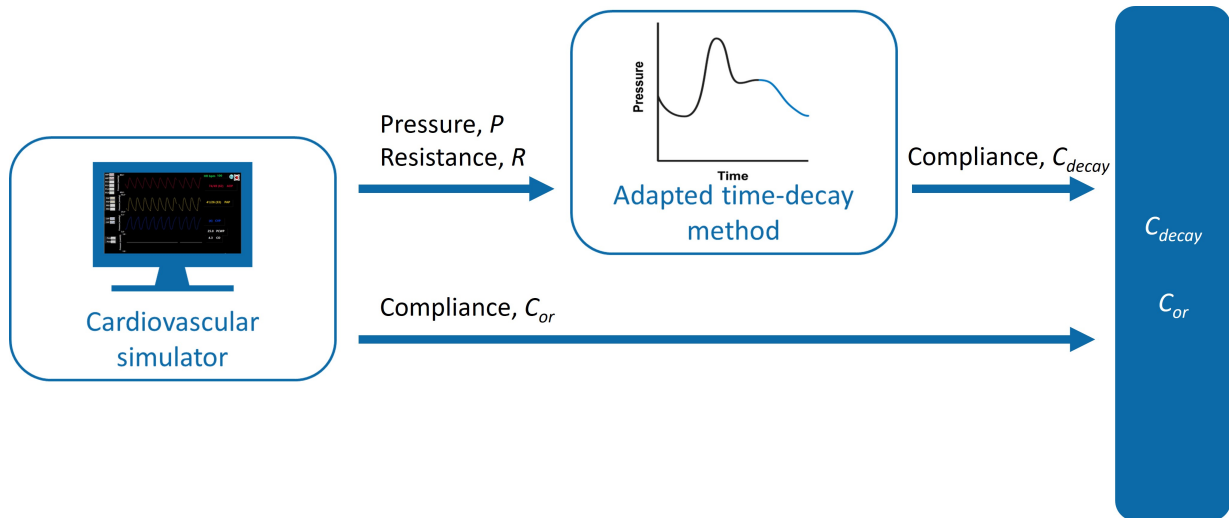
Figure 5: The method used to evaluate the compliance estimation using the adapted time-decay method C_{decay} in simulated arterial blood pressure data P, with a known resistance R.

3.3   Results

In all three simulators, a baseline patient was simulated. Table 2 shows the values for MAP, CVP, PWP, CO and Q_E for the baseline patient in all simulators. For the CVP and PWP, respectively the right and left atrial pressure was used. All parameters used for the simulation in the UT simulator, Harvi simulator and Aplysia can be found in Appendix A, Tables 7, 8 and 9.

Table 2: Mean arterial pressure (MAP), central venous pressure (CVP), pulmonary wedge pressure (PWP), native cardiac output (CO) and VA ECMO flow (Q_E) of the simulated baseline patient in the three simulators.

	UT simulator	Harvi simulator	Aplysia
MAP [mmHg]	71	69	76
CVP [mmHg]	2.9	2.2	5.5
PWP [mmHg]	32	29	21
CO [L/min]	3.0	3.3	3.2
Q_E [L/min]	2.0	2.1	2.1
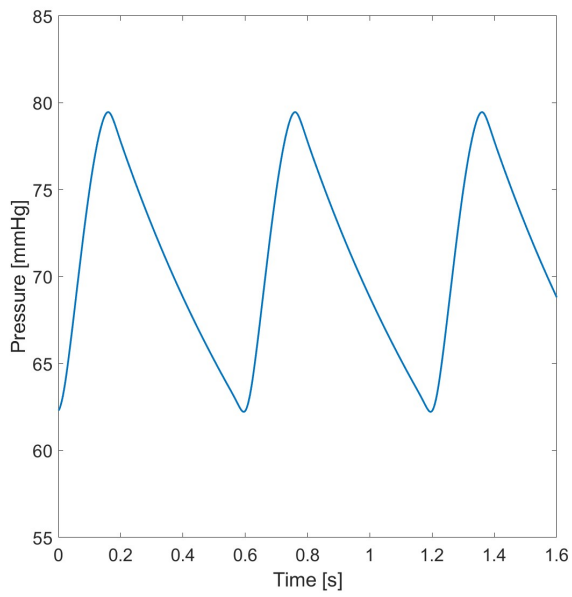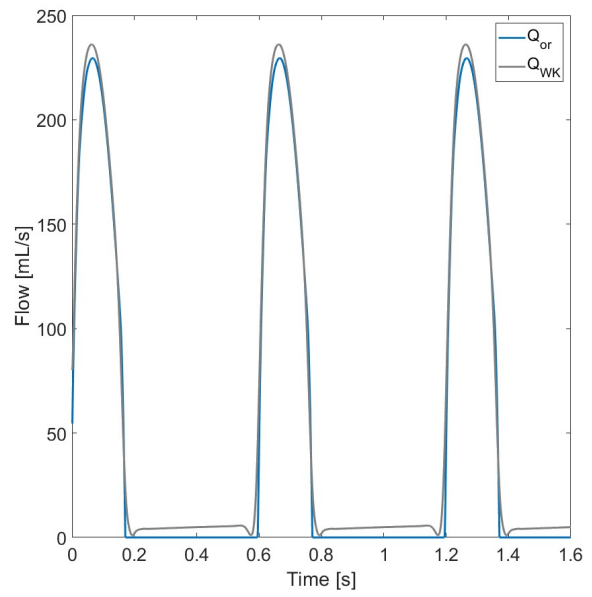
Figure 6: a) Arterial blood pressure and b) LV flow simulated with the UT simulator (Q_{or}) in blue and LV flow calculated from the blood pressure using the two-element WK model (Q_{WK}) in gray.
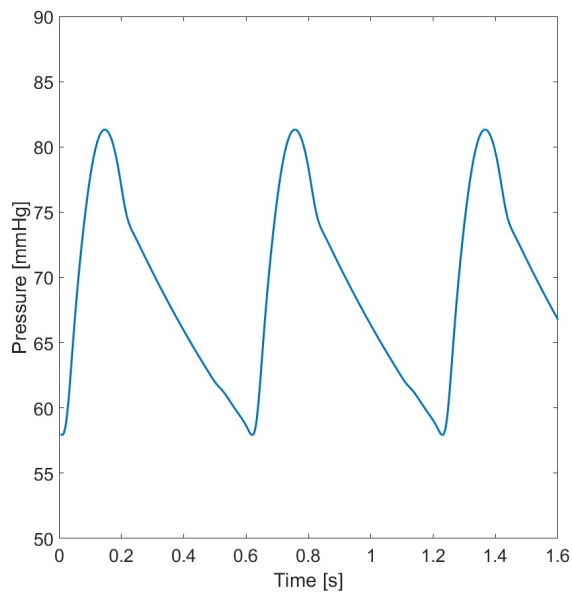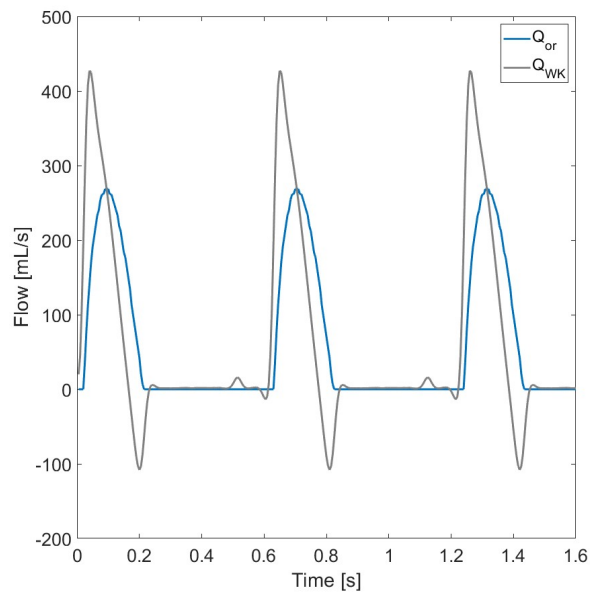
Figure 7: a) Arterial blood pressure and b) LV flow simulated with the Harvi simulator (Q_{or}) in blue and LV flow calculated from the blood pressure using the two-element WK model (Q_{WK}) in gray.
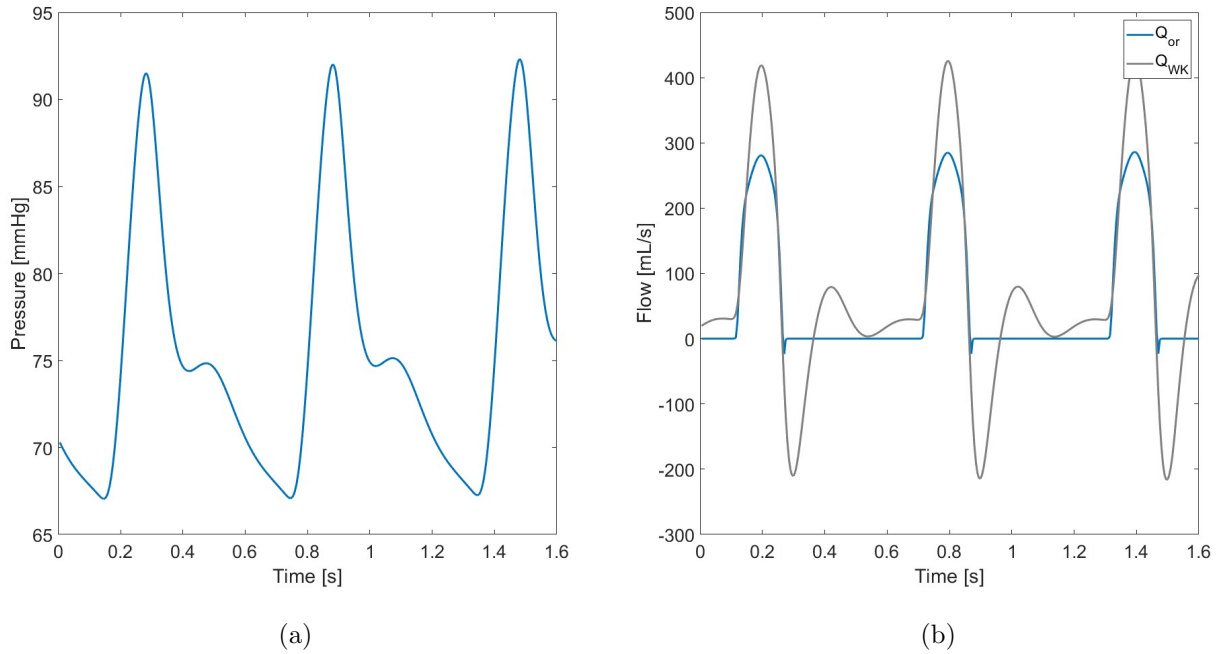
Figure 8: a) Arterial blood pressure and b) LV flow simulated with Aplysia (Q_{or}) in blue and LV flow calculated from the blood pressure using the two-element WK model (Q_{WK}) in gray.

3.3.1 Left ventricular flow

Figure 6, 7 and 8 show on the right the Q_{or} and Q_{WK} respectively for the UT simulator, the Harvi simulator and Aplysia. On the left of side, these figures show the arterial pressure from the simulator, used to calculate LV flow with the two-element Windkessel model. The three simulators have different pressure waveforms and all show different patterns for Q_{WK}. Besides, the difference between Q_{or} and Q_{WK} is the smallest for the UT simulator.

The quality of the calculated LV flow is expressed as a percentage error for SV and by using the nRMSE. Figure 9 and 10 show boxplots of the error in SV and nRMSE from the (a) UT simulator, (b) UT simulator with constant ECMO flow, (c) Harvi simulator and from (d) Aplysia. The error in SV is the smallest for the Harvi simulator, with a mean error of 2.5%. The calculated SV from Aplysia differs the most from the original SV, with a mean error of 26.3%. For the UT simulator, the error in SV is equal using actual and constant flow, both with a mean of 11.4%. The differences in the percentage error for SV due to the change of parameters in the simulated scenario's are shown in Appendix D, Figure 24.

The UT simulator shows the smallest nRMSE with a mean of 0.16 using actual ECMO flow and 0.17 for constant ECMO flow. Compared to the UT simulator, the nRMSE for the Harvi simulator and Aplysia are larger, which is in line with Figure 6b, 7b and 8b, since nRMSE also takes the waveform of the LV flow into account.
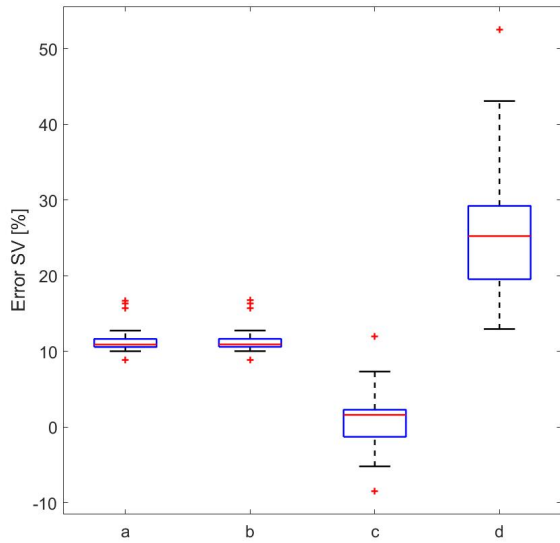
Figure 9: The percentage error of the calculated SV, with respect to the original SV from the (a) UT simulator, (b) UT simulator with constant ECMO flow, (c) Harvi simulator and from (d) Aplysia.
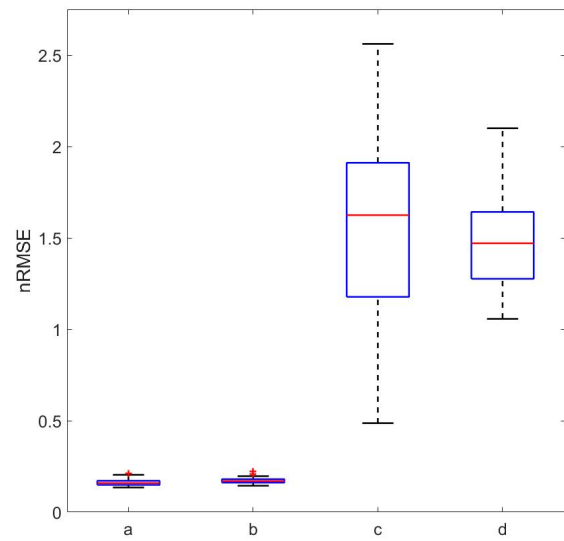
Figure 10: The nRMSE of the calculated LV flow, with respect to the original LV flow from the (a) UT simulator, (b) UT simulator with constant ECMO flow, (c) Harvi simulator and from (d) Aplysia.

3.3.2 Adapted time-decay method

Figure 11 shows the correlation between C_{decay} and C_{or}, with the dashed line indicating $C_{decay} = C_{or}$. The values for C_{decay} determined from the UT and Harvi simulator data is close to corresponding values for C_{or}, for Aplysia the C_{decay} overestimates the actual compliance in all cases. Note that the range of the y-axis in Figure 11c is larger than for the UT and Harvi simulator.
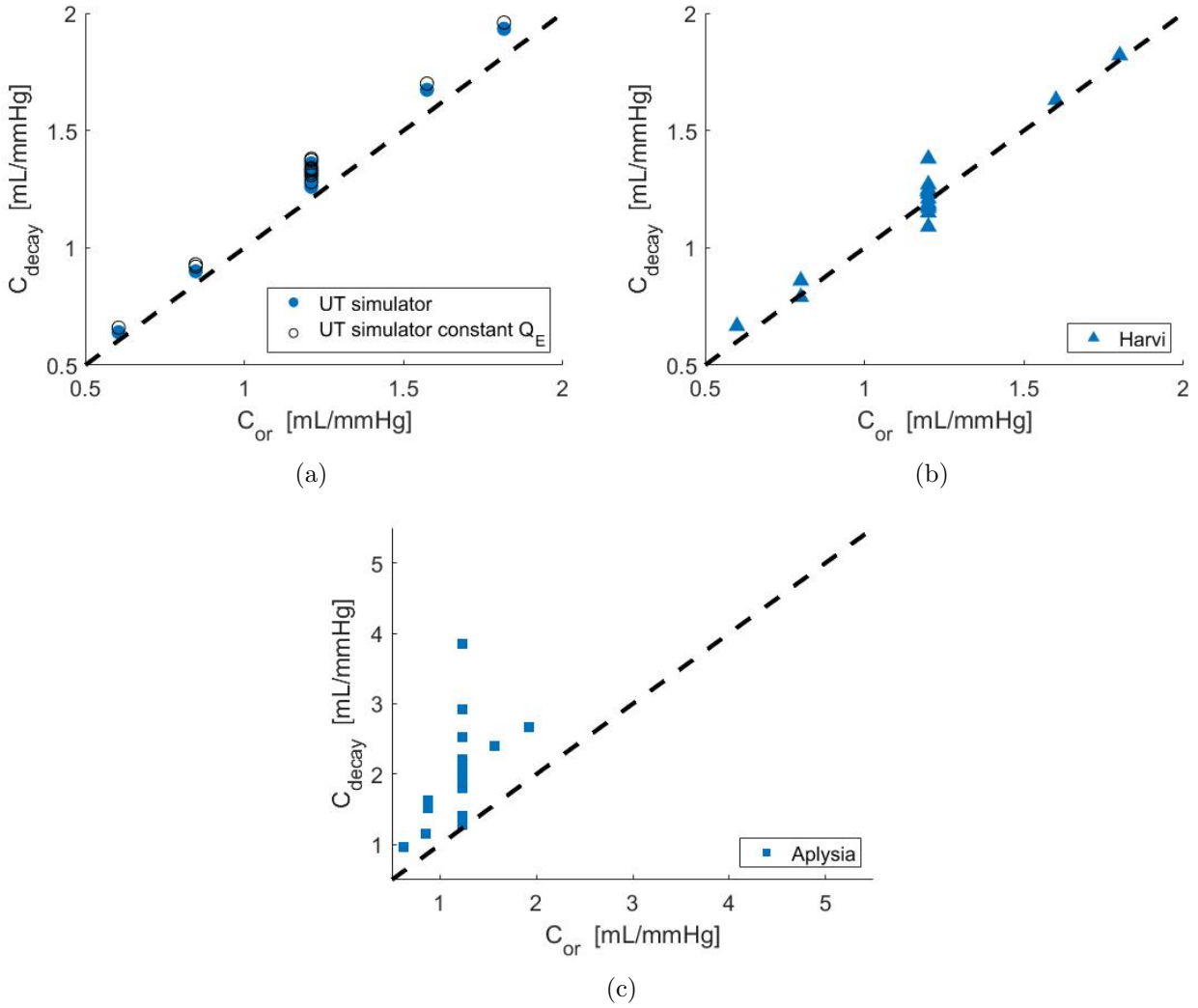
Figure 11: The compliances determined using the adapted time-decay method, C_{decay} and the compliance originally set in the simulator, C_{or}. For respectively the (a) UT simulator with actual and constant ECMO flow (Q_E), (b) the Harvi simulator and (c) Aplysia. The dashed line indicates $C_{decay} = C_{or}$.

3.4 Discussion

In this study we used three different cardiovascular simulators to study the quality of left ventricular flow determined from the blood pressure signal using the two-element Windkessel model during VA ECMO. In two simulators the calculation of the LV flow resulted in an average error in SV below 12%. For the third simulator, the average error was larger with an average of 26%. Data from the same simulations was also used to study an adapted time-decay method to determine compliance from arterial blood pressure in patients supported with VA ECMO. In two of the simulators, the compliance did not differ more than 0.18 mL/mmHg. In the third simulator, the maximum difference was clearly higher, with 2.6 mL/mmHg.

3.4.1 Stroke volume

Our results show that application of the two-element Windkessel model to arterial blood pressure can estimate LV flow in simulated patients, supported with VA ECMO. Especially the errors found in the calculation of the SV are consistence with other PWA methods. To the extent of our knowledge other PWA methodes to estimate CO were never tested in simulation studies. However, there are multiple studies in which PWA methods, based on two-element Windkessel models, are tested in porcine data without VA ECMO support. The SV error below 12% we found in two of the three simulators agrees with the average error in CO between 11.8 and 14.5% found in these studies with porcine data [32]–[34]. Bond et al. studied the application of an uncalibrated PWA method in patients supported with veno-venous ECMO and used echocardiography for the reference CO. Although the interaction of veno-venous ECMO with the patients hemodynamics differs largely from VA ECMO, the SV error we found in the UT simulator does agree with the average CO error of 10.1% found by Bond et al. [46].

3.4.2 Waveform

From Figure 6, 7, and 8 it becomes clear that the pressure and flow waveforms are different for all three simulators. The blood pressure waveform for Aplysia is visually the most clinically realistic, showing a clear dicrotic notch. Aplysia also shows left ventricular flow closest to what is expected, including negative flow, which is physiologically followed by aortic valve closing [47]. The pressure waveform in the UT simulator is the least complicated, visually the waveform of the calculated flow is also most similar to the original LV flow. This is confirmed by the nRMSE, Figure 10 shows. When studying the boxplots in Figure 9 and 10, it is noteworthy that application of the two-element Windkessel model on data from the Harvi simulator results in a very small error in SV, even though there is a large inaccuracy in the waveform, reflected by the nRMSE.

Values for nRMSE are not commonly used in evaluation of PWA methods, since most methods aim to determine SV, or even CO. Hence, it is hard to translate the resulted nRMSE values to clinical practice. We studied the nRMSE value since we think that LV flow waveform can help in the future to study contractility estimators, such as the systolic acceleration of blood flow in the LVOT [37]. Regarding to the waveform it is also important to notice that in this study, both, the simulators and the two-element WK model are lumped parameter models. These models do not account for wave transmission and reflection, which are present in the real arterial system [38], [39]. To study the validity of the method proposed in this study in the situation where also wave transmission and reflection occur, the method should be studied in clinical data.

3.4.3 Adapted time-decay method

Figure 11 shows that the estimation of C using the adapted time-decay method overestimates the original compliance most of the time. Especially in Aplysia, this overestimation is large, with an average overestimation of 0.78 mL/mmHg (37.0%) with outliers up to 2.6 mL/mmHg (68.0%). In particular these outliers suggest that the adapted time-decay method would not be a suitable method to estimate arterial compliance in the clinical setting. However, a different conclusion is drawn from the data from the UT or Harvi simulator. In these simulators the compliance estimation results in only small errors, on average between 0.05 and 0.1 mL/mmHg, respectively 4.6 and 6.8%. The errors found in the UT and Harvi are similar to the values found by Stergiopulos et al., using a non-linear computer model of the systemic arterial tree to test the time-decay method without VA ECMO [27].

The different accuracy of C_{decay} between the simulators may be explained by the main assumption in the time-decay method. As explained in Section 3.2.4 the adapted time-decay method uses the assumption that during diastole, the flow consists of only the VA ECMO flow. This is however only true in the ascending aorta [25], [27]. Since the pressure data from Aplysia is defined more distally, compared to the UT and Harvi simulator, this may have influenced the accuracy of the compliance determined with the adapted time-decay method.

3.4.4 Strengths and limitations

In this study, cardiovascular simulators were used to validate the application a two-element Windkessel model to calculate LV flow from arterial blood pressure. The advantage of using cardiovascular simulators is the possibility to simulate a wide range of hemodynamic situations, including the interaction with a VA ECMO device. Besides, in contrast to the clinical setting, all patient specific parameters, including resistance and compliance are known in these simulations. Since it is difficult to determine compliance in patients, simulation data can be used to test the application of the Windkessel model without the interference of inaccurate patient specific parameters. Additionally, in Appendix D, Figure 24 shows that the change in SV error due to changing parameters is neglectable for the UT and Harvi simulator, suggesting that our method stays accurate for changing hemodynamic situations.

Since all simulators are lumped parameter models, they only partly represent the interactions in the cardiovascular system of a patient. Next to this, there is another difficulty in applying the Windkessel model to clinical data. As discussed earlier, the parameters need to be estimated for each individual patients, while parameters also change over time. Although a method to calculate compliance is proposed and shows promising results in this study, the estimation of compliance and resistance will introduce extra uncertainty.

We also studied the effect of using constant instead of actual ECMO flow in our method. Whereas the actual ECMO flow is known from the simulators, in the clinical practice only a constant value for ECMO flow is registered. Since the fluctuation in ECMO flow due to the changing afterload during the cardiac cycle are small, we expected this to have little to no influence in the calculations of our model. This is indeed confirmed by the small difference in nRMSE and SV error between a) and b) in Figure 9 and 10.

3.4.5 Conclusion

To conclude, LV flow could be calculated from arterial blood pressure using the two-element Windkessel model. In two of the three cardiovascular simulators, the average stroke volume error was below 12%. In these simulators, also arterial compliance could be accurately estimated using the proposed adapted time-decay method, showing an average overestimation of arterial compliance below 0.1 mL/mmHg. The results in the third simulator however, show a limited accuracy for both methods. Therefore, we recommend to further evaluate the promising application of the two-element Windkessel model and the adapted time-decay method in clinical data of patients supported with VA ECMO.

4 Left ventricular flow monitoring using arterial blood pressure in patients supported with VA ECMO

4.1 Introduction

To improve the clincal care management of patient supported with VA ECMO in the ICU, it is crucial to accurately monitor the LV function. However, it is complex to gain insight in the LV function. The currently evaluated hemodynamic parameters are a result of the interaction between the VA ECMO circuit and the LV. In Section 3.2.1, we described a method to determine the contribution of the LV. The study in different cardiovascular simulators showed promising results in two simulators. These results are however of limited value to draw conclusions about the applicability in clinical data. Compared to the simulated setting, the clinical setting involves more phenomena that might influence the outcome. Not only the wave transmission and reflection, but also the occurrence of noise and measurement errors in blood pressure and patient specific parameter calculations.

Currently, there are multiple methods available to determine CO or SV in patients at the ICU. First, the use of thermodilution using a pulmonary arterial catheter, also known as a Swan Ganz catheter. CO measurement with thermodilution includes the injection of cold fluid or intermitted heating of the blood in the right atrium. Blood flows through the right atrium and ventricle to the thermistor close to the tip in the pulmonary artery, which registers the temperature curve and uses it to calculate pulmonary blood flow. Under the assumption that the output of the right ventricle is equal to the output of the LV, the CO is determined. At this moment, thermodilution using a pulmonary artery catheter is the golden standard for measuring CO in critically ill patients [32], [48]. However, this is not validated during ECMO support [32], [49]. Overestimation of the cardiac output when using a Swan Ganz catheter may occur due to indicator loss. Besides, the use of the Swan Ganz catheter is invasive and not without risks [32], [48].

Another method to determine CO or SV is echocardiography, this can be performed transthoracic (TTE) or transesophageal (TEE). With echocardiography the velocity time integral (VTI) of the left ventricular outflow tract (LVOT) can be determined, as well as the diameter of the LVOT (dLVOT),

$$SV = \pi \cdot \left(\frac{dLVOT}{2}\right)^2 \cdot VTI. \tag{9}$$

However, the accuracy of SV measurements using TTE is limited and cannot be performed continuously [49], [50]. Other available methods to determine CO include analysis of the arterial blood pressure waveform as discussed in Section 3. The disadvantage of the PWA methods is that they are not directly applicable to the patients in our study, due to the influence of the VA ECMO circuit.

The Windkessel model could provide a solution to continuously monitor the LV flow during VA ECMO in the ICU. For the two-element Windkessel model, the patient specific values for vascular resistance and arterial compliance are required. In addition to being used to apply the Windkessel model, accurate estimations of R and C can also provide more insight in the cardiovascular status of the specific patient. Compliance, for example, influences the PP and therefore might be used to improve the interpretation of PP during VA ECMO.

Eventually, we want to improve cardiac function monitoring during VA ECMO. Continuously describing the LV flow will be a first step towards a comprehensive monitoring system, ultimately leading towards a decision support system. The application of the two-element Windkessel model showed to

be promising to calculate LV flow in cardiovascular simulation data. Hence, in this study we further validated the application of this Windkessel model to calculate LV flow using blood pressure in patients supported with VA ECMO. Besides, also the application of the adapted time-decay method to determine compliance and resistance was studied in clinical data.

4.2 Methods

To study the applicability of the two-element Windkessel model as described in section 3.2.1, we conducted a prospective observational study for which echocardiograms and signals that are routinely obtained as part of the daily clinical management are collected in patients supported with VA ECMO in the ICU at the UMC Utrecht. Besides, the same data was also collected in patients supported with a heart-lung machine (HLM) in the operating room (OR), since similar phenomena occur in these patients.

4.2.1 Study population

We included seven patients supported with VA ECMO in the ICU or undergoing cardiac surgery while supported with a HLM in the OR. Patients were excluded if they were supported by a ventriculo-aortic axial pump (Impella) or if their age was below 18 years. Besides, patients were excluded if no LVOT VTI measurement could be performed.

4.2.2 Data acquisition

In patients supported with VA ECMO in the ICU, the arterial blood pressure signals and VA ECMO flow are registered during routine echocardiography. If data registration occurred during a weaning trial, this was repeated for all consecutive flows for which a VTI measurement was available.

In the OR arterial blood pressure signals were registered during weaning of the HLM. In the weaning process, HLM flow is gradually reduced and the LV generates SV again. This setting is similar to the situation during VA ECMO support: flow from the heart and the ECMO together generate the resulting arterial blood pressure. In the OR, pressure signals during three different flows were used, 75, 50 and 25% of the total expected CO.

Arterial blood pressure is measured using a catheter in the radial artery. Standard filtering is performed by the monitor with a low-pass filter of 12Hz, which could not be turned off. Before data registration it is assured that the pressure transducer is set at the correct height, as in daily clinical practice. For each flow, one minute of arterial blood pressure is collected with a sampling frequency of 1kHz. In addition, calibration to zero and flushing of the arterial catheter was registered to calibrate the pressure and review over- or underdamping afterwards.

For the echocardiogram TTE or TEE was used. For every patient, one value for dLVOT was used, assuming this diameter is constant over time within a patient. For LVOT VTI, we used the average VTI of three consecutive beats at each flow, measured with pulsed wave Doppler.

4.2.3 Analysis

Registered arterial blood pressure was first filtered using a 2nd order low-pass Butterworth filter with a cut-off frequency at 20Hz to remove noise. If available, 30 seconds are selected around the VTI measurement.
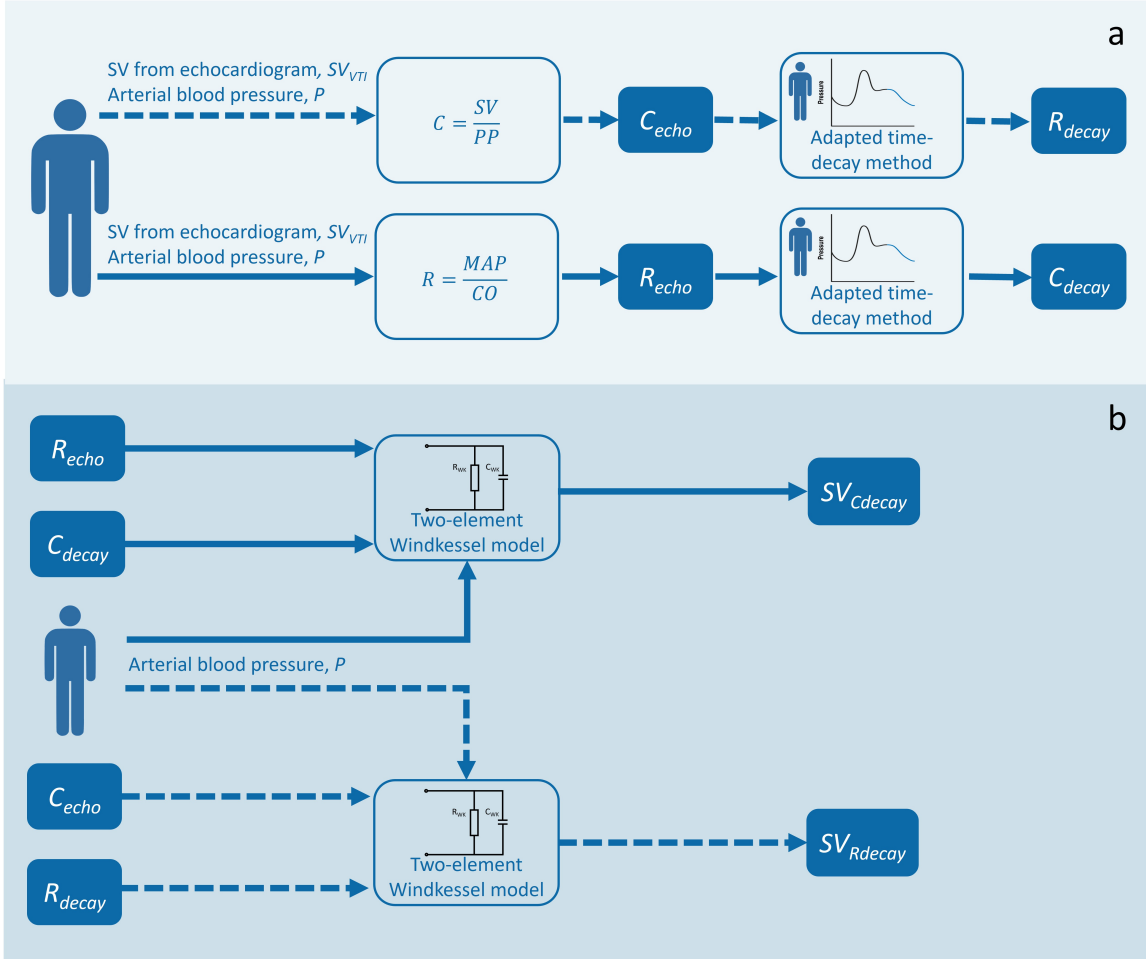
Figure 12: The method used to determine a) R_{echo}, C_{echo}, R_{decay} and C_{decay} and b) SV_{Cdecay} and SV_{Rdecay}.

4.2.3.1 Compliance and resistance

For application of the two-element Windkessel model, the vascular resistance and arterial compliance need to be estimated for each patient and flow. SV and PP or CO and MAP from the arterial blood pressure and echocardiogram measurement are used to determine respectively C_{echo} and R_{echo}, according to Equation (1) and (2). These values were used to validate the adapted time-decay method as proposed in 3.2.4. Equation (8) is used to calculate C_{decay}, using R_{echo}. The compliance determined with the adapted time-decay method is compared to C_{echo}. The equivalent was performed to determine the quality of the resistance estimated with the adapted time-decay method, R_{decay}, using C_{echo}. The upper part of Figure 12 shows a schematic representation of this method.

To determine LV flow, all registrations were first analyzed individually. Equation (4) was applied to the arterial blood pressure data, using 1) R_{echo} with C_{decay} and 2) R_{decay} and C_{echo}, as the bottom part of Figure 12 shows. The resulting LV flow was used to calculate the average SV of three consecutive beats, using the integral of the LV flow. Next, for the patients with a series of successive registrations at different flows, we used compliance from Equation (1) during the previous ECMO flow,

C_0, to calculate the resistance during the current ECMO flow with the adapted time-decay method, R_1. Subsequently, these C_0 and R_1 were used to calculate LV flow with the two-element Windkessel model.

4.2.3.2 *Bland-Altman analysis*

To display the relation between the two-element Windkessel model derived SV and the SV determined from the LVOT VTI and dLVOT, a Bland-Altman plot was used. The Bland-Altman plot shows the agreement between the two methods with the average of the two methods on the x-axis and the difference between the two methods on the y-axis . The mean of the differences is called the bias. Variation around the bias is described by the Limits of Agreement (LoA), defined by ± 1.96 times the standard deviation. Assuming a normal distribution of the differences, 95% of the differences will be within the LoA [51], [52]. The same method is applied to describe the agreement between the patient specific parameters derived using the adapted time-decay method and using Equation (1) and (2).

4.3 Results

In total 19 data registrations were performed in seven patients, of whom three were supported with VA ECMO in the ICU and four were supported with a HLM in the OR.

First, the parameters were determined. Figure 13a shows the agreement between compliance determined using Equation (1), C_{echo} and compliance determined using the adapted time-decay method in Equation (8), C_{decay}. The average difference between these two compliances is -0.56 mL/mmHg, the limits of agreement are -1.68 and 0.57 mL/mmHg for compliances between 0.8 and 2.4 mL/mmHg. Figure 13b shows the agreement for the resistance, comparing the resistance calculated using Equation (2), R_{echo}, with the resistance from the adapted time-decay method, R_{decay}. For these resistances between 0.6 and 1.2 mmHg·s/mL, the mean difference is -0.15 mmHg·s/mL, with limits of agreement of -0.43 and 0.13 mmHg·s/mL.

The values for arterial compliance and vascular resistance were used to determined SV. Figure 14a shows the agreement between the SV determined using the echo measurement of the LVOT VTI and dLVOT (SV_{VTI}) and the SV determined in the two-element Windkessel model using the compliance C_{decay} and the resistance R_{echo}. The mean difference between the SV of these two methods is 0.88 mL, with LoA of -0.51 and 2.27 mL. The agreement between the SV calculated with the Windkessel model using compliance R_{decay} and compliance C_{echo}, is shown in the Bland-Altman plot in Appendix E, Figure 25.

Not in all patients data registration was available for multiple consecutive flows. In five patients data was registered for two to four consecutive flows, together resulting in 15 data registrations. Figure 14b shows the Bland-Altman plot comparing SV_{VTI} with the SV calculated with the two-element Windkessel model, using $R1$ and $C0$. Using these parameters, the difference of the calculated SV, SV_{C0R1}, with the SV_{VTI} show a larger range, with limits of agreement between -25.45 and 26.00 mL, although having an mean difference of 0.26 mL. The agreement of the corresponding values of $R1$ with the values for R_{echo} are shown in Appendix F, Figure 26.

Figure 15 shows an example of the arterial blood pressure with the corresponding LV flow, calculated using the two-element Windkessel model. The LV flow shows a large positive flow to almost 1500 mL/s and a large negative flow, less than -500 mL/s.
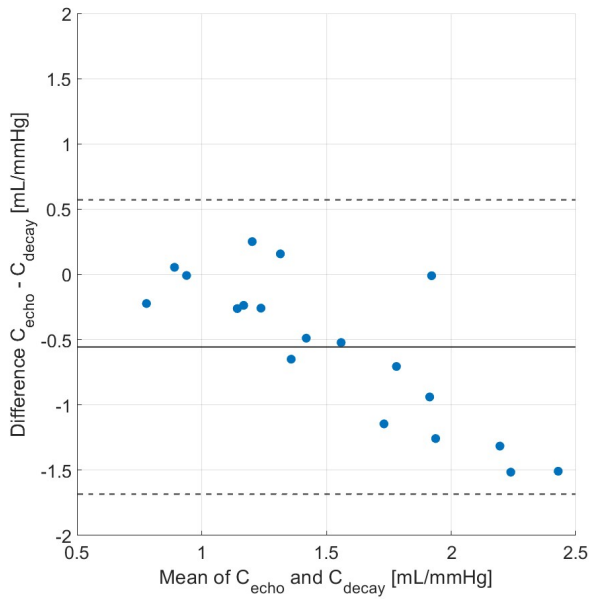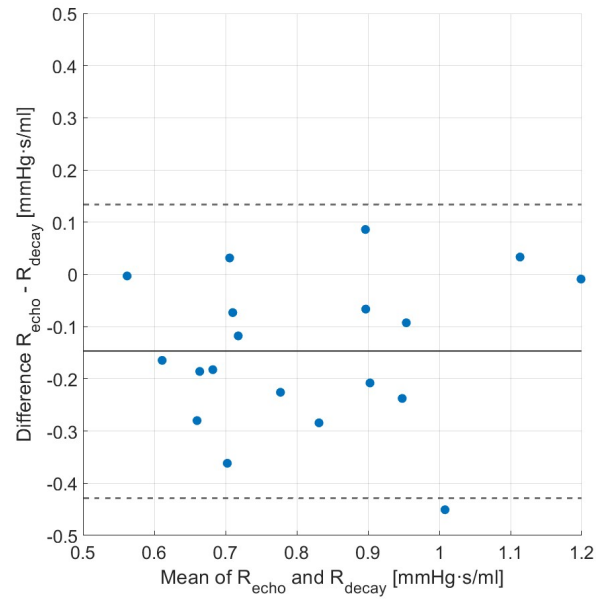
Figure 13: Bland-Altman plots, with the solid line indicating the mean difference, the dashed line the limits of agreement. a) show the agreement between C_{echo} and C_{decay} with an mean difference of -0.56 mL/mmHg and limits of agreement of -1.68 and 0.57 mL/mmHg. b) shows the agreement between R_{echo} and R_{decay}, with a mean difference of -0.15 mmHg·s/mL and limits of agreement of -0.43 and 0.13 mmHg·s/mL.
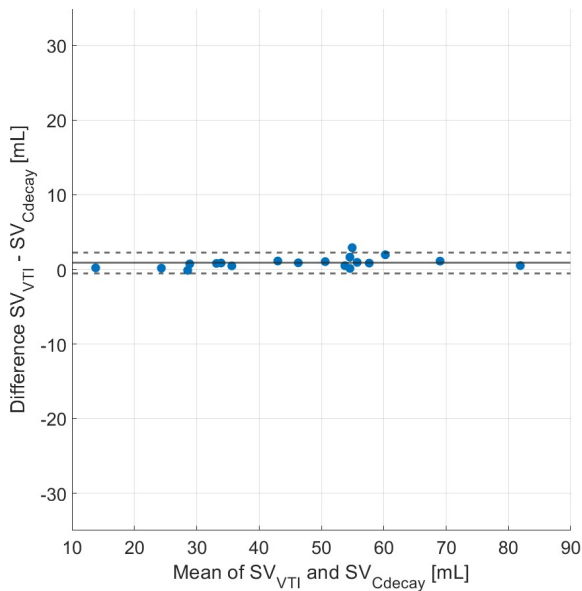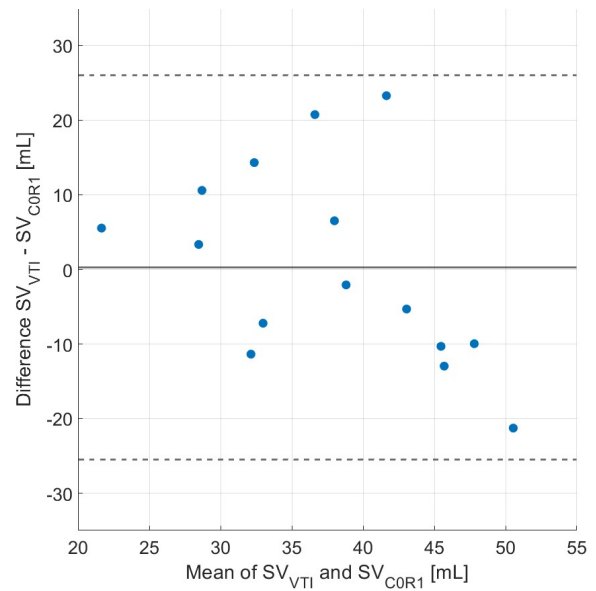
Figure 14: Bland-Altman plots, with the solid line indicating the mean difference, the dashed line the limits of agreement. a) shows the agreement between SV_{VTI} and SV_{Cdecay} with a mean difference of 0.88 mL and limits of agreement of -0.51 and 2.27 mL. b) shows the agreement between SV_{VTI} and SV_{C0R1}, with a mean difference of 0.26 mL and limits of agreement of -25.48 and 26.00 mL.
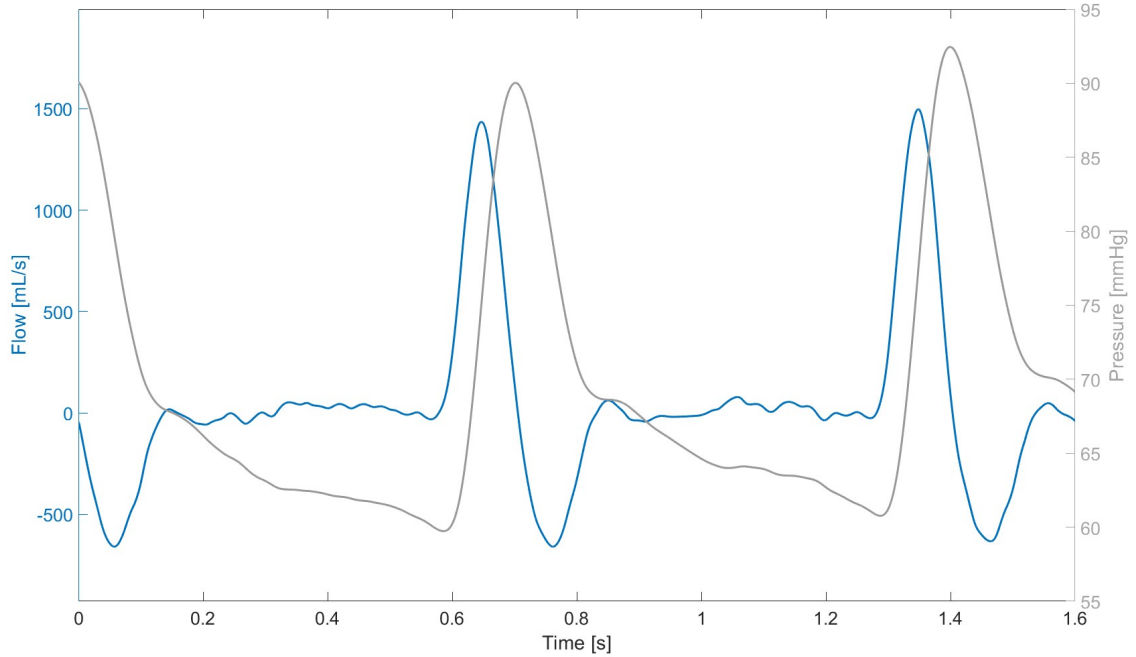
Figure 15: Example of arterial blood pressure [mmHg] in gray and corresponding calculated left ventricular flow [mL/s] in blue.

4.4 Discussion

In this study we performed a proof of principle for the application of the two-element Windkessel model to determine LV flow from arterial blood pressure in patients supported with VA ECMO. We used 19 data registration in 7 patients supported with VA ECMO in the ICU or with a HLM in the OR.

To evaluate the LV flow calculations, results were shown using Bland-Altman analysis. The main advantage of Bland-Altman is that the agreement between two methods can be studied. There is currently no golden standard to determine SV, C or R in patients supported with VA ECMO. Therefore it is most useful to study if our method could replace current available methods. The Bland-Altman plots also include the calculation of the limits of agreement (LoA), which described the range of 95% of the differences, assuming a normal distribution. This assumption is less strict then in usual statistical testing and is therefore visually assessed using boxplots and histograms of the differences. However, due to the small amount of samples, accurate assessment of the normal distribution assumption is difficult. Nevertheless, the LoA can be used as an indication of the agreement between the two methods.

4.4.1 Patient specific parameters

The agreement between the patient specific parameters determined using the adapted time-decay method and using Equation (1) and (2) is large. Especially the average difference is small for both, resistance and compliance. The range of compliance we found in this study agrees with normal values for compliance, between 0.2 and 2.7 mL/mmHg [21]. Figure 13a shows that the difference between C_{echo} and C_{decay} increases as the average value for C increases. This shows that for possible high

27

compliant vessels, the adapted time-decay method does not give the same results as Equation (1). It is important to take into account that the compliance determined with Equation (1) is not necessarily the correct value. In fact, for this equation, it is assumed that the SV is the volume entering the compliant arteries, without taking the outflow of blood into the peripheral vessels into account. This can cause overestimation of the compliance, although Chemla et al. showed the compliance calculated with Equation (1) corresponds to the compliance estimated with the area method [25], [26]. In our results, C_{decay} is usually larger than C_{echo}, which would imply that C_{decay} is an overestimation of the actual arterial compliance. From Figure 13b it seems that R_{decay} is also an overestimation of the real vascular resistance. For the resistance there is no clear dependency of the difference on the mean value of R_{echo} and R_{decay}.

In our study, arterial compliance and vascular resistance are determined using the adapted time-decay method on peripheral arterial blood pressure, measured in the radial artery. As discussed in Section 3.2.4, it is assumed that blood flow equals VA ECMO flow during the diastolic phase. However, this assumption is violated when using peripheral pressure, since in the peripheral vessels, the flow during diastole is larger than only VA ECMO. This can lead to incorrect estimation of RC. To improve the estimation of patient specific parameters, a transfer function, transforming peripheral to central arterial blood pressure could be used. The disadvantage of such a transfer function is that it also introduces new uncertainties. Therefore, it might be more beneficial to also study new compliance estimation methods, such as proposed by Arai et al., which claims to be less dependent on the differences between central and peripheral measured blood pressure [53].

4.4.2 Left ventricular flow

The LV flow calculated using the arterial blood pressure and R_{echo} and C_{decay} (SV_{Cdecay}) shows an average difference of 0.88 mL and a range described by the LoA of -0.51 and 2.27 mL. It is evident that this difference between SV_{VTI} and SV_{Cdecay} is small and would therefore probably be clinically useful. To better clinically interpret these values, it is helpful to estimate the cardiac index (CI). The CI is defined as, $\text{CI} = \frac{\text{CO}}{\text{BSA}}$, with BSA the body surface area, which is 1.85 m^2 for an average person with a length of 1.80 m and a weight of 80 kg. A normal value of the CI is above 2.5 L/min/m^2 and a value below 2.0 L/min/m^2 is associated with cardiogenic shock. To translate the LoA for SV_{VTI} and SV_{Cdecay} to CI values, we assume a HR of 80 BPM. The LoA between -0.51 and 2.27 from Figure 14a then correspond with a CI between -0.02 and 0.10 L/min/m^2. These errors would be small enough to make a distinction between a normal CI (above 2.5 L/min/m^2) and a CI associated with cardiogenic shock (below 2.0 L/min/m^2). However, when using C_0 and R_1, as in Figure 14b, the LoA become large, although the average difference is small, 0.26 mL. The LoA between -25.48 and 26.00 mL, correspond to a range for CI between -1.10 and 1.12 L/min/m^2. This range is too large to make a distinction between a normal CI (above 2.5 L/min/m^2) and a CI associated with cardiogenic shock (below 2.0 L/min/m^2). This shows that monitoring SV using the two-element Windkessel model is applicable if the exact values for arterial compliance and venous resistance are known. A relative small error in these parameters can have large influence on the calculated SV.

Figure 15 shows an example of calculate LV flow with the corresponding arterial blood pressure. Despite that a negative flow just before aortic valve closure is expected, the negative flow in Figure 15 is larger than expected [47]. The peak of the positive flow is also larger than expected. The larger negative and larger positive flow cancel each other out in the calculation of the SV, making it possible to have a correct SV, despite showing an unexpected waveform for LV flow. The waveform of the LV flow influences parameters such as the LVOT mean systolic acceleration (LVOTacc), for which Bauer et al. showed a strong correlation with Ees [37]. To be able to use LV flow to continuously

monitor such estimates of Ees, the waveform of the calculated LV flow should be improved. One of the causes of the incorrect waveform might be the simplification of the interaction between blood pressure and flow in the two-element Windkessel model. Improvement of the calculate LV waveform may be possible by using a more elaborate model, such as the three- or four-element Windkessel model, or even one-dimensional models that also take wave transmission and reflection into account.

4.4.3 Strengths and limitations

To proof the principle of LV flow calculations with the two-element Windkessel model in patients supported with VA ECMO, we used data during VA ECMO or HLM support. Data registration in the OR was performed during weaning of the HLM. During weaning, blood flows from both, the heart and the HLM into the arterial system. Similar to the conditions during VA ECMO, the LV and the support device together influence the total hemodynamics. There are however also dissimilarities. Most importantly, with HLM support, central cannulation is used, while VA ECMO in the ICU is usually peripheral cannulated in the femoral artery. In the application of the two-element Windkessel model the site of cannulation is not taken into account, because the Windkessel model is a lumped parameter model, assuming all blood flow enters into one single vessel with a compliance and resistance.

To determine the quality of the calculated SV, we used the SV determined using echocardiographic measurements of the LVOT VTI and dLVOT. Although echocardiography is an accepted method to determine SV, also during VA ECMO, this measurement is also not perfectly accurate. Different studies are performed to study the accuracy of the VTI measurement. The least significant change in VTI that can be trusted between two TTE examinations is around 14% [54], [55]. Blanco et al. showed that the VTI measurements can vary 11% between measurements [50]. Besides the error in the VTI measurements, the measurement of the dLVOT introduces another error. As shown in Equation (9) the SV is proportional to the inverse of the squared radius. Correct estimation of dLVOT is therefore important for accurate SV calculation. For the measurement of dLVOT, it is usually assumed that the LVOT is circular, while in practice the LVOT is elliptical of shape, causing an underestimation of 29% in the area of the LVOT [56]. The calculation of the area could therefore be improved using measurements in multiple directions. Together with the error in the VTI measurement, the error in LVOT diameter can lead to an error up to 43%. Although, in practice the VTI is often overestimated, which is found to compensate for the underestimation of the LVOT area [56]. However, this is not an assurance that the values of SV_{VTI} in our study are correct. The agreement between SV_{VTI} and SV_{Cdecay} is larger than the agreement between two VTI measurements found in the studies described above. The difference we found between SV_{VTI} and SV_{C0R1} is larger, also compared to the difference between two TTE examinations.

In this study, we additionally tested the ability to apply the proposed method, using the two-element Windkessel model and the adapted time-decay method, to eventually continuously monitor the LV. The method we propose for the continuous application of the SV calculation uses the assumption of a constant compliance within one patient. Compliance is determined once, using Equation (1), for which an echocardiography should be performed. Thereafter, the resulted arterial compliance, C_0 is used with the adapted time-decay method to determine vascular resistance R_1 at any moment. Ultimately, these parameter are used in the two-element Windkessel model to repeatedly calculate SV. We studied this method using the available consecutive registrations for different ECMO flows, within one patient. Despite the large LoA range, it is expected that with an improved R estimation, this method can be used to continuously monitor the SV, using a single calibration to determine arterial compliance.

4.4.4 Conclusion

Application of the two-element Windkessel model could be used to accurately determine SV during VA ECMO or HLM support, using known patient specific parameters. The waveform of the LV flow could however not be determined correctly using this simplified representation of the cardiovascular system. Furthermore, correct patient specific parameters are important in the SV calculation and the current estimations are too imprecise for continuous application of the Windkessel model. It is therefore recommended to further improve continuous parameter estimation methods for patients supported with VA ECMO.

5 The additional value of a one-dimensional cardiovascular model to describe the relation between blood pressure and flow in patients supported with VA ECMO

5.1 Introduction

Cardiovascular models are used for various clinical applications, including CO estimation from arterial blood pressure [32]–[34]. The three most used types of cardiovascular models are zero-dimensional models, or lumped parameter models, one-dimensional models and three-dimensional models. All having their own advantages and disadvantages. The choice of the type of model therefore depends on the application. The zero-dimensional model is the least computational expensive, unfortunately at the cost of being an extreme simplification of the entire cardiovascular system. Where the more elaborate three-dimensional model is less simplified and describes the pressure and flow in three dimensions, the computational costs of such a model are large. In terms of computational costs and simplification, the one-dimensional model is between the zero- and three-dimensional model [45].

In this thesis a lumped parameter model is used to calculate LV flow from arterial blood pressure. As discussed above, the lumped parameter model simplifies the calculations. However, the disadvantage is that for this simplification, phenomena such as wave transmission and reflection are ignored. The application of the two-element Windkessel model as described in Section 3 and 4 used arterial blood pressure from the radial artery to estimate flow originating from the LV. When flow from the LV generates a pressure in the radial artery, the phenomena that cannot be described by a zero-dimensional model are involved. Therefore, extension of the model towards a one-dimensional model might improve the quality of the LV flow calculation.

Although we know that the one-dimensional model takes more aspects of the transmission of LV flow into radial artery pressure into account, we do not know if a one-dimensional model would notably improve the calculation of LV flow in patients supported with VA ECMO, compared to the two-element Windkessel model. The aim of this study is therefore to compare the two-element Windkessel model to a one-dimensional distributed parameter model, to determine if the use of a one-dimensional model would be of added value. Zero- and one-dimensional models were compared using transfer functions. Besides, the two-element Windkessel model was compared to a more elaborate lumped parameter model and the effect of inaccurate resistance and compliance estimation was studied.

5.2 Methods

To be able to compare zero- and one-dimensional models, we will use Bode plots of the transfer functions derived from different models. Below, we will explain the models we used and describe the derivation of their transfer functions. In total, we will derive six transfer functions. An overview of all transfer functions is give in Table 5, at the end of this section.

5.2.1 Lumped parameter models

The two-element Windkessel model uses total vascular resistance (R) and arterial compliance (C) to describe the relation between pressure and flow in the cardiovascular system. Figure 16 shows the electrical analogue of this model. The transfer function using left ventricular flow as input and the arterial blood pressure as output of the system, $H_{WK}(s)$, is described by:

$$H_{WK}(s) = \frac{R_{WK}}{1 + R_{WK}C_{WK}s}.$$

$$(10)$$
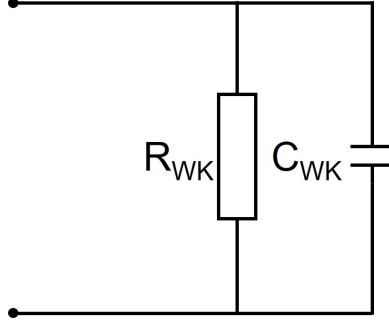
Figure 16: Electrical representation of the two-element Windkessel model.
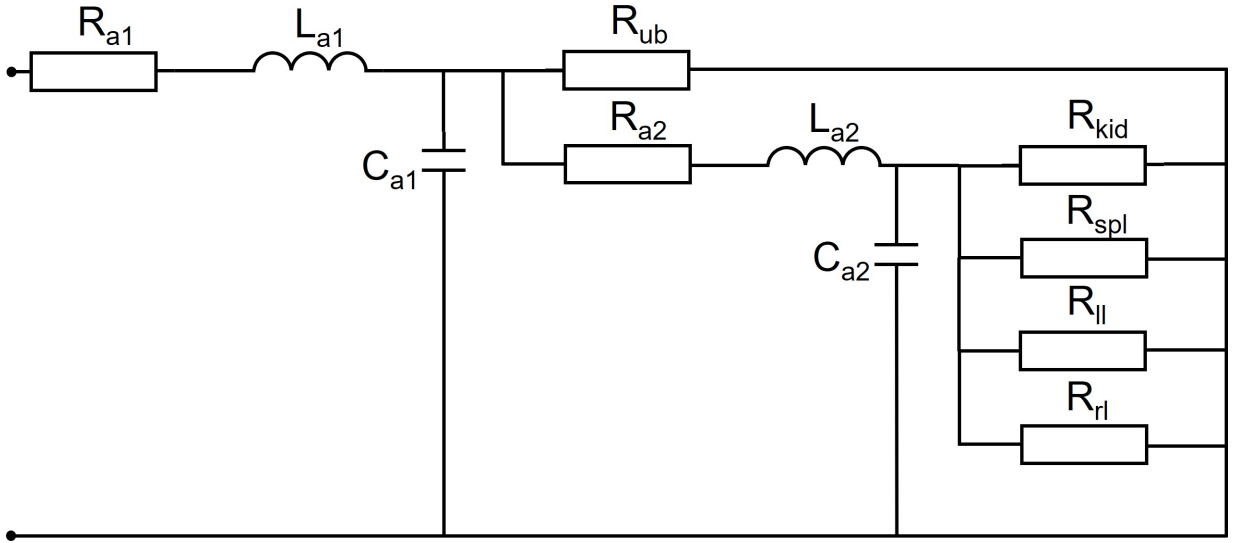
Figure 17: Electrical representation of a part of the model used in the UT simulator.

The cardiovascular simulator of the University of Twente (UT) uses a more elaborate model. Figure 17 shows the electrical analogue of a part of this model. Compared to the two-element Windkessel model, the compliance and resistance are split into several compartments. To be able to correctly compare both transfer functions, the total vascular resistance for the two-element Windkessel model, R_{WK}, was estimated as the equivalent resistance of all resistances in the model of the University of Twente simulator, ignoring the very small venous resistances and other components. Hence,

$$R_p = \frac{1}{\frac{1}{R_{kid}} + \frac{1}{R_{spl}} + \frac{1}{R_{ll}} + \frac{1}{R_{rl}}} \tag{11}$$

$$R_{WK} = \frac{1}{\frac{1}{R_p + R_{a2}} + \frac{1}{R_{ub}}} + R_{a1}. \tag{12}$$

Similarly, the arterial compliance for the two-element Windkessel model, C_{WK}, was estimated as equivalent compliance,

$$C_{WK} = C_{a1} + C_{a2}. \tag{13}$$

Table 3 shows the parameter values used in these calculations. From the electrical analogue in Figure

17, we can derive a transfer function,

$$H_{UT}(s) = \frac{B_1 s^4 + B_2 s^3 + B_3 s^2 + B_4 s + B_5}{B_6 s^3 + B_7 s^2 + B_8 s + B_9}.$$ (14)

for the cardiovascular simulator from the University of Twente using the following coefficients,

$$B_1 = C_{a1}\ C_{a2}\ L_{a1}\ L_{a2}\ R_{ub}\ R_p$$ (15)

$$B_2 = C_{a1}\ C_{a2}\ L_{a1}\ R_{a2}\ R_{ub}\ R_p + C_{a1}\ C_{a2}\ L_{a2}\ R_{a1}\ R_{ub}\ R_p + C_{a1}\ L_{a1}\ L_{a2}\ R_{ub} + C_{a2}\ L_{a1}\ L_{a2}\ R_p$$ (16)

$$B_3 = C_{a1}\ C_{a2}\ R_{a1}\ R_{a2}\ R_{ub}\ R_p + C_{a1}\ L_{a1}\ R_{a2}\ R_{ub} + C_{a1}\ L_{a1}\ R_{ub}\ R_p + C_{a1}\ L_{a2}\ R_{a1}\ R_{ub}$$
$$\quad + C_{a2}\ L_{a1}\ R_{a2}\ R_p + C_{a2}\ L_{a1}\ R_{ub}\ R_p + C_{a2}\ L_{a2}\ R_{a1}\ R_p + C_{a2}\ L_{a2}\ R_{ub}\ R_p + L_{a1}\ L_{a2}$$ (17)

$$B_4 = C_{a1}\ R_{a1}\ R_{a2}\ R_{ub} + C_{a1}\ R_{a1}\ R_{ub}\ R_p + C_{a2}\ R_{a1}\ R_{a2}\ R_p$$
$$\quad + C_{a2}\ R_{a1}\ R_{ub}\ R_p + C_{a2}\ R_{a2}\ R_{ub}\ R_p + L_{a1}\ R_{a2} + L_{a1}\ R_{ub} + L_{a1}\ R_p + L_{a2}\ R_{a1} + L_{a2}\ R_{ub}$$ (18)

$$B_5 = R_{a1}\ R_{a2} + R_{a1}\ R_{ub} + R_{a1}\ R_p + R_{a2}\ R_{ub} + R_{ub}\ R_p$$ (19)

$$B_6 = C_{a1}\ C_{a2}\ L_{a2}\ R_{ub}\ R_p$$ (20)

$$B_7 = C_{a1}\ C_{a2}\ R_{a2}\ R_{ub}\ R_p + C_{a1}\ L_{a2}\ R_{ub} + C_{a2}\ L_{a2}\ R_p$$ (21)

$$B_8 = C_{a1}\ R_{a2}\ R_{ub} + C_{a1}\ R_{ub}\ R_p + C_{a2}\ R_{a2}\ R_p + C_{a2}\ R_{ub}\ R_p + L_{a1}$$ (22)

$$B_9 = R_{a2} + R_{ub} + R_p.$$ (23)

A simple calculation gives $\frac{B_5}{B_9} = R_{WK}$, see Equation (12). So at $s = 0$ the transfer function of the two-element Windkessel model is equal to the transfer function of the model of the UT simulator as shown in Figure 17.

Table 3: Parameter values for the lumped parameter models.

Parameter	Value	Unit
C_{a1}	0.660	mL/mmHg
C_{a2}	0.550	mL/mmHg
L_{a1}, L_{a2}	$5 \cdot 10^{-5}$	mmHg·s^2/mL
R_{kid}	3.19	mmHg·s/mL
R_{spl}	2.34	mmHg·s/mL
R_{ll}, R_{rl}	5.58	mmHg·s/mL
R_{ub}	3.00	mmHg·s/mL
R_{a1}	0.013	mmHg·s/mL
R_{a2}	0.009	mmHg·s/mL
R_{ub}	3.00	mmHg·s/mL
R_{WK}	0.716	mmHg·s/mL
C_{WK}	1.21	mL/mmHg

5.2.2 One-dimensional Navier-Stokes

The lumped parameter models were compared to a one-dimensional distributed parameter model. The one-dimensional model for this study should describe flow in a compliant tube. The three-dimensional Navier-Stokes equations describe such a flow, assuming a laminar flow and an incompressible fluid [57]. The one-dimensional Navier-Stokes equations were derived from this, assuming there is a flat velocity profile, except at the walls, where the flow becomes zero within a thin layer (δ). Additionally, it is assumed that the pressure is constant over the cross-sectional area of the vessel and the blood density ρ is also a constant. The resulting, one-dimensional Navier-Stokes equations we use in this study are,

$$\frac{\partial A}{\partial t} + \frac{\partial q}{\partial x} = 0 \tag{24}$$

$$\frac{\partial q}{\partial t} + \frac{\partial}{\partial x}\left(\frac{q^2}{A}\right) + \frac{A}{\rho}\frac{\partial p}{\partial x} = -\frac{2\pi\nu r_0}{\delta}\frac{q}{A}. \tag{25}$$

With the cross-sectional vessel area A, the blood flow q and the blood pressure p dependent on time t and location on the vessel x. The first equation is the one-dimensional derivation of the continuity equation. The second equation represents the momentum equation, with the fluid acceleration explained by the first two terms and the forces on the fluid by the other terms. The right-hand side represents the viscous stress on the wall, with kinematic viscosity ν. The viscous term in the longitudinal direction is neglected, since it is small compared to this right-hand side [58]. With Equation (24) and (25), we have two equations with three unknowns, q, A and p. Therefore a third equation was used to be able to solve the system of equations. This third equation describes the relation between cross-sectional blood vessel area A and pressure p. Several options exist to describe this relation, assuming an elastic wall. We choose to use,

$$p = \frac{4}{3}\frac{Eh}{r_0}\left(1 - \sqrt{\frac{A_0}{A}}\right). \tag{26}$$

With E Young's modulus, h the thickness of the vessel wall, r_0 the unstressed radius at $p = 0$ mmHg and $A_0 = \pi r_0^2$.

5.2.2.1 *Boundary conditions*

For the model described by Equations (24), (25) and (26), two boundary conditions are necessary, one at each end of the vessel, represented by a and b in Figure 18.

At side a, where the heart is, we assume a certain flow from the left ventricle, $u(t)$,

$$q(a,t) = u(t). \tag{27}$$

In this study we used $a = 0$ as the start of the one-dimensional vessel.

At side b, the brachial artery ends and is coupled to a two-element Windkessel model to relate the blood pressure and the blood flow, described by

$$q(b,t) = \frac{p(b,t)}{R_b} + C_b\frac{dp(b,t)}{dt}. \tag{28}$$

Figure 18: Schematic representation of the vessel described by the one-dimensional Navier-Stokes equations, with boundaries at the side of the LV, $x = a$ and at the radial artery $x = b$.

5.2.3 Parameter values for the one-dimensional Navier-Stokes equation

To be able to apply the described one-dimensional model, parameter values were needed for all parameters involved. We assumed one single vessel from the LV towards the start of the radial artery, without branches or tapering. The dimensions of the single vessel were determined using the dimensions of all the vessels in the assumed trajectory. Table 4 shows the estimates used for length, radius and wall thickness of the different parts of this trajectory [58], [59]. The length of the single vessel is the total length of all the segments. The radius is set such that the total resistance of the single vessel equals the sum of the resistances of the different segments. For resistance (R_t), Poiseuille's law for resistance in a tube was used,

$$R_t = \frac{8L\eta}{\pi r^4}, \tag{29}$$

with L the length of the tube, η a viscosity constant and r the internal radius of the tube [38]. The wall thickness of the single vessel is calculated as the weighted thickness, using the segment length as weight. The result was a single vessel with a length (b) of 52.8 cm, a radius (r_0) of 0.38 cm and a wall thickness (h) of 0.088 cm. Values for r_0 and h were used to determine values for $\frac{Eh}{r_0}$, with Young's

Table 4: Estimated geometry of the arteries from the left ventricle to the brachial artery [58], [59].

Artery	Length [cm]	Radius [cm]	Wall thickness [cm]
Ascending aorta	7	1.20	0.164
Aortic arc part 1	1.8	1.13	0.151
Aortic arc part 2	1	1.10	0.151
Subclavian + Brachial artery	43	0.36	0.071
Single 1D vessel	**52.8**	**0.38**	**0.088**

modulus $E = 4 \cdot 10^6 \frac{g}{cm \cdot s^2}$ [59]. To fit with the units of the other parameters, the unit for pressure used is $\frac{g}{cm \cdot s^2} = 7.5 \cdot 10^{-4}$ mmHg.

When using the two-element Windkessel model as a boundary condition for the one-dimensional Navier-Stokes equations, the values for resistance and compliance are different compared to the Windkessel model that describes the entire arterial system. The coupled Windkessel model only describes the vascular system after the brachial artery, with a higher resistance and a lower compliance than the total arterial system. To estimate values for the resistance (R_b) and compliance (C_b) of the coupled Windkessel model we used values of the radial artery compartments described by Westerhof et al., assuming resistances in series and compliances in parallel [59]. Resulting in $R_b = 1.8304 \cdot 10^4 \frac{g}{cm^4 s} = 13.72 \frac{mmHg \cdot s}{mL}$ and $C_b = 1.877 \cdot 10^{-6} \frac{cm^4 s^2}{g} = 2.5 \cdot 10^{-3} \frac{mL}{mmHg}$.

5.2.4 Transfer functions for partial differential equations

For linear time-invariant systems described with ordinary differential equations such as the above described lumped parameter models, the application and derivation of transfer functions are common. The associated transfer functions are rational functions. For linear time-invariant partial differential equations however, the transfer functions are irrational, often having infinite or no poles and zeros. Moreover, the boundary conditions are of large influence on the location of the poles and the zero's and therefore the stability of the system [60]. The system described by the one-dimensional Navier-Stokes equations, Equation (24) and (25), is non-linear. However, an irrational transfer functions can only be described for linear partial differential equations. The next sections describe how the transfer function is obtained for these non-linear equations, starting by linearizing the equations around a steady-state solution. We obtained the steady-state solution in two situations, 1) when the blood has a viscosity of zero, $\nu = 0$ and 2) when there is no blood flow. The transfer function is derived with two different boundary conditions: 1) a given flow at both ends of the vessel and 2) coupled to a two-element Windkessel model at the end of the brachial artery.

5.2.5 Inviscid fluid

We first derived the transfer function for a fluid without viscosity, $\nu = 0$. Hence, the right-hand side of Equation (25) becomes zero.

5.2.5.1 *Steady-state solution*

For $\nu = 0$, the one-dimensional Navier-Stokes equations are,

$$\frac{\partial A}{\partial t} + \frac{\partial q}{\partial x} = 0 \tag{30}$$

$$\frac{\partial q}{\partial t} + \frac{\partial}{\partial x}\left(\frac{q^2}{A}\right) + \frac{A}{\rho}\frac{\partial p}{\partial x} = 0. \tag{31}$$

In the steady state q and A need to be independent of t, using Equation (30): $\frac{\partial q}{\partial x} = 0$. For the steady state solution, $q(a) = q(b) = q_{eq}$ with q_{eq} a constant flow. Since we have the boundary conditions in Equations (27) and (28). Using these constants in Equation (31) with (26),

$$\left(\frac{-q^2}{A^2} + \frac{1}{\rho}\frac{4}{3}\frac{Eh}{r_0}\frac{\sqrt{A_0}}{2}\frac{1}{\sqrt{A}}\right)\frac{dA}{dx} = 0. \tag{32}$$

Which gives,

$$A = \left(\frac{q^2}{\frac{1}{\rho}\frac{4}{3}\frac{Eh}{r_0}\frac{\sqrt{A_0}}{2}}\right)^{2/3} \vee \frac{dA}{dx} = 0. \tag{33}$$

Both solutions give that in the steady state A is constant over the length of the vessel. The steady state solution for the one-dimensional Navier-Stokes equations, assuming an inviscid fluid, is given by the constants q_{eq} and A_{eq}. This steady state solution should also satisfy the boundary conditions at both ends. Since q_{eq} is a constant flow, the boundary condition at $x = a$ is satisfied. For the boundary condition at $x = b$, we have Equation (28), together with Equation (26),

$$q_{eq} = \frac{4}{3R_b}\frac{Eh}{r_0}\left(1 - \sqrt{\frac{A_0}{A_{eq}}}\right). \tag{34}$$

We choose $q_{eq} = 33$ mL/s, which is a low ECMO flow of 2 L/min, resulting in $A_{eq} = 1.732$ cm^2.

5.2.5.2 *Linearization*

The system was linearized around the steady state solution q_{eq} and A_{eq}. In Equation (30) and (31), $A = A_{eq} + A_v$ and $q = q_{eq} + q_v$ was substituted, where A_v and q_v represent the variable part of respectively the cross-sectional vessel area and the blood flow,

$$\frac{\partial A_v}{\partial t} + \frac{\partial q_v}{\partial x} = 0 \tag{35}$$

$$\frac{\partial q_v}{\partial t} + \frac{\partial}{\partial x}\left(\frac{(q_{eq}+q_v)^2}{(A_{eq}+A_v)}\right) + \frac{(A_{eq}+A_v)}{\rho}\frac{\partial p}{\partial x} = 0, \tag{36}$$

where we used that q_{eq} and A_{eq} are constants. Substituting Equation (35) into Equation (36),

$$\frac{\partial q_v}{\partial t} + 2\frac{\partial q_v}{\partial x}\left(\frac{q_v}{A_{eq}+A_v}\right) + 2\frac{\partial q_v}{\partial x}\left(\frac{q_{eq}}{A_{eq}+A_v}\right) - \frac{\partial A_v}{\partial x}\frac{q_{eq}^2}{(A_{eq}+A_v)^2}$$
$$- \frac{\partial A_v}{\partial x}\frac{q_v^2}{(A_{eq}+A_v)^2} - \frac{\partial A_v}{\partial x}\frac{2q_{eq}q_v}{(A_{eq}+A_v)^2} + \frac{A_v}{\rho}\frac{\partial p}{\partial x} + \frac{A_{eq}}{\rho}\frac{\partial p}{\partial x} = 0. \tag{37}$$

This equation still includes the non-linear parts, $\frac{1}{(A_{eq}+A_v)}$ and $\frac{1}{(A_{eq}+A_v)^2}$. For further linearization, these elements were described using a Taylor expansion around $A_v = 0$,

$$\frac{1}{(A_{eq}+A_v)} \approx \frac{1}{A_{eq}} - \frac{A_v}{A_{eq}^2} + \mathcal{O}(A_v^2) \tag{38}$$

$$\frac{1}{(A_{eq}+A_v)^2} \approx \frac{1}{A_{eq}^2} - \frac{2A_v}{A_{eq}^3} + \mathcal{O}(A_v^2), \tag{39}$$

in which we ignore A_v^2 and higher order terms, since A_v is small. Substitute this into Equation (37),

$$\frac{\partial q_v}{\partial t} + 2\frac{\partial q_v}{\partial x}\frac{q_v}{A_{eq}} - 2\frac{\partial q_v}{\partial x}\frac{q_v A_v}{A_{eq}^2} + 2\frac{\partial q_v}{\partial x}\frac{q_{eq}}{A_{eq}} - 2\frac{\partial q_v}{\partial x}\frac{q_{eq}A_v}{A_{eq}^2} - \frac{\partial A_v}{\partial x}\frac{q_{eq}^2}{A_{eq}^2} + 2\frac{\partial A_v}{\partial x}\frac{q_{eq}^2 A_v}{A_{eq}^3}$$
$$- \frac{\partial A_v}{\partial x}\frac{q_v^2}{A_{eq}^2} + 2\frac{\partial A_v}{\partial x}\frac{q_v^2 A_v}{A_{eq}^3} - \frac{\partial A_v}{\partial x}\frac{2q_0 q_v}{A_{eq}^2} + 2\frac{\partial A_v}{\partial x}\frac{2q_{eq}q_v A_v}{A_{eq}^3} + \frac{A_v}{\rho}\frac{\partial p}{\partial x} + \frac{A_{eq}}{\rho}\frac{\partial p}{\partial x} = 0. \tag{40}$$

The components q_v and A_v are small, hence Equation (40) can be simplified by neglecting all non-linear terms with q_v and A_v. Thus, the linearized system for an inviscid fluid in a single vessel is given by the system of partial differential equations,

$$\frac{\partial A_v}{\partial t} + \frac{\partial q_v}{\partial x} = 0 \tag{41}$$

$$\frac{\partial q_v}{\partial t} + 2\frac{\partial q_v}{\partial x}\frac{q_{eq}}{A_{eq}} - \frac{\partial A_v}{\partial x}\frac{q_{eq}^2}{A_{eq}^2} + \frac{A_{eq}}{\rho}\frac{\partial p}{\partial x} = 0. \tag{42}$$

To be able to apply the relation between the cross-sectional area A and pressure p, a Taylor expansion of Equation (26) around $A = A_{eq}$ was used,

$$p \approx p_{eq} + \frac{4}{3}\frac{Eh}{r_0}\left(\frac{1}{2}\frac{\sqrt{A_0}A_v}{A_{eq}\sqrt{A_{eq}}}\right). \tag{43}$$

The pressure p is also substituted with a steady state (p_{eq}) and variable (p_v) part, where p_{eq} is the pressure for $A = A_{eq}$,

$$p_{eq} = \frac{4}{3} \frac{Eh}{r_0} \left(1 - \sqrt{\frac{A_0}{A_{eq}}} \right). \tag{44}$$

Hence, the variable part of the pressure $p_v = p - p_{eq}$,

$$p_v \approx \frac{4}{3} \frac{Eh}{r_0} \frac{1}{2} \frac{\sqrt{A_0} A_v}{A_{eq} \sqrt{A_{eq}}}. \tag{45}$$

The boundary conditions are already linear and are therefore still described by Equation (27) and (28).

5.2.5.3 *Transfer function*

To derive the transfer function for the linearized one-dimensional Navier-Stokes equations with an inviscid fluid, Equation (45) is substituted into Equations (41) and (42), with $k_1 = \frac{q_{eq}}{A_{eq}}$ and $k_2 = \frac{1}{\rho} \frac{2}{3} \frac{Eh}{r_0} \frac{\sqrt{A_0}}{\sqrt{A_{eq}}}$. To construct a transfer function we apply the Laplace transform to the systems of partial differential equations to obtain the system of ordinary differential equations,

$$\begin{cases} sA_v + \frac{\partial q_v}{\partial x} = 0 \\ sq_v + 2k_1 \frac{\partial q_v}{\partial x} - \frac{\partial A_v}{\partial x} k_1^2 + k_2 \frac{\partial A_v}{\partial x} = 0. \end{cases} \tag{46}$$

In matrix notation,

$$\begin{bmatrix} \frac{\partial q_v}{\partial x} \\ \frac{\partial A_v}{\partial x} \end{bmatrix} = \begin{bmatrix} 0 & -s \\ \frac{-s}{k_2 - k_1^2} & \frac{2k_1 s}{k_2 - k_1^2} \end{bmatrix} \begin{bmatrix} q_v \\ A_v \end{bmatrix}. \tag{47}$$

With eigenvalues and corresponding eigenvectors,

$$\lambda_1 = \frac{-s}{\sqrt{k_2} + k_1}, \qquad\qquad v_1 = \begin{bmatrix} \sqrt{k_2} + k_1 \\ 1 \end{bmatrix}, \tag{48}$$

$$\lambda_2 = \frac{s}{\sqrt{k_2} - k_1}, \qquad\qquad v_2 = \begin{bmatrix} -\sqrt{k_2} + k_1 \\ 1 \end{bmatrix}. \tag{49}$$

Hence, the general solution,

$$q_v(x) = \alpha \left(\sqrt{k_2} + k_1 \right) e^{\lambda_1 x} + \beta \left(-\sqrt{k_2} + k_1 \right) e^{\lambda_2 x} \tag{50}$$

$$A_v(x) = \alpha e^{\lambda_1 x} + \beta e^{\lambda_2 x}. \tag{51}$$

It appears we might divide by zero for $k_2 - k_1^2 = 0$. In this situation, the system described by Equation (46) becomes,

$$sq_v - 2k_1 s A_v = 0 \tag{52}$$

and therefore the transfer function becomes scalar $\frac{1}{2k_1}$. However, substituting the parameters values described in Section 5.2.3, we find $k_2 \gg k_1^2$, therefore this situation will not occur.

Using Equation (50), α and β can be expressed in the flow at the boundaries $q_v(0)$ and $q_v(b)$,

$$\begin{bmatrix} \alpha \\ \beta \end{bmatrix} = \frac{1}{e^{\lambda_2 b} - e^{\lambda_1 b}} \begin{bmatrix} e^{\lambda_2 b} \frac{1}{(\sqrt{k_2}+k_1)} & \frac{-1}{(\sqrt{k_2}+k_1)} \\ -e^{\lambda_1 b} \frac{1}{(-\sqrt{k_2}+k_1)} & \frac{1}{(-\sqrt{k_2}+k_1)} \end{bmatrix} \begin{bmatrix} q_v(0) \\ q_v(b) \end{bmatrix}. \tag{53}$$

Using this expression of α and β in Equation (51),

$$\begin{bmatrix} A_v(0) \\ A_v(b) \end{bmatrix} = \frac{1}{e^{\lambda_2 b} - e^{\lambda_1 b}} \begin{bmatrix} \frac{e^{\lambda_2 b}}{\sqrt{k_2}+k_1} - \frac{e^{\lambda_1 b}}{-\sqrt{k_2}+k_1} & \frac{-1}{\sqrt{k_2}+k_1} + \frac{1}{-\sqrt{k_2}+k_1} \\ \frac{e^{(\lambda_1+\lambda_2)b}}{\sqrt{k_2}+k_1} - \frac{e^{(\lambda_1+\lambda_2)b}}{-\sqrt{k_2}+k_1} & \frac{-e^{\lambda_1 b}}{\sqrt{k_2}+k_1} + \frac{e^{\lambda_2 b}}{-\sqrt{k_2}+k_1} \end{bmatrix} \begin{bmatrix} q_v(0) \\ q_v(b) \end{bmatrix}. \tag{54}$$

Which we express as,

$$\begin{bmatrix} A_v(0) \\ A_v(b) \end{bmatrix} = \begin{bmatrix} G_{11}(s) & G_{12}(s) \\ G_{21}(s) & G_{22}(s) \end{bmatrix} \begin{bmatrix} q_v(0) \\ q_v(b) \end{bmatrix}, \tag{55}$$

with,

$$G_{11}(s) = \frac{e^{\lambda_2 b}}{(\sqrt{k_2}+k_1)(e^{\lambda_2 b} - e^{\lambda_1 b})} - \frac{e^{\lambda_1 b}}{(k_1 - \sqrt{k_2})(e^{\lambda_2 b} - e^{\lambda_1 b})},$$

$$G_{21}(s) = \frac{2\sqrt{k_2}e^{(\lambda_1+\lambda_2)b}}{(\sqrt{k_2}-k_1)(\sqrt{k_2}+k_1)(e^{\lambda_2 b} - e^{\lambda_1 b})},$$

$$G_{21}(s) = \frac{2\sqrt{k_2}e^{(\lambda_1+\lambda_2)b}}{(\sqrt{k_2}-k_1)(\sqrt{k_2}+k_1)(e^{\lambda_2 b} - e^{\lambda_1 b})},$$

$$G_{22}(s) = \frac{e^{\lambda_2 b}}{(k_1 - \sqrt{k_2})(e^{\lambda_2 b} - e^{\lambda_1 b})} - \frac{e^{\lambda_1 b}}{(\sqrt{k_2}+k_1)(e^{\lambda_2 b} - e^{\lambda_1 b})},$$

where λ_1 and λ_2 both depend on s. The system was first studied without coupling to the two-element Windkessel model. At both ends, a and b, the flow will be a fixed value. Hence, as shown in Equation (55), for an inviscid fluid with a fixed flow at both boundaries the transfer function from $q_v(0)$ to $A_v(b)$ is,

$$H_{NSv0}(s) = G_{21}(s). \tag{56}$$

5.2.5.3.1 *Coupled to the Windkessel model*

Next, the Windkessel model was added as a boundary condition at $x = b$, described by Equation (28). Applying a Laplace transform and the linear relation between p_v and A_v at $x = b$,

$$q_v(b) = WK(s)A_v(b) \tag{57}$$

with,

$$WK(s) = \frac{\rho k_2}{A_{eq}}\left(\frac{1}{R_b} + C_b s\right). \tag{58}$$

To describe the transfer function for the system coupled to a two-element Windkessel model, we use Equation (55) and (57),

$$A_v(b) = G_{21}(s) \cdot q_v(0) + G_{22}(s) \cdot WK(s) \cdot A_v(b). \tag{59}$$

So, the transfer function from $q_v(0)$ to $A_v(b)$ for the one-dimensional model with an inviscid fluid, coupled to a two-element Windkessel model is described by,

$$H_{NS\nu0WK}(s) = \frac{G_{21}(s)}{1 - G_{22}(s)WK(s)}.$$

(60)

5.2.6 Viscous fluid

Since blood does not have a viscosity of zero, we also studied the transfer function of a system when the viscosity is nonzero.

5.2.6.1 *Steady-state solution*

To find a constant steady-state solution for the system when the viscocity is nonzero, we used the assumption that there is no flow in the steady state, $q_{eq} = 0$. The one-dimensional Navier-Stokes equations with this assumption are,

$$\frac{\partial A}{\partial t} = 0$$

(61)

$$\frac{A}{\rho}\frac{\partial p}{\partial x} = 0.$$

(62)

The steady-state solution was found by substituting Equation (26) into Equation (62),

$$\frac{1}{\rho}\frac{4}{3}\frac{Eh}{r_0}\frac{\sqrt{A_0}}{2}\frac{1}{\sqrt{A}}\frac{dA}{dx} = 0.$$

(63)

Therefore, A is a constant in the steady state. The values for A_{eq} and q_{eq} also need to satisfy the boundary condition at both ends. The boundary condition at $x = a$ is satisfied since q_{eq} is a constant. For the boundary condition at $x = b$ we again use Equation (34) with $q_{eq} = 0$, to obtain $A_{eq} = A_0$ for the steady state solution.

5.2.6.2 *Linearization*

The system for viscous fluid is linearized around the steady state solution. Again, by substituting $A = A_{eq} + A_v$ and $q = q_{eq} + q_v$ with $q_{eq} = 0$ in Equations (24) and (25),

$$\frac{\partial A_v}{\partial t} + \frac{\partial q_v}{\partial x} = 0$$

(64)

$$\frac{\partial q_v}{\partial t} + \frac{\partial}{\partial x}\left(\frac{q_v^2}{(A_{eq} + A_v)}\right) + \frac{(A_{eq} + A_v)}{\rho}\frac{\partial p}{\partial x} = -\frac{2\pi\nu r_0 q_v}{\delta(A_{eq} + A_v)}.$$

(65)

The linearized system was obtained using Equation (38) and (45) and neglecting all non-linear terms that include A_v or q_v,

$$\frac{\partial A_v}{\partial t} + \frac{\partial q_v}{\partial x} = 0$$

(66)

$$\frac{\partial q_v}{\partial t} + k_2\frac{\partial A_v}{\partial x} = -k_3 q_v,$$

(67)

where $k_2 = \frac{1}{\rho}\frac{2}{3}\frac{Eh}{r_0}\frac{\sqrt{A_0}}{\sqrt{A_{eq}}}$ again, and $k_3 = \frac{2\pi\nu r_0}{\delta A_{eq}}$. This is the linearized system we used to derive the transfer function.

5.2.6.3 *Transfer function*

To derive the transfer function for the linearized one-dimensional Navier-Stokes with a viscous fluid, the Laplace transformation is applied to Equation (66) and (67), to obtain the ordinary differential equations,

$$\begin{cases} sA_v + \frac{\partial q_v}{\partial x} = 0 \\ sq_v + k_2\frac{\partial A_v}{\partial x} = -k_3 q_v. \end{cases} \tag{68}$$

In matrix notation,

$$\begin{bmatrix} \frac{\partial q_v}{\partial x} \\ \frac{\partial A_v}{\partial x} \end{bmatrix} = \begin{bmatrix} 0 & -s \\ \frac{-k_3-s}{k_2} & 0 \end{bmatrix} \begin{bmatrix} q_v \\ A_v \end{bmatrix}. \tag{69}$$

With eigenvalues and corresponding eigenvectors,

$$\lambda_3 = \frac{-\sqrt{k_2 s(-k_3-s)}}{-k_3-s}, \qquad v_3 = \begin{bmatrix} \frac{-\sqrt{-k_2 s(-k_3-s)}}{k_2} \\ 1 \end{bmatrix} = \begin{bmatrix} v_q \\ 1 \end{bmatrix}, \tag{70}$$

$$\lambda_4 = \frac{\sqrt{k_2 s(-k_3-s)}}{-k_3-s} = -\lambda_3, \qquad v_4 = \begin{bmatrix} \frac{\sqrt{-k_2 s(-k_3-s)}}{k_2} \\ 1 \end{bmatrix} = \begin{bmatrix} -v_q \\ 1 \end{bmatrix}. \tag{71}$$

Hence, the general solution,

$$q_v(x) = -\alpha v_q e^{-\lambda_3 x} + \beta v_q e^{\lambda_3 x} \tag{72}$$

$$A_v(x) = \alpha e^{-\lambda_3 x} + \beta e^{\lambda_3 x}. \tag{73}$$

With Equation (72) from this general solution we can express α and β using $q_v(0)$ and $q_v(b)$, similar to Section 5.2.5,

$$\begin{bmatrix} \alpha \\ \beta \end{bmatrix} = \frac{1}{e^{-\lambda_3 b} - e^{\lambda_3 b}} \begin{bmatrix} \frac{e^{\lambda_3 b}}{v_q} & \frac{-1}{v_q} \\ \frac{e^{-\lambda_3 b}}{v_q} & \frac{-1}{v_q} \end{bmatrix} \begin{bmatrix} q_v(0) \\ q_v(b) \end{bmatrix}. \tag{74}$$

Using Equation (73) and (74),

$$\begin{bmatrix} A_v(0) \\ A_v(b) \end{bmatrix} = \frac{1}{e^{-\lambda_3 b} - e^{\lambda_3 b}} \begin{bmatrix} \frac{e^{-\lambda_3 b}e^{\lambda_3 b}}{v_q} & \frac{-2}{v_q} \\ \frac{2}{v_q} & \frac{-e^{-\lambda_3 b\lambda^2}-e^{\lambda_3 b}}{v_q} \end{bmatrix} \begin{bmatrix} q_v(0) \\ q_v(b) \end{bmatrix}. \tag{75}$$

Which we write as,

$$\begin{bmatrix} A_v(0) \\ A_v(b) \end{bmatrix} = \begin{bmatrix} F_{11}(s) & F_{12}(s) \\ F_{21}(s) & F_{22}(s) \end{bmatrix} \begin{bmatrix} q_v(0) \\ q_v(b) \end{bmatrix}, \tag{76}$$

with,

$$F_{11}(s) = \frac{e^{-\lambda_3 b} + e^{\lambda_3 b}}{v_q\left(e^{-\lambda_3 b} - e^{\lambda_3 b}\right)} \tag{77}$$

$$F_{12}(s) = \frac{-2}{v_q\left(e^{-\lambda_3 b} - e^{\lambda_3 b}\right)} \tag{78}$$

$$F_{21}(s) = \frac{2}{v_q\left(e^{-\lambda_3 b} - e^{\lambda_3 b}\right)} \tag{79}$$

$$F_{22}(s) = \frac{-e^{-\lambda_3 b} - e^{\lambda_3 b}}{v_q\left(e^{-\lambda_3 b} - e^{\lambda_3 b}\right)}, \tag{80}$$

where λ_3 and v_q both depend on s. The transfer function was first determined using a fixed value for the flow at both ends, $q_v(0)$ and $q_v(b)$. The resulting transfer function from $q_v(0)$ to $A_v(b)$ for the one-dimensional Navier-Stokes equations, linearized around $q_{eq} = 0$ with a viscous fluid is,

$$H_{NSq0}(s) = F_{21}(s). \tag{81}$$

5.2.6.3.1 *Coupled to the Windkessel model*

Additionally, for the one-dimensional Navier-Stokes equations with viscous fluid, the transfer function was also derived for the system coupled to a Windkessel model. To describe this transfer function, we again used the Laplace transformation of the Windkessel boundary condition in Equation (58). Further, Equation (76) is used to obtain,

$$A_v(b) = F_{21}(s) \cdot q_v(0) + F_{22}(s) \cdot WK(s) \cdot A_v(b). \tag{82}$$

Therefore, the transfer function from $q_v(0)$ to $A_v(b)$ for the one-dimensional model with a viscous fluid, coupled to a two-element Windkessel model is describe by,

$$H_{NSq0WK}(s) = \frac{F_{21}(s)}{1 - F_{22}(s)WK(s)}. \tag{83}$$

Table 5: Overview of the different transfer functions

Transfer function	Model	Boundary Conditions	Steady-state assumption
$H_{WK}(s)$	Two-element Windkessel	-	-
$H_{UT}(s)$	UT simulator	-	-
$H_{NS\nu0}(s)$	One-dimensional Navier-Stokes	$q(a) = u_1$, $q(b) = u_2$	Inviscid fluid
$H_{NS\nu0WK}(s)$	One-dimensional Navier-Stokes	$q(a) = u_1$, $q(b) = \frac{p(b)}{R} + C\frac{dp(b)}{dt}$	Inviscid fluid
$H_{NSq0}(s)$	One-dimensional Navier-Stokes	$q(a) = u_1$, $q(b) = u_2$	Zero flow
$H_{NSq0WK}(s)$	One-dimensional Navier-Stokes	$q(a) = u_1$, $q(b) = \frac{p(b)}{R} + C\frac{dp(b)}{dt}$	Zero flow

5.3 Results

5.3.1 Lumped parameter models

Figure 19a shows the Bode plot of the transfer function $H_{WK}(s)$ and $H_{UT}(s)$, together with $H_{WK}(s)$ using a deviation of 30 or 50% in the resistance, Figure 19a shows the results over a wide range of frequencies, Figure 19b focuses on the frequencies until 20 Hz. Changing the resistance shows the largest effect for the lower frequencies, around 1 Hz both the magnitude and phase plot are similar for the different resistances. Figure 20 shows the same results for adjustments in the compliances. These changes show the largest effect above 0.1 Hz.
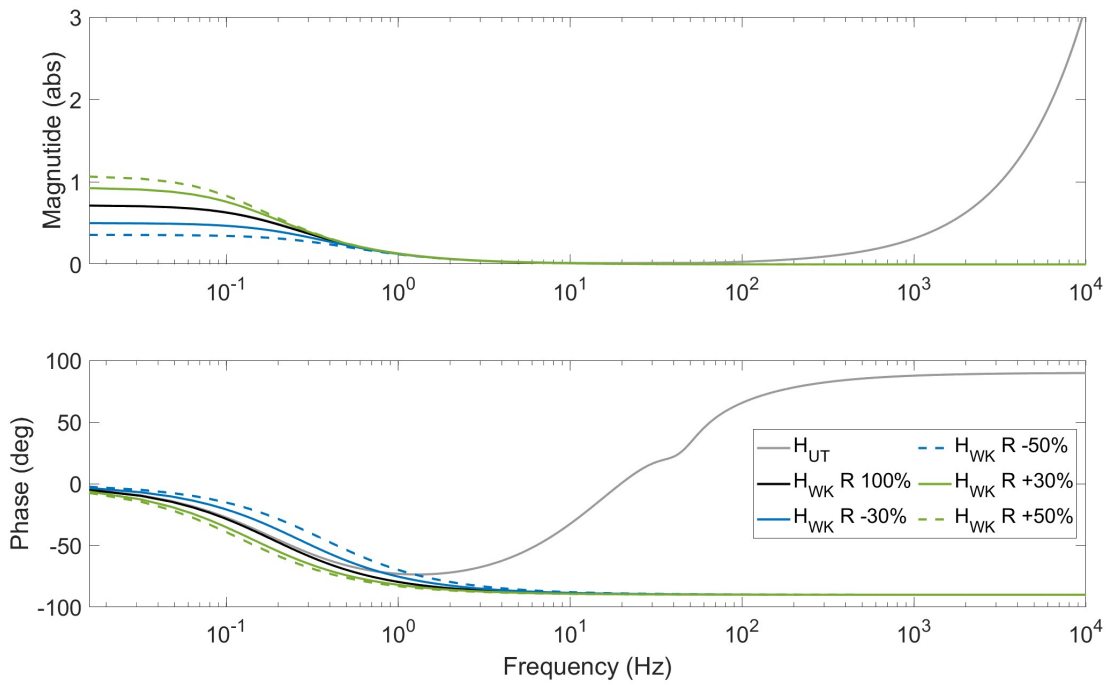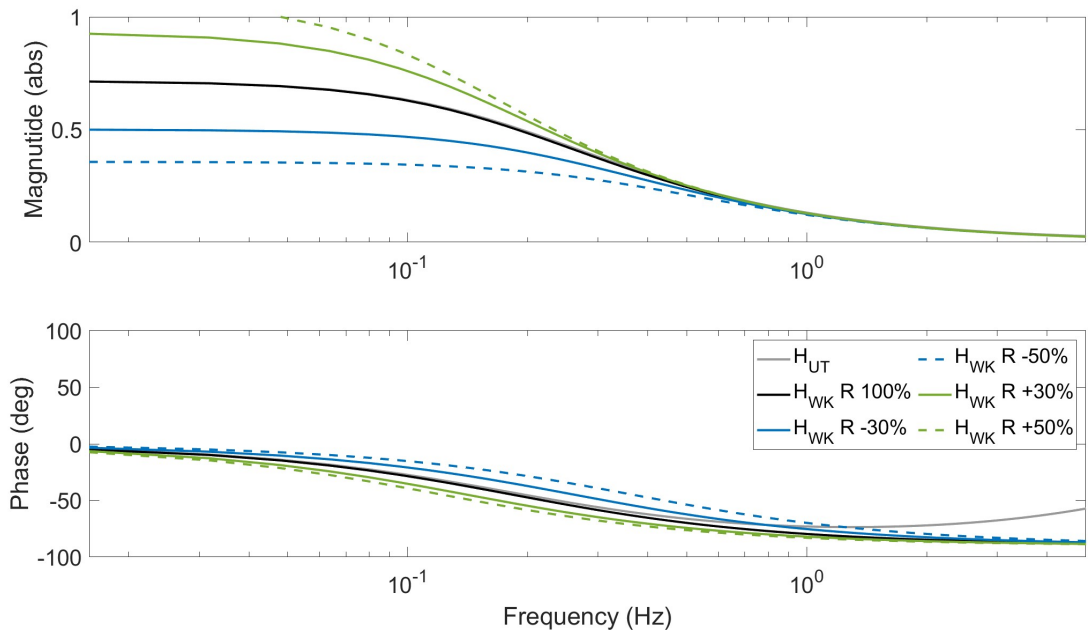
Figure 19: Bode plots of $H_{UT}(s)$ and of $H_{WK}(s)$, using resistance R varying from -50 to +50% of R_{WK}. Over a) a wide frequency range and b) focused between 0 and 20 Hz.
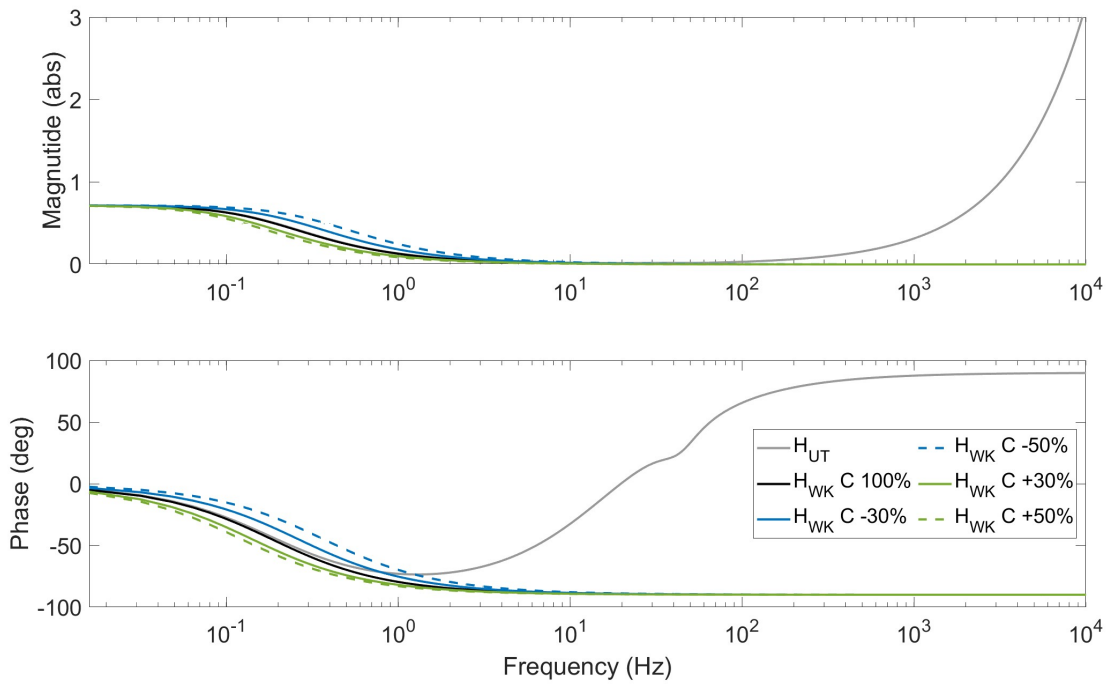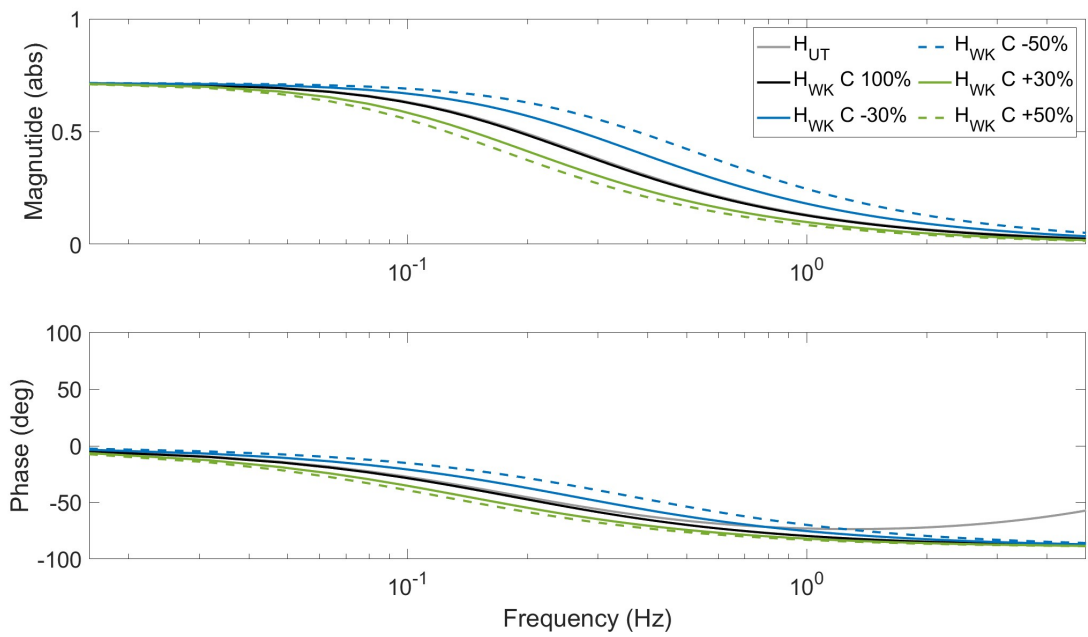
Figure 20: Bode plots of $H_{UT}(s)$ and of $H_{WK}(s)$, using compliance C varying from -50 to +50% of C_{WK}. Over a) a wide frequency range and b) focused between 0 and 20 Hz.

5.3.2 One-dimensional Navier-Stokes equations

To be able to compare the Bode plots of the lumped parameter models to the Bode plots of the one-dimensional models, we used two factors. First, the transfer functions of the one-dimensional models is multiplied by $\frac{2}{3}\frac{Eh}{r_0}\frac{\sqrt{A_0}}{A_{eq}\sqrt{A_{eq}}}$, according to Equation (45), to obtain a transfer function with pressure p, instead of cross-sectional vessel area A as output and additionally the pressure in $\frac{g}{cm \cdot s^2}$ is multiplied with $7.5 \cdot 10^{-4}$, to obtain a pressure in mmHg. Next, $H_{NS\nu0}(s)$, $H_{NS\nu0WK}(s)$, $H_{NSq0}(s)$ and $H_{NSq0WK}(s)$ are multiplied by an extra correction factor, $M_{\nu0}$ or M_{q0} such that respectively the magnification of $H_{NS\nu0WK}(s)$ or $H_{NSq0WK}(s)$ equals the magnification of $H_{WK}(s)$ at the HR of 100 BPM (1.67 Hz). These extra correction factors $M_{\nu0}$ and M_{q0} equal respectively 0.281 and 0.048. Table 6 shows the values of the parameters used in the one-dimensional Navier-Stokes equations.

Figure 21 shows the Bode plot for transfer function $H_{NS\nu0}(s)$ and $H_{NS\nu0WK}(s)$, both showing large peaks for magnitude for frequencies above 4 Hz. For $H_{NS\nu0}(s)$ these peaks retain their large amplitude for increasing frequencies, while for $H_{NS\nu0WK}(s)$, where a Windkessel model is coupled, the amplitude decreases for higher frequencies. At these peaks, the phase shows jumps, which can be seen in the phase plot of Figure 21b.

Figure 22 shows the Bode plots for $H_{NSq0}(s)$ and $H_{NSq0WK}(s)$. These transfer functions do not show peaks in the magnitude, but both show a gradually decrease in magnitude for increasing frequencies. In the phase plot in Figure 22a one jump occurs.

Table 6: Parameter values for the one-dimensional Navier-Stokes equations.

Parameter	Value	Unit
r_0	0.38	cm
A_0	0.451	cm^2
A_{eq} [1]	1.732	cm^2
A_{eq} [2]	0.451	cm^2
q_{eq} [1]	33	mL/s
q_{eq} [2]	0	mL/s
b	52.8	cm
h	0.088	cm
ν	$4.64 \cdot 10^{-4}$ [61]	cm^2/s
δ	0.1 [58]	mmHg$\cdot$s^2/mL
E	$4 \cdot 10^6$ [59]	g/cm$\cdot$s^2
ρ	1.05 [61]	g/mL
C_b	$1.877 \cdot 10^{-6}$	cm$^4\cdot$s^2/g
R_b	$1.8304 \cdot 10^4$	g/cm^{4}s

[1]: for $\nu = 0$, [2]: for $q = 0$.

5.3.3 Comparison of zero- and one-dimensional models

To study the added value of a one-dimensional model to a two-element Windkessel model to describe the relation between LV flow and arterial blood pressure, Figure 23 shows the Bode plot of $H_{WK}(s)$, $H_{NS\nu0WK}(s)$ and $H_{NSq0WK}(s)$ together. The effects on the magnitude appear to be similar for $H_{UT}(s)$ and $H_{NSq0WK}(s)$, not only around the corrected frequency of 1.67 Hz. Whereas for the effects in phase $H_{UT}(s)$ and $H_{NS\nu0WK}(s)$ appear to behave similarly for frequencies below 5 Hz.
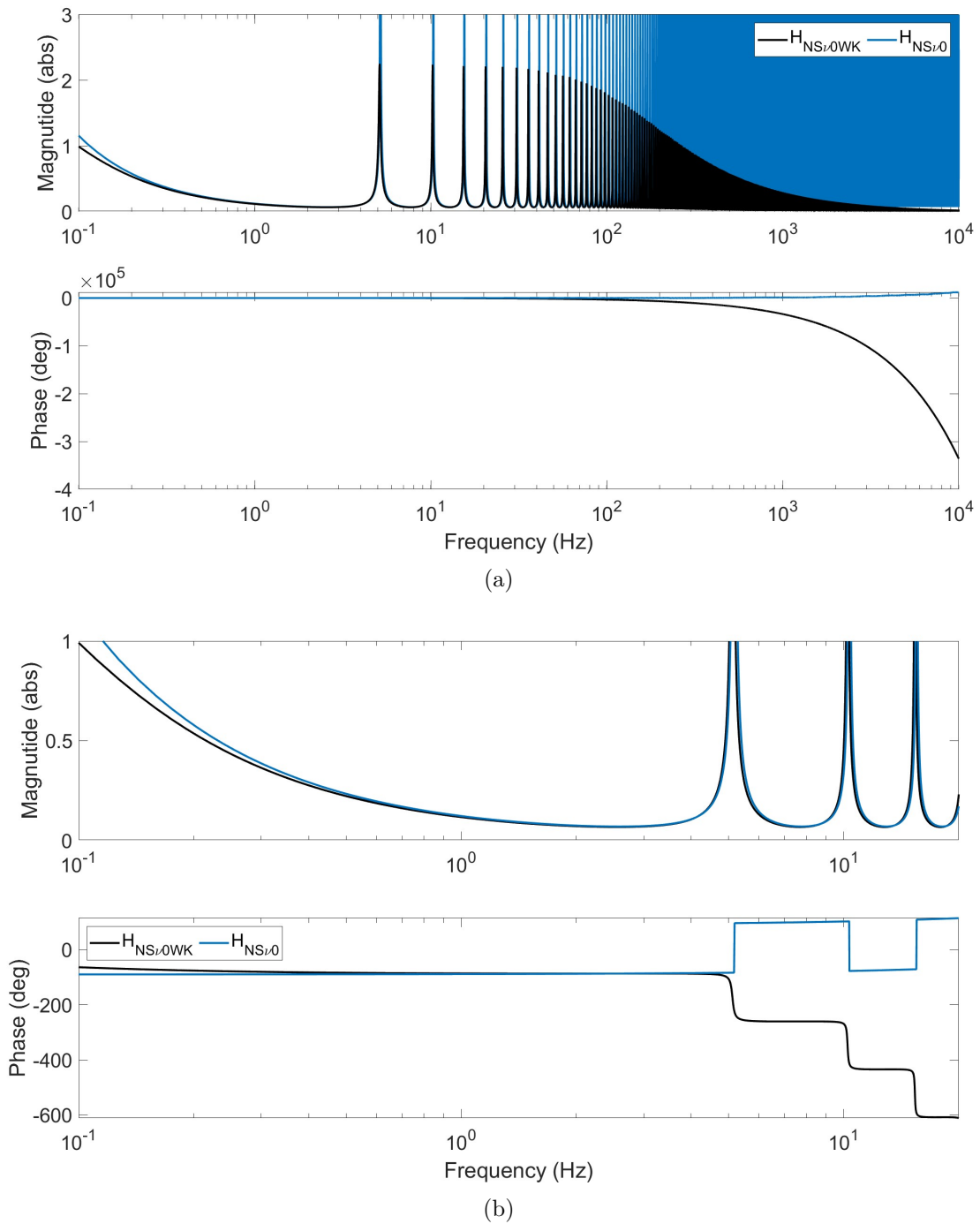
Figure 21: Bode plots of $H_{NS\nu0}(s)$ in blue and of $H_{NS\nu0WK}(s)$ in black line, over a) a wide frequency range and b) focused between 0.1 and 20 Hz.

46
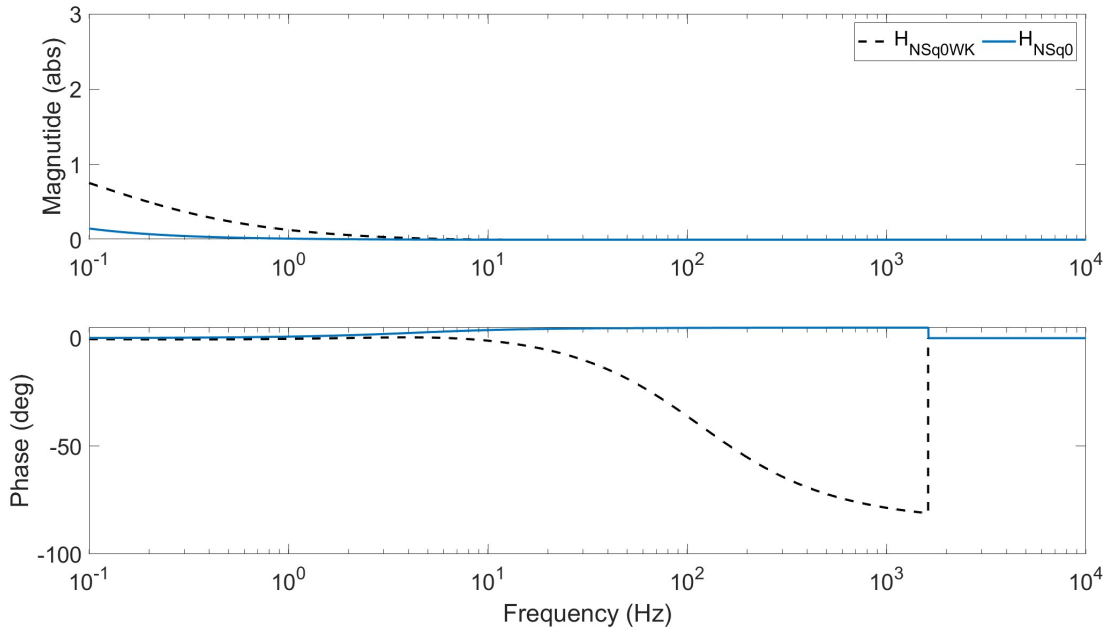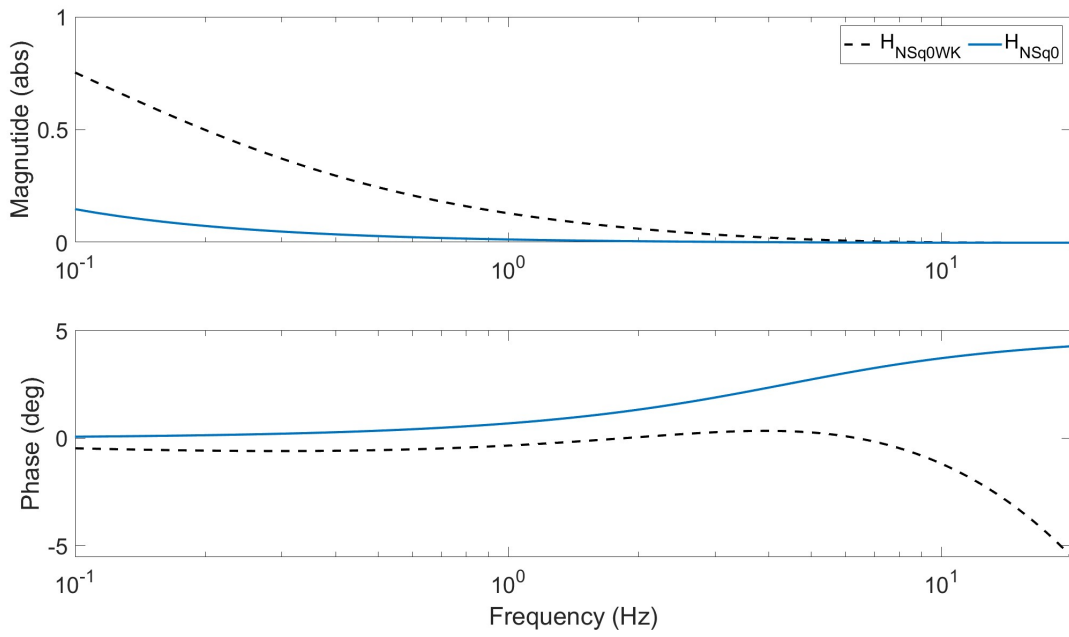
Figure 22: Bode plots of $H_{NSq0}(s)$ in solid blue line and of $H_{NSq0WK}(s)$ in black dashed line, over a) a wide frequency range and b) focused between 0.1 and 20 Hz.
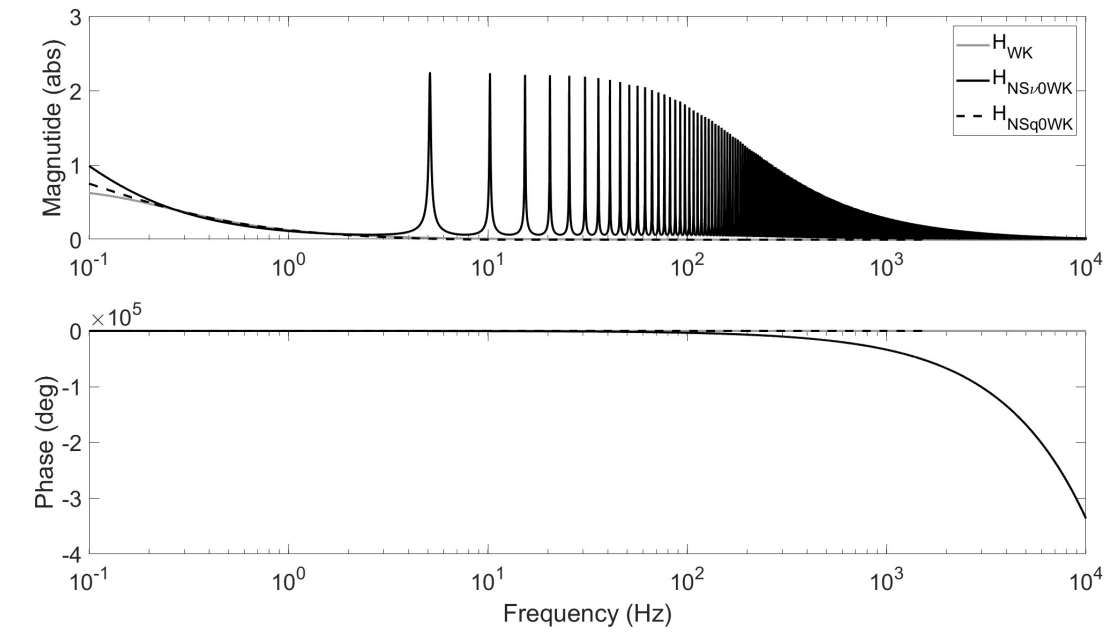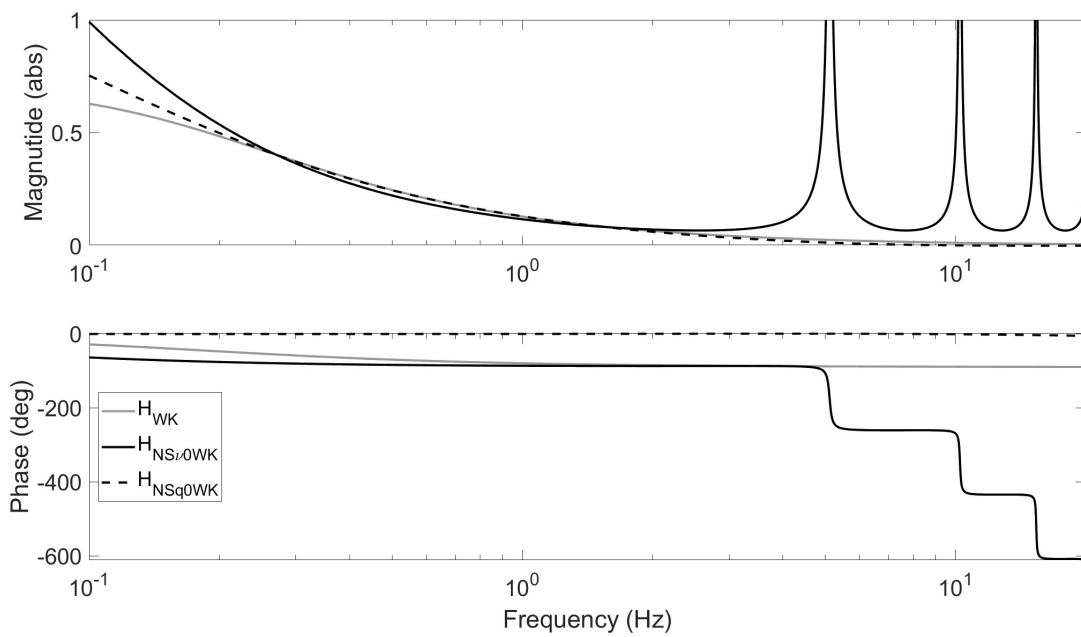
Figure 23: Bode plots of $H_{WK}(s)$ in solid grey line, $H_{NS\nu0WK}(s)$ in solid black line and of $H_{NSq0WK}(s)$ in dashed black line, over a) a wide frequency range and b) focused between 0.1 and 20 Hz.

5.4 Discussion

In this study we used transfer functions to study the added value of a one-dimensional distributed parameter model to describe the relation between blood pressure and flow. We compared the two-element Windkessel model and a more elaborate lumped parameter model to a one-dimensional model of a single compliant vessel. The one-dimensional Navier-Stokes equations were linearized around a steady state with different assumptions to obtain different transfer functions.

5.4.1 Lumped parameter models

Figure 19 and 20 show that for the two-element Windkessel model the magnitude is almost zero above 10 Hz. This is in line with the statement that the two-element Windkessel model is not accurate for high frequencies. The Bode plots shown for the two-element Windkessel model in this study are similar to the Bode plots shown by Westerhof et al., for both the magnitude and phase [38].

The more elaborate model shown in Figure 17, that is part of the model of the cardiovascular simulator of the University of Twente, shows results comparable to the two-element Windkessel model for frequencies between 0 and 2 Hz. However, for higher frequencies the phase shifts, similar to results of Westerhof et al. for the three- and four-element models [38]. The magnitude strongly increases for frequencies above 5 Hz, eventually towards infinity. This is induced by the improper transfer function. In the UT model, pressures are eventually used to calculate flow. Hence, pressure can be thought of as input and flow as output for the part of the model of the UT simulator Figure 17 shows. To compare the different models and transfer functions, flow is used as input and pressure as output, resulting in an improper transfer function for the UT model. Additionally, it is important to notice that for this comparison not the entire model is used, we did not include the valve models and the venous part of the model. Besides, we assumed an equal pressure after the peripheral resistances (R_{kid}, R_{spl}, R_{ll}, R_{rl}, R_{ub}), while in the actual model this equality only applies at the right atrium. The comparison with the UT model can be improved by using the entire model for simulations with different input frequencies and use the magnification and phase shift of the output to construct a Bode plot.

To show the effect of incorrect estimation of the vascular resistance, the transfer function for the two-element Windkessel model is also shown for varying resistances between -50 and +50%. Figure 19 shows that a modification of 50% in the vascular resistance also results in a modification of 50% in the magnitude of the transfer function for 0 Hz. This can also be concluded from Equation (10) for $s = 0$. Accordingly, an incorrect estimation of the vascular resistance can lead to large miscalculations of pressure, especially for constant flow. Since we study the application of the two-element Windkessel model during VA ECMO, a large part of the arterial blood pressure is caused by a constant flow. This is also shown when applying the model in Section 4. This confirms the importance of correct resistance estimation for the application of the two-element Windkessel model.

The effect of incorrect arterial compliance estimation is also shown. Figure 20 shows there is no effect of the accuracy of compliance estimation for a constant flow, as can also be concluded from $H_{WK}(s)$ itself. The compliance is of greater importance between 0.1 and 10 Hz, in particular for the magnitude, where varying the compliance with -50 and +50% leads to respectively over- and underestimation of the magnification. However, this effect is less prominent than the effect for changes in the resistance. Therefore, it remains important that especially vascular resistance is estimated with a high accuracy for a correct LV flow calculation.

5.4.2 One-dimensional Navier-Stokes equations

In this study we used the one-dimensional Navier-Stokes equations to describe a single vessel. For all corrected transfer functions based on these equations, the magnitude for low frequencies is similar to the measured values shown by Westerhof et al. However, these results do not match for the higher frequencies and for the phase. Actually, the comparison between these graphs is not entirely legitimate, since Westerhof et al. show a Bode plot with both pressure and flow measured in the aorta, whereas the transfer function we showed for the one-dimensional model describes blood pressure in the radial artery and flow in the aortic root [38].

For the linearization to derive the transfer functions $H_{NS\nu 0}(s)$ and $H_{NS\nu 0WK}(s)$, we assumed a viscosity of the blood of zero. This viscosity causes damping in the system, which can be noticed when comparing Figure 21 and 22. The large peaks in Figure 21, where an inviscid fluid is assumed, do not appear in Figure 22 where the viscosity of blood is taken into account. Figure 21 also shows the effect of the addition of the two-element Windkessel model in the boundary condition. The damping effect of the two-element Windkessel model causes the peaks in the magnitude to decrease for increasing frequencies.

For the linearization to derive transfer functions $H_{NSq0}(s)$ and $H_{NSq0WK}(s)$, we assumed the flow to be zero in steady-state. Although this situation does not occur during VA ECMO, we expected this linearization to be more realistic than using the assumption of an inviscid fluid, since blood is undoubtedly a viscous fluid.

5.4.3 Comparison of zero- and one-dimensional models

Figure 23 shows the Bode plot for the two-element Windkessel model together with the Bode plots for the one-dimensional models, coupled to a two-element Windkessel model. Note that in this study all transfer functions describe the relation between change in flow from the steady state to change in pressure from the steady state, instead of the pressure and flow itself. The magnitude of $H_{WK}(s)$ seems to match with the magnitude of $H_{NS\nu 0WK}(s)$ and $H_{NSq0WK}(s)$ for frequencies above 0.3 Hz, except for the peaks in $H_{NS\nu 0WK}(s)$. Part of this agreement is caused by the correction factor that aligns $H_{NS\nu 0WK}(s)$ and $H_{NSq0WK}(s)$ with $H_{WK}(s)$ at 1.67 Hz. The magnitude of $H_{NSq0WK}(s)$ decays towards zero just as fast as the Windkessel model. We did not expect to see this, since the two-element Windkessel model does not account correctly for the higher frequencies and we expected an improved performance for the one-dimensional model. It is unlikely that the small magnitude for high frequency is caused by the coupling with the Windkessel model, since $H_{NSq0}(s)$ shows the same behaviour. It is possible that this behaviour for large frequencies is due to the simplifications made to derive the transfer function of an already simplified model. The frequencies between 0.3 and 5 Hz for which the models show similar magnification, correspond with HR between 18 and 300 BPM. Physiological heart rates lie within this range.

The phase of $H_{WK}(s)$, $H_{NS\nu 0WK}(s)$ and $H_{NSq0WK}(s)$ are not similar, as shown in Figure 23. Below 5 Hz, $H_{NS\nu 0WK}(s)$ is similar to the two-element Windkessel model. The phase for $H_{NSq0WK}(s)$ remains around zero, which only matches for higher frequencies to the measured results of Westerhof et al., which also fluctuates around zero for frequencies above 4 Hz [38].

5.4.4 Strengths and limitations

We derived and used transfer functions to study if the use of a one-dimensional model would be of added value for LV flow calculations from radial artery pressure. The one-dimensional model we used represents a single vessel, without tapering or branching. In reality, branching of the vessels introduces wave reflection and is therefore likely to influence the LV flow calculations [59]. Analytic derivation of transfer functions of more elaborate one-dimensional models is however complex. To be able to compare the the LV flow calculation of the two-element Windkessel model to a situation with tapering and branching, it is recommended to construct a Bode plot of such a one-dimensional model. Instead of analytic derivation of the transfer function, a Bode plot estimation can be performed by using input signals with different frequencies and determine the amplification and phase shift for every frequency, as explained above for the UT model. Comparison with a one-dimensional model that includes tapering and branching may give more insight in the improvement that can be made in LV flow calculations.

To derive the transfer functions of the one-dimensional model, the one-dimensional Navier-Stokes equations were linearized. However, in this study we did not compare the solutions for the original model to the solutions of the linearizations. To study the validity of these linearizations, their solutions should be compared to the solutions of the non-linearized model in the physiological range around the steady state solutions. Besides, in the current model we assume LV flow and ECMO flow to both enter in the aortic arch as one source. In practice, femoral cannulation is most often used. While in the lumped parameter models, location and direction of flow into the arterial system are not taken into account, this is taken into account in a one dimensional model and can therefore influence the description of the relation between flow and pressure.

In this study we used parameter values estimated from literature. Besides, we used an extra correction factor to be able to compare the lumped parameter model to the one-dimensional models. The one-dimensional model requires a lot more parameters to be defined than the two-element Windkessel model. In the clinical setting, determining the two patient specific parameters for the two-element Windkessel model is already difficult. Since for the one-dimensional model even more patient-specific parameters are necessary, it is expected that application of this model for LV flow calculations in clinical practice will be challenging.

5.4.5 Conclusion

Comparison of transfer functions derived from linearized one-dimensional Navier-Stokes equations and lumped parameter models, showed that for low frequencies there is little difference between the models. Therefore, the use of these linearized distributed parameter models will not lead to large improvements in the flow calculations from arterial blood pressure for low frequencies. However, further studies should show if more comprehensive one-dimensional models can improve the LV flow waveform calculated from blood pressure in the radial artery.

6   General discussion

In this master thesis a method is studied to determine left ventricular flow from blood pressure measurements in patients supported with VA ECMO in the ICU. We showed that application of the two-element Windkessel model could be used to accurately determine SV during VA ECMO in different hemodynamic situation, in cardiovascular simulation and clinical data, using exactly known patient specific parameters. The waveform of the calculated LV flow from the clinical data did however not agree with the expected waveform. We also showed that linearized one-dimensional Navier-Stokes equations, describing the flow in a single vessel, will not lead to a large improvement in the flow calculations for low frequencies.

6.1   Recommendations

Chapter 4 and 5 show that the correct estimation of the patient specific parameters and especially total vascular resistance, is extremely important for a correct SV estimation with the two-element Windkessel model. To continuously determine the flow from the LV, also R and C need to be determined continuously. We can assume a constant compliance over time and use the proposed adapted time-decay method to continuously determine R as explained in Section 4.2.3.1. However, as shown in Chapter 4, current estimations of R are not accurate enough for continuous SV calculations. Therefore, the estimation of these patient specific parameter needs to be improved. Besides the method proposed in this thesis, there are also other methods available to determine R and C that could be adapted and validated for patients supported with VA ECMO, among which a method proposed by Arai et al. [53].

In addition to being used for the application of the two-element Windkessel model, the patient specific parameters can also be used for better patient characterization. The resistance and compliance influence MAP and PP. Therefore, to interpret the values for MAP and PP and choose the appropriate intervention based on this, knowledge of the arterial compliance and total vascular resistance of the individual patient is important.

Ideally, we would be able to monitor the ESPVR using its slope, which is comparable to Ees, to gain insight in the recovery or deterioration of the LV during VA ECMO. This could be done by using the LV flow waveform, instead of the stroke volume. From this flow, LVOTacc can be determined, which is shown to related to Ees [37]. Models that are more elaborate than the two-element Windkessel model, might improve calculation of the LV flow waveform. A downside of the application of more elaborate models is that the increased complexity of the model also increases the number of patient specific parameters that need to be determined. Another promising method to estimate LV contractility is the use of a physiological model, such as the models used in Chapter 3. These models can be fitted to a patient, using the available continuously measured data such as ECMO flow, arterial and venous blood pressure and HR, together with estimations of the resistance and compliance of the different compartments to determine the most probable value for Ees. Repetition of this fitting within several hours to days for changing parameters, results in consecutive values for Ees. This would be of great value to monitor the LV during VA ECMO, since Ees describes the LV function independently of pre- and afterload.

6.2   Future perspectives

This thesis mainly focuses on monitoring of the LV function, to gain more insight in the status of the patient. Continuous monitoring of the LV can also help to describe the ideal constellation for the

patient, in terms of ECMO settings, LV unloading and drugs and fluid administration. With this, the balanced situation that is aimed for in every patient can be defined. However, after defining the ideal situation it remains difficult to achieve this situation in the dynamic patient. With a continuous LV monitoring system we can strive for a decision support system to support the physician in the decision on the best interventions, resulting in the best possible treatment. Eventually one could think of an automated control system, in which the ECMO settings are (semi) automatically adapted based on patient data.

Continuously monitoring the function of the left ventricle can contribute to the improvement of the clinical management of patients supported with VA ECMO. Therefore, this can lead to improved treatment with VA ECMO, eventually leading to an increased survival of patients with cardiogenic shock in the future.

References

[1] H. Thiele, E. M. Ohman, S. de Waha-Thiele, U. Zeymer, and S. Desch, "Management of cardiogenic shock complicating myocardial infarction: An update 2019," *European Heart Journal*, vol. 40, no. 32, pp. 2671–2683, Aug. 2019, ISSN: 0195-668X. DOI: 10.1093/eurheartj/ehz363.

[2] H. R. Reynolds and J. S. Hochman, "Cardiogenic shock," *Circulation*, vol. 117, no. 5, pp. 686–697, Feb. 2008, ISSN: 0009-7322. DOI: 10.1161/CIRCULATIONAHA.106.613596.

[3] L. Rupprecht, B. Flörchinger, S. Schopka, *et al.*, "Cardiac decompression on extracorporeal life support: A review and discussion of the literature," *ASAIO Journal*, vol. 59, no. 6, pp. 547–553, Nov./Dec. 2013, ISSN: 10582916. DOI: 10.1097/MAT.0b013e3182a4b2f6.

[4] M. M. Koerner, M. D. Harper, C. K. Gordon, *et al.*, "Adult cardiac veno-arterial extracorporeal life support (VA-ECMO): Prevention and management of acute complications," *Annals of Cardiothoracic Surgery*, vol. 8, no. 1, pp. 66–75, Jan. 2019, ISSN: 23041021. DOI: 10.21037/acs.2018.12.09.

[5] J. A. Hermens, C. L. Meuwese, M. K. Szymanski, M. Gianoli, D. van Dijk, and D. W. Donker, "Patient-centered weaning from venoarterial extracorporeal membrane oxygenation: "A practice-oriented narrative review of literature"," *Perfusion (United Kingdom)*, vol. 38, no. 7, pp. 1349–1359, Oct. 2023, ISSN: 1477111X. DOI: 10.1177/02676591221115938.

[6] M. Mourad, J. Eliet, N. Zeroual, *et al.*, "Pulse pressure and end-tidal carbon dioxide for monitoring low native cardiac output during veno-arterial ECLS: A prospective observational study," *Critical Care*, vol. 24, no. 1, pp. 1–9, Sep. 2020, ISSN: 1466609X. DOI: 10.1186/s13054-020-03280-z.

[7] C. L. Meuwese, D. Brodie, and D. W. Donker, "The ABCDE approach to difficult weaning from venoarterial extracorporeal membrane oxygenation," *Critical Care*, vol. 26, no. 1, pp. 1–11, Jul. 2022, ISSN: 1466609X. DOI: 10.1186/s13054-022-04089-8.

[8] C. L. Meuwese, J. A. Hermens, M. de Haan, *et al.*, "Twelve years of circulatory extracorporeal life support at the University Medical Centre Utrecht," *Netherlands Heart Journal*, vol. 29, no. 7-8, pp. 394–401, Mar. 2021, ISSN: 18766250. DOI: 10.1007/s12471-021-01552-z.

[9] ELSO, "ECLS Registry Report International Summary - October 2022," Extracorporeal Life Support Organization, Tech. Rep., 2022, p. 1.

[10] D. W. Donker, M. Sallisalmi, and M. Broomé, "Right-Left Ventricular Interaction in Left-Sided Heart Failure With and Without Venoarterial Extracorporeal Membrane Oxygenation Support-A Simulation Study," *ASAIO Journal*, vol. 67, no. 3, pp. 297–305, Mar. 2021, ISSN: 1538943X. DOI: 10.1097/MAT.0000000000001242.

[11] K. R. Walley, "Function of the Left Heart," in *Cardiopulmonary Monitoring*, S. Magder, A. Malhotra, K. A. Hibbert, and C. C. Hardin, Eds. Cham: Springer International Publishing, 2021, ch. 4, pp. 49–60. DOI: 10.1007/978-3-030-73387-2_4.

[12] A. Nitenberg, "Evaluation of left ventricular performance: an insolvable problem in human beings? The Graal quest," in *Applied Physiology in Intensive Care Medicine 2*, M. R. Pinsky, L. Brochard, J. Mancebo, and M. Antonelli, Eds., 3rd ed. Heidelberg, New York, Dordrecht, London: Springer, 2012, pp. 363–365. DOI: 10.1007/978-3-642-28233-1_42.

[13] P. Morimont, B. Lambermont, J. Guiot, *et al.*, "Ejection Fraction May Not Reflect Contractility: Example in Veno-Arterial Extracorporeal Membrane Oxygenation for Heart Failure," *ASAIO Journal*, vol. 64, no. 4, E68–E71, Jul./Aug. 2018, ISSN: 1538943X. DOI: 10.1097/MAT.0000000000000661.

[14] H. S. Lim, "The Physiologic Basis of Ejection Fraction [Letter to the editor]," *ASAIO Journal*, vol. 65, no. 6, E63, Aug. 2019, ISSN: 1538943X. DOI: 10.1097/MAT.0000000000000899.

[15] P. Morimont and B. Lambermont, "Measuring Contractility During Mechanical Circulatory Support Would Be a Strong Plus [Letter to the editor]," *ASAIO Journal*, vol. 64, no. 5, E139, Sep./Oct. 2018, ISSN: 1538943X. DOI: 10.1097/MAT.0000000000000738.

[16] A. M. Dart and B. A. Kingwell, "Pulse pressure - A review of mechanisms and clinical relevance," *Journal of the American College of Cardiology*, vol. 37, no. 4, pp. 975–984, Mar. 2001, ISSN: 07351097. DOI: 10.1016/S0735-1097(01)01108-1.

[17] J. Rilinger, A. M. Riefler, X. Bemtgen, *et al.*, "Impact of pulse pressure on clinical outcome in extracorporeal cardiopulmonary resuscitation (eCPR) patients," *Clinical Research in Cardiology*, vol. 110, no. 9, pp. 1473–1483, Sep. 2021, ISSN: 18610692. DOI: `10.1007/s00392-021-01838-7`.

[18] S. I. Lee, Y. S. Lim, C. H. Park, W. S. Choi, and C. H. Choi, "Importance of pulse pressure after extracorporeal cardiopulmonary resuscitation," *Journal of Cardiac Surgery*, vol. 36, no. 8, pp. 2743–2750, Aug. 2021, ISSN: 15408191. DOI: `10.1111/jocs.15614`.

[19] M. Siriwardena, J. Breeding, M. Gopalakrishnan, *et al.*, "Pulse pressure within the first 2 days of venoarterial extracorporeal membrane oxygenation is predictive of death prior to hospital discharge, renal dysfunction requiring dialysis and pulmonary oedema," *Perfusion (United Kingdom)*, vol. 38, no. 8, pp. 1568–1576, 2023, ISSN: 1477111X. DOI: `10.1177/02676591221115935`.

[20] B. W. Park, D. C. Seo, I. K. Moon, *et al.*, "Pulse pressure as a prognostic marker in patients receiving extracorporeal life support," *Resuscitation*, vol. 84, no. 10, pp. 1404–1408, Oct. 2013, ISSN: 03009572. DOI: `10.1016/j.resuscitation.2013.04.009`.

[21] Z. Liu, C. T. Ting, S. Zhu, and F. C. Yin, "Aortic compliance in human hypertension," *Hypertension*, vol. 14, no. 2, pp. 129–136, Aug. 1989, ISSN: 0194911X. DOI: `10.1161/01.HYP.14.2.129`.

[22] G. E. McVeigh, C. W. Bratteli, D. J. Morgan, *et al.*, "Age-related abnormalities in arterial compliance identified by pressure pulse contour analysis: Aging and arterial compliance," *Hypertension*, vol. 33, no. 6, pp. 1392–1398, Jun. 1999, ISSN: 0194911X. DOI: `10.1161/01.HYP.33.6.1392`.

[23] T. Länne, B. Sonesson, D. Bergqvist, H. Bengtsson, and D. Gustafsson, "Diameter and compliance in the male human abdominal aorta: Influence of age and aortic aneurysm," *European Journal of Vascular Surgery*, vol. 6, no. 2, pp. 178–184, Mar. 1992, ISSN: 0950821X. DOI: `10.1016/S0950-821X(05)80237-3`.

[24] P. Tozzi, D. Hayoz, C. Oedman, I. Mallabiabarrena, and L. K. Von Segesser, "Systolic axial artery length reduction: An overlooked phenomenon in vivo," *American Journal of Physiology - Heart and Circulatory Physiology*, vol. 280, no. 5 49-5, pp. 2300–2305, May 2001, ISSN: 03636135. DOI: `10.1152/ajpheart.2001.280.5.h2300`.

[25] D. Švec and M. Javorka, "Noninvasive Arterial Compliance Estimation," *Physiological Research*, vol. 70, pp. 483–494, Dec. 2021, ISSN: 18029973. DOI: `10.33549/physiolres.934798`.

[26] D. Chemla, J.-L. Hébert, C. Coirault, *et al.*, "Total arterial compliance estimated by stroke volume-to-aortic pulse pressure ratio in humans," *American Journal of Physiology-Heart and Circulatory Physiology*, vol. 274, no. 2, H500–H505, Feb. 1998, ISSN: 0363-6135. DOI: `10.1152/ajpheart.1998.274.2.H500`.

[27] N. Stergiopulos, J. J. Meister, and N. Westerhof, "Evaluation of methods for estimation of total arterial compliance," *American Journal of Physiology - Heart and Circulatory Physiology*, vol. 268, no. 4, H1540–H1548, Apr. 1995, ISSN: 03636135. DOI: `10.1152/ajpheart.1995.268.4.h1540`.

[28] R. Naeije, "Pulmonary vascular resistance: A meaningless variable?" *Intensive Care Medicine*, vol. 29, no. 4, pp. 526–529, Feb. 2003, ISSN: 03424642. DOI: `10.1007/s00134-003-1693-3`.

[29] L. B. K. Hill, J. J. Sollers, and J. F. Thayer, "Resistance reconstructed: Estimation of total peripheral resistance from computationally-derived cardiac output," *Biomedical Sciences Instrumentation*, vol. 49, pp. 216–223, 2013, ISSN: 00678856.

[30] J. L. Teboul, B. Saugel, M. Cecconi, *et al.*, "Less invasive hemodynamic monitoring in critically ill patients," *Intensive Care Medicine*, vol. 42, no. 9, pp. 1350–1359, Sep. 2016, ISSN: 14321238. DOI: `10.1007/s00134-016-4375-7`.

[31] S. Krishnan and G. A. Schmidt, "Hemodynamic monitoring in the extracorporeal membrane oxygenation patient," *Current Opinion in Critical Care*, vol. 25, no. 3, pp. 285–291, Jun. 2019, ISSN: 1070-5295. DOI: `10.1097/MCC.0000000000000602`.

[32] N. Fazeli and J. O. Hahn, "Estimation of cardiac output and peripheral resistance using square-wave-approximated aortic flow signal," *Frontiers in Physiology*, vol. 3, pp. 1–10, Jul. 2012, ISSN: 1664042X. DOI: `10.3389/fphys.2012.00298`.

[33] T. Arai, K. Lee, and R. J. Cohen, "Cardiac output and stroke volume estimation using a hybrid of three Windkessel models," *Annual International Conference of the IEEE Engineering in Medicine and Biology Society*, pp. 4971–4974, 2010. DOI: `10.1109/IEMBS.2010.5627225`.

[34] T. A. Parlikar, T. Heldt, G. V. Ranade, and G. C. Verghese, "Model-based estimation of cardiac output and total peripheral resistance," *Computers in Cardiology*, vol. 34, pp. 379–382, Sep. 2007, ISSN: 02766574. DOI: 10.1109/CIC.2007.4745501.

[35] K. Kouz, T. W. Scheeren, D. De Backer, and B. Saugel, "Pulse Wave Analysis to Estimate Cardiac Output," *Anesthesiology*, vol. 134, no. 1, pp. 119–126, Jan. 2021, ISSN: 15281175. DOI: 10.1097/ALN.0000000000003553.

[36] B. Saugel, K. Kouz, T. W. Scheeren, *et al.*, "Cardiac output estimation using pulse wave analysis—physiology, algorithms, and technologies: a narrative review," *British Journal of Anaesthesia*, vol. 126, no. 1, pp. 67–76, Jan. 2021, ISSN: 14716771. DOI: 10.1016/j.bja.2020.09.049.

[37] F. Bauer, M. Jones, T. Shiota, *et al.*, "Left ventricular outflow tract mean systolic acceleration as a surrogate for the slope of the left ventricular end-systolic pressure-volume relationship," *Journal of the American College of Cardiology*, vol. 40, no. 7, pp. 1320–1327, Oct. 2002, ISSN: 07351097. DOI: 10.1016/S0735-1097(02)02138-1.

[38] N. Westerhof, J. W. Lankhaar, and B. E. Westerhof, "The arterial windkessel," *Medical and Biological Engineering and Computing*, vol. 47, no. 2, pp. 131–141, Feb. 2009, ISSN: 01400118. DOI: 10.1007/s11517-008-0359-2.

[39] P. Segers, E. R. Rietzschel, M. L. De Buyzere, *et al.*, "Three-and-four-element Windkessel models: Assessment of their fitting performance in a large cohort of healthy middle-aged individuals," *Proceedings of the Institution of Mechanical Engineers, Part H: Journal of Engineering in Medicine*, vol. 222, no. 4, pp. 417–428, Apr. 2008, ISSN: 09544119. DOI: 10.1243/09544119JEIM287.

[40] L. Fresiello, G. Ferrari, A. Di Molfetta, *et al.*, "A cardiovascular simulator tailored for training and clinical uses," *Journal of Biomedical Informatics*, vol. 57, pp. 100–112, Oct. 2015, ISSN: 15320464. DOI: 10.1016/j.jbi.2015.07.004.

[41] M. Broomé, E. Maksuti, A. Bjällmark, B. Frenckner, and B. Janerot-Sjöberg, "Closed-loop real-time simulation model of hemodynamics and oxygen transport in the cardiovascular system," *BioMedical Engineering Online*, vol. 12, no. 1, pp. 1–20, Jul. 2013, ISSN: 1475925X. DOI: 10.1186/1475-925X-12-69.

[42] D. Burkhoff, G. Sayer, D. Doshi, and N. Uriel, "Hemodynamics of Mechanical Circulatory Support," *Journal of the American College of Cardiology*, vol. 66, no. 23, pp. 2663–2674, Dec. 2015, ISSN: 15583597. DOI: 10.1016/j.jacc.2015.10.017.

[43] H. Baumgartner, J. Hung, J. Bermejo, *et al.*, "Recommendations on the echocardiographic assessment of aortic valve stenosis: A focused update from the European Association of Cardiovascular Imaging and the American Society of Echocardiography," *European Heart Journal Cardiovascular Imaging*, vol. 18, no. 3, pp. 254–275, Mar. 2017, ISSN: 20472412. DOI: 10.1093/ehjci/jew335.

[44] W. A. Zoghbi, D. Adams, R. O. Bonow, *et al.*, "Recommendations for Noninvasive Evaluation of Native Valvular Regurgitation: A Report from the American Society of Echocardiography Developed in Collaboration with the Society for Cardiovascular Magnetic Resonance," *Journal of the American Society of Echocardiography*, vol. 30, no. 4, pp. 303–371, Apr. 2017, ISSN: 10976795. DOI: 10.1016/j.echo.2017.01.007.

[45] J. Alastruey, P. H. Charlton, V. Bikia, *et al.*, "Arterial pulse wave modeling and analysis for vascular-age studies: A review from vascagenet," *American Journal of Physiology-Heart and Circulatory Physiology*, vol. 325, no. 1, H1–H29, Jul. 2023, ISSN: 0363-6135. DOI: 10.1152/ajpheart.00705.2022.

[46] O. Bond, S. Pozzebon, F. Franchi, *et al.*, "Comparison of estimation of cardiac output using an uncalibrated pulse contour method and echocardiography during veno-venous extracorporeal membrane oxygenation," *Perfusion*, vol. 35, no. 5, pp. 397–401, Jul. 2020, ISSN: 0267-6591. DOI: 10.1177/0267659119883204.

[47] W. F. Boron and E. L. Boulpaep, *Medical Physiology: a cellular and molecular approach*, 2nd. Philadelphia: Elsevier, 2012, pp. 534–535, ISBN: 9781437717532.

[48] D. A. Reuter, C. Huang, T. Edrich, S. K. Shernan, and H. K. Eltzschig, "Cardiac output monitoring using indicator-dilution techniques: Basics, limits, and perspectives," *Anesthesia and Analgesia*, vol. 110, no. 3, pp. 799–811, Mar. 2010, ISSN: 00032999. DOI: 10.1213/ANE.0b013e3181cc885a.

[49] K. F. Bachmann, L. Zwicker, K. Nettelbeck, *et al.*, "Assessment of right heart function during extracorporeal therapy by modified thermodilution in a porcine model," *Anesthesiology*, vol. 133, no. 4, pp. 879–891, Oct. 2020, ISSN: 15281175. DOI: 10.1097/ALN.0000000000003443.

[50] P. Blanco, "Rationale for using the velocity–time integral and the minute distance for assessing the stroke volume and cardiac output in point-of-care settings," *Ultrasound Journal*, vol. 12, no. 1, Dec. 2020, ISSN: 25248987. DOI: 10.1186/s13089-020-00170-x.

[51] J. M. Bland and D. G. Altman, "Statistical methods for assessing agreement between two methods of clinical measurement.," *Lancet (London, England)*, vol. 327, no. 8476, pp. 307–310, Feb. 1986, ISSN: 0140-6736. DOI: 10.1016/S0140-6736(86)90837-8.

[52] J. M. Bland and D. G. Altman, "Measuring agreement in method comparison studies.," *Statistical methods in medical research*, vol. 8, no. 2, pp. 135–60, Jun. 1999, ISSN: 0962-2802. DOI: 10.1177/096228029900800204.

[53] T. Arai, K. Lee, M. B. Stenger, S. H. Platts, J. V. Meck, and R. J. Cohen, "Preliminary application of a novel algorithm to monitor changes in pre-flight total peripheral resistance for prediction of post-flight orthostatic intolerance in astronauts," *Acta Astronautica*, vol. 68, no. 7-8, pp. 770–777, Apr. 2011, ISSN: 00945765. DOI: 10.1016/j.actaastro.2010.10.008.

[54] M. Jozwiak, P. Mercado, J. L. Teboul, *et al.*, "What is the lowest change in cardiac output that transthoracic echocardiography can detect?" *Critical Care*, vol. 23, no. 1, Apr. 2019, ISSN: 1466609X. DOI: 10.1186/s13054-019-2413-x.

[55] S. Sacchi, N. M. Dhutia, M. J. Shun-Shin, *et al.*, "Doppler assessment of aortic stenosis: A 25-operator study demonstrating why reading the peak velocity is superior to velocity time integral," *European Heart Journal Cardiovascular Imaging*, vol. 19, no. 12, pp. 1380–1389, Dec. 2018, ISSN: 20472412. DOI: 10.1093/ehjci/jex218.

[56] H. Huh, J. Lee, M. Kinno, M. Markl, J. D. Thomas, and A. J. Barker, "Two wrongs sometimes do make a right: errors in aortic valve stenosis assessment by same-day Doppler echocardiography and 4D flow MRI," *International Journal of Cardiovascular Imaging*, vol. 38, no. 8, pp. 1815–1823, Aug. 2022, ISSN: 15730743. DOI: 10.1007/s10554-022-02553-8.

[57] A. L. Barnard, W. Hunt, W. Timlake, and E. Varley, "A Theory of Fluid Flow in Compliant Tubes," *Biophysical Journal*, vol. 6, no. 6, pp. 717–724, Nov. 1966, ISSN: 00063495. DOI: 10.1016/S0006-3495(66)86690-0.

[58] M. S. Olufsen, C. S. Peskin, W. Y. Kim, E. M. Pedersen, A. Nadim, and J. Larsen, "Numerical Simulation and Experimental Validation of Blood Flow in Arteries with Structured-Tree Outflow Conditions," *Annals of Biomedical Engineering*, vol. 28, no. 11, pp. 1281–1299, Nov. 2000, ISSN: 0090-6964. DOI: 10.1114/1.1326031.

[59] N. Westerhof, F. Bosman, C. J. De Vries, and A. Noordergraaf, "Analog studies of the human systemic arterial tree," *Journal of Biomechanics*, vol. 2, no. 2, pp. 121–143, May 1969, ISSN: 00219290. DOI: 10.1016/0021-9290(69)90024-4.

[60] R. Curtain and K. Morris, "Transfer functions of distributed parameter systems: A tutorial," *Automatica*, vol. 45, no. 5, pp. 1101–1116, May 2009, ISSN: 00051098. DOI: 10.1016/j.automatica.2009.01.008.

[61] B. N. Steele, D. Valdez-Jasso, M. A. Haider, and M. S. Olufsen, "Predicting arterial flow and pressure dynamics using a 1D fluid dynamics model with a viscoelastic wall," *SIAM Journal on Applied Mathematics*, vol. 71, no. 4, pp. 1123–1143, Jan. 2011, ISSN: 00361399. DOI: 10.1137/100810186.

Appendices

A   Simulation parameters

Table 7: Parameters used for the simulations in the UT simulator. Besides the values for: total blood volume = 6140 mL, Cubv = 9.6, CkidV = 18, CspV = 66, CllV = 11.4, CrlV = 11.4, CsupVCint = 18, CinfVCint = 2.4, CinfVCext = 30, Cap = 1.5.

Baseline	HR	Es LV	Es RV	al	AV →	MV ←	Rpulm	Rkid	Rspl	Rll	Rrl	Rub	Ca1	Ca2	Q_E	RPM
1	100	1	1.01	0.15	20	100000	0.101	3.19	2.34	5.58	5.58	3	0.66	0.55	2	2500

R and C	HR	Es LV	Es RV	al	AV →	MV ←	Rpulm	Rkid	Rspl	Rll	Rrl	Rub	Ca1	Ca2	Q_E	RPM
1	100	1	1.01	0.15	20	100000	0.101	2.233	1.638	3.906	3.906	2.1	0.66	0.55	3	3000
2	100	1	1.01	0.15	20	100000	0.101	1.595	1.17	2.79	2.79	1.5	0.66	0.55	5.4	4000
3	100	1	1.01	0.15	20	100000	0.101	4.147	3.042	7.254	7.254	3.9	0.66	0.55	2	2500
4	100	1	1.01	0.15	20	100000	0.101	4.785	3.51	8.37	8.37	4.5	0.66	0.55	1.9	2500
5	100	1	1.01	0.15	20	100000	0.101	3.19	2.34	5.58	5.58	3	0.462	0.385	2	2500
6	100	1	1.01	0.15	20	100000	0.101	3.19	2.34	5.58	5.58	3	0.33	0.275	2.1	2500
7	100	1	1.01	0.15	20	100000	0.101	3.19	2.34	5.58	5.58	3	0.858	0.715	2	2500
8	100	1	1.01	0.15	20	100000	0.101	3.19	2.34	5.58	5.58	3	0.99	0.825	2	2500
9	100	1	1.01	0.15	20	100000	0.101	2.233	1.638	3.906	3.906	2.1	0.462	0.385	3	3000
10	100	1	1.01	0.15	20	100000	0.101	4.147	3.042	7.254	7.254	3.9	0.462	0.385	2	2500

HR	HR	Es LV	Es RV	al	AV →	MV ←	Rpulm	Rkid	Rspl	Rll	Rrl	Rub	Ca1	Ca2	Q_E	RPM
1	40	1	1.01	0.15	20	100000	0.101	3.19	2.34	5.58	5.58	3	0.66	0.55	3	3000
2	60	1	1.01	0.15	20	100000	0.101	3.19	2.34	5.58	5.58	3	0.66	0.55	2.1	2500
3	80	1	1.01	0.15	20	100000	0.101	3.19	2.34	5.58	5.58	3	0.66	0.55	2.1	2500
4	120	1	1.01	0.15	20	100000	0.101	3.19	2.34	5.58	5.58	3	0.66	0.55	2	2500
5	140	1	1.01	0.15	20	100000	0.101	3.19	2.34	5.58	5.58	3	0.66	0.55	2.1	2500

RV	HR	Es LV	Es RV	al	AV →	MV ←	Rpulm	Rkid	Rspl	Rll	Rrl	Rub	Ca1	Ca2	Q_E	RPM
1	100	1	0.9	0.15	20	100000	0.101	3.19	2.34	5.58	5.58	3	0.66	0.55	2	2500
2	100	1	0.7	0.15	20	100000	0.101	3.19	2.34	5.58	5.58	3	0.66	0.55	2	2500
3	100	1	0.4	0.15	20	100000	0.101	3.19	2.34	5.58	5.58	3	0.66	0.55	2.1	2500

AS	HR	Es LV	Es RV	al	AV →	MV ←	Rpulm	Rkid	Rspl	Rll	Rrl	Rub	Ca1	Ca2	Q_E	RPM
1	100	1	1.01	0.15	40	100000	0.101	3.19	2.34	5.58	5.58	3	0.66	0.55	2	2500
2	100	1	1.01	0.15	80	100000	0.101	3.19	2.34	5.58	5.58	3	0.66	0.55	2.1	2500
3	100	1	1.01	0.15	110	100000	0.101	3.19	2.34	5.58	5.58	3	0.66	0.55	3	3000

MR	HR	Es LV	Es RV	al	AV →	MV ←	Rpulm	Rkid	Rspl	Rll	Rrl	Rub	Ca1	Ca2	Q_E	RPM
1	100	1	1.01	0.15	20	500	0.101	3.19	2.34	5.58	5.58	3	0.66	0.55	2.1	2500
2	100	1	1.01	0.15	20	300	0.101	3.19	2.34	5.58	5.58	3	0.66	0.55	2.1	2500
3	100	1	1.01	0.15	20	140	0.101	3.19	2.34	5.58	5.58	3	0.66	0.55	3	3000

Table 8: Parameters used for the simulations in the Harvi simulator.

Baseline	HR	Es LV	Es RV	α LV	α RV	β LV	β RV	AV open area	MV close area	SVR	PVR	Ca sys	Ca pul	Q_E	RPM
1	100	0.7	0.74	0.034	0.028	0.22	0.34	-	0	12.7	1.9	1.2	25	2.1	2000

R and C	HR	Es LV	Es RV	α LV	α RV	β LV	β RV	AV open area	MV close area	SVR	PVR	Ca sys	Ca pul	Q_E	RPM
1	100	0.7	0.74	0.034	0.028	0.22	0.34	-	0	8.9	1.9	1.2	25	3.8	3600
2	100	0.7	0.74	0.034	0.028	0.22	0.34	-	0	6.4	1.9	1.2	25	5.8	6500
3	100	0.7	0.74	0.034	0.028	0.22	0.34	-	0	16.5	1.9	1.2	25	2.1	2040
4	100	0.7	0.74	0.034	0.028	0.22	0.34	-	0	19.1	1.9	1.2	25	2.1	2040
5	100	0.7	0.74	0.034	0.028	0.22	0.34	-	0	12.7	1.9	0.8	25	2.1	2040
6	100	0.7	0.74	0.034	0.028	0.22	0.34	-	0	12.7	1.9	0.6	25	2.1	2040
7	100	0.7	0.74	0.034	0.028	0.22	0.34	-	0	12.7	1.9	1.6	25	2.1	2040
8	100	0.7	0.74	0.034	0.028	0.22	0.34	-	0	12.7	1.9	1.8	25	2.1	2000
9	100	0.7	0.74	0.034	0.028	0.22	0.34	-	0	8.9	1.9	0.8	25	4.1	4000
10	100	0.7	0.74	0.034	0.028	0.22	0.34	-	0	16.5	1.9	0.8	25	2.1	2040

HR	HR	Es LV	Es RV	α LV	α RV	β LV	β RV	AV open area	MV close area	SVR	PVR	Ca sys	Ca pul	Q_E	RPM
1	40	0.7	0.67	0.034	0.028	0.22	0.34	-	0	12.7	1.9	1.2	25	3.9	3720
2	60	0.7	0.52	0.034	0.028	0.22	0.34	-	0	12.7	1.9	1.2	25	3	2820
3	80	0.7	0.30	0.034	0.028	0.22	0.34	-	0	12.7	1.9	1.2	25	2.2	2120
5	120	0.7	0.74	0.034	0.028	0.22	0.34	-	0	12.7	1.9	1.2	25	2.1	2000
6	140	0.7	0.74	0.034	0.028	0.22	0.34	-	0	12.7	1.9	1.2	25	2	2040

RV	HR	Es LV	Es RV	α LV	α RV	β LV	β RV	AV open area	MV close area	SVR	PVR	Ca sys	Ca pul	Q_E	RPM
1	100	0.7	0.74	0.034	0.028	0.22	0.34	-	0	12.7	1.9	1.2	25	2.1	2050
2	100	0.7	0.74	0.034	0.028	0.22	0.34	-	0	12.7	1.9	1.2	25	2.1	2050
3	100	0.7	0.74	0.034	2.000	0.22	0.34	-	0	12.7	1.9	1.2	25	2.1	2000

AS	HR	Es LV	Es RV	α LV	α RV	β LV	β RV	AV open area	MV close area	SVR	PVR	Ca sys	Ca pul	Q_E	RPM
1	100	0.7	0.74	0.034	0.028	0.22	0.34	2	0	12.7	1.9	1.2	25	2.1	1990
2	100	0.7	0.74	0.034	0.028	0.22	0.34	1.3	0	12.7	1.9	1.2	25	2.1	1990
3	100	0.7	0.74	0.034	0.028	0.22	0.34	0.8	0	12.7	1.9	1.2	25	2.5	2300

MR	HR	Es LV	Es RV	α LV	α RV	β LV	β RV	AV open area	MV close area	SVR	PVR	Ca sys	Ca pul	Q_E	RPM
1	100	0.7	0.74	0.034	0.028	0.22	0.34	-	0.1	12.7	1.9	1.2	25	2.1	2000
2	100	0.7	0.74	0.034	0.028	0.22	0.34	-	0.3	12.7	1.9	1.2	25	2.9	2700
3	100	0.7	0.74	0.034	0.028	0.22	0.34	-	0.5	12.7	1.9	1.2	25	3.5	3300

Table 9: Parameters used for the simulations in the Aplysia simulator. Besides the value for total blood volume = 5300 mL.

Baseline	HR	SVR	PVR	Contr. LV	Stiffness LV	Ca	Contr. RV	MV close area	AV open area	Q_E	RPM
1	100	0.76	0.115	0.8	0.054	1.23	0.6	0	5	2.1	2500

R and C	HR	SVR	PVR	Contr. LV	Stiffness LV	C	Contr. RV	MV close area	AV open area	Q_E	RPM
1	100	0.53	0.115	0.8	0.054	1.23	0.6	0	5	2.4	2800
2	100	0.38	0.115	0.8	0.054	1.23	0.6	0	5	5	4800
3	100	1	0.115	0.8	0.054	1.23	0.6	0	5	2	2500
4	100	1.14	0.115	0.8	0.054	1.23	0.6	0	5	2	2500
5	100	0.76	0.115	0.8	0.054	0.88	0.6	0	5	2.1	2500
6	100	0.76	0.115	0.8	0.054	0.62	0.6	0	5	2.1	2500
7	100	0.76	0.115	0.8	0.054	1.56	0.6	0	5	2.1	2500
8	100	0.76	0.115	0.8	0.054	1.92	0.6	0	5	2.1	2500
9	100	0.53	0.115	0.8	0.054	0.88	0.6	0	5	2.7	3000
10	100	1	0.115	0.8	0.054	0.85	0.6	0	5	2	2500

HR	HR	SVR	PVR	Contr. LV	LV stiffness	Ca	Contr. RV	MV close area	AV open area	Q_E	RPM
1	40	0.76	0.115	0.8	0.054	1.23	0.6	0	5	2.7	3000
2	60	0.76	0.115	0.8	0.054	1.23	0.6	0	5	2.1	2500
3	80	0.76	0.115	0.8	0.054	1.23	0.6	0	5	2.1	2500
4	120	0.76	0.115	0.8	0.054	1.23	0.6	0	5	2.1	2500
5	140	0.76	0.115	0.8	0.054	1.23	0.6	0	5	2.1	2500

RV	HR	SVR	PVR	Contr. LV	LV stiffness	Ca	Contr. RV	MV close area	AV open area	Q_E	RPM
1	100	0.76	0.115	0.8	0.054	1.23	0.5	0	5	2.1	2500
2	100	0.76	0.115	0.8	0.054	1.23	0.4	0	5	2.1	2500
3	100	0.76	0.115	0.8	0.054	1.23	0.2	0	5	2.1	2500

AS	HR	SVR	PVR	Contr. LV	LV stiffness	Ca	Contr. RV	MV close area	AV open area	Q_E	RPM
1	100	0.76	0.115	0.8	0.054	1.23	0.6	0	2	2.1	2500
2	100	0.76	0.115	0.8	0.054	1.23	0.6	0	1.3	2.1	2500
3	100	0.76	0.115	0.8	0.054	1.23	0.6	0	0.8	2.1	2500

MR	HR	SVR	PVR	Contr. LV	LV stiffness	Ca	Contr. RV	MV close area	AV open area	Q_E	RPM
1	100	0.76	0.115	0.8	0.054	1.23	0.6	0.1	5	2.1	2500
2	100	0.76	0.115	0.8	0.054	1.23	0.6	0.3	5	2.1	2500
3	100	0.76	0.115	0.8	0.054	1.23	0.6	0.5	5	2.1	2500

B Results for left ventricular flow calculations in cardiovascular simulators

Table 10: Results of LV flow calculations from data obtained from the UT simulator.

Baseline	nRMSE	SV original [mL]	SV WK model [mL]	SV error [mL]	SV error [%]
1	0.2	29.7	32.8	3.1	10.4

R and C	nRMSE	SV original [mL]	SV WK model [mL]	SV error [mL]	SV error [%]
1	0.2	33.4	36.8	3.5	10.3
2	0.2	28.8	31.3	2.5	8.8
3	0.2	22.9	25.3	2.5	10.9
4	0.2	19.3	21.5	2.2	11.5
5	0.1	28.3	31.4	3.0	10.7
6	0.1	26.8	29.7	3.0	11.1
7	0.2	30.4	33.5	3.1	10.1
8	0.2	30.7	33.7	3.1	10.0
9	0.2	31.8	35.2	3.4	10.6
10	0.2	21.9	24.4	2.5	11.3

HR	nRMSE	SV original [mL]	SV WK model [mL]	SV error [mL]	SV error [%]
1	0.2	41.3	48.2	6.9	16.7
2	0.1	41.4	46.6	5.2	12.4
3	0.1	34.6	38.4	3.8	10.9
4	0.2	25.4	28.3	2.9	11.5
5	0.2	20.4	23.6	3.2	15.7

RV	nRMSE	SV original [mL]	SV WK model [mL]	SV error [mL]	SV error [%]
1	0.2	29.4	32.6	3.2	10.8
2	0.2	28.7	32.1	3.5	12.0
3	0.2	26.1	30.4	4.3	16.3

AS	nRMSE	SV original [mL]	SV WK model [mL]	SV error [mL]	SV error [%]
1	0.1	28.4	31.4	3.0	10.5
2	0.1	26.5	29.3	2.9	10.9
3	0.1	25.2	28.0	2.8	11.1

MR	nRMSE	SV original [mL]	SV WK model [mL]	SV error [mL]	SV error [%]
1	0.2	27.8	30.8	3.0	10.7
2	0.2	26.7	29.6	2.9	10.9
3	0.2	18.6	20.9	2.4	12.7

Table 11: Results of LV flow calculations from data obtained from the UT simulator using constant ECMO flow.

Baseline	nRMSE	SV original [mL]	SV WK model [mL]	SV error [mL]	SV error [%]
1	0.2	29.7	32.8	3.1	10.4

R and C	nRMSE	SV original [mL]	SV WK model [mL]	SV error [mL]	SV error [%]
1	0.2	33.4	36.8	3.5	10.4
2	0.2	28.8	31.3	2.5	8.9
3	0.2	22.9	25.3	2.5	10.9
4	0.2	19.3	21.5	2.2	11.5
5	0.2	28.3	31.4	3.0	10.7
6	0.2	26.8	29.7	3.0	11.1
7	0.2	30.4	33.5	3.1	10.2
8	0.2	30.7	33.7	3.1	10.0
9	0.2	31.8	35.2	3.4	10.6
10	0.2	21.9	24.4	2.5	11.3

HR	nRMSE	SV original [mL]	SV WK model [mL]	SV error [mL]	SV error [%]
1	0.2	41.3	48.2	6.9	16.8
2	0.2	41.4	46.6	5.2	12.5
3	0.2	34.6	38.4	3.8	11.0
4	0.2	25.4	28.3	2.9	11.5
5	0.2	20.4	23.6	3.2	15.7

RV	nRMSE	SV original [mL]	SV WK model [mL]	SV error [mL]	SV error [%]
1	0.2	29.4	32.6	3.2	10.8
2	0.2	28.7	32.1	3.5	12.1
3	0.2	26.1	30.4	4.3	16.3

AS	nRMSE	SV original [mL]	SV WK model [mL]	SV error [mL]	SV error [%]
1	0.2	28.4	31.4	3.0	10.6
2	0.1	26.5	29.3	2.9	10.9
3	0.1	25.2	28.0	2.8	11.2

MR	nRMSE	SV original [mL]	SV WK model [mL]	SV error [mL]	SV error [%]
1	0.2	27.8	30.8	3.0	10.7
2	0.2	26.7	29.6	2.9	10.9
3	0.2	18.6	20.9	2.4	12.8

Table 12: Results of LV flow calculations from data obtained from the Harvi simulator.

Baseline	nRMSE	SV original [mL]	SV WK model [mL]	SV error [mL]	SV error [%]
1	1.6	33.2	33.8	0.6	1.9

R and C	nRMSE	SV original [mL]	SV WK model [mL]	SV error [mL]	SV error [%]
1	1.5	35.8	35.5	-0.3	-0.9
2	1.2	43.2	44.3	1.1	2.6
3	1.9	25.7	25.9	0.1	0.6
4	2.1	21.8	21.8	0.1	0.3
5	1.0	31.7	32.2	0.5	1.7
6	0.7	30.6	31.1	0.5	1.5
7	2.3	33.4	34.1	0.7	2.1
8	2.6	31.3	32.0	0.7	2.2
9	0.9	33.2	32.3	-0.9	-2.7
10	1.2	24.8	25.0	0.2	0.8

HR	nRMSE	SV original [mL]	SV WK model [mL]	SV error [mL]	SV error [%]
1	1.7	35.4	32.4	-3.0	-8.5
2	1.5	36.7	35.9	-0.8	-2.2
3	1.5	36.5	37.1	0.6	1.6
4	1.8	26.7	27.6	0.8	3.2
5	2.0	25.5	27.4	1.9	7.3

RV	nRMSE	SV original [mL]	SV WK model [mL]	SV error [mL]	SV error [%]
1	1.6	32.5	33.4	0.8	2.6
2	1.7	31.8	33.1	1.3	4.2
3	1.8	28.9	32.3	3.5	12.0

AS	nRMSE	SV original [mL]	SV WK model [mL]	SV error [mL]	SV error [%]
1	1.6	33.2	33.9	0.7	2.0
2	0.6	32.6	32.2	-0.4	-1.1
3	0.5	28.4	27.7	-0.7	-2.6

MR	nRMSE	SV original [mL]	SV WK model [mL]	SV error [mL]	SV error [%]
1	1.6	31.0	31.6	0.6	1.9
2	1.9	23.5	23.1	-0.4	-1.7
3	2.3	17.4	16.5	-0.9	-5.2

Table 13: Results of LV flow calculations from data obtained from Aplysia.

Baseline	nRMSE	SV original [mL]	SV WK model [mL]	SV error [mL]	SV error [%]
1	1.5	32.2	39.6	7.4	22.9

R and C	nRMSE	SV original [mL]	SV WK model [mL]	SV error [mL]	SV error [%]
1	1.2	37.6	49.9	12.3	32.7
2	1.2	37.8	54.1	16.3	43.1
3	1.9	27.0	31.4	4.5	16.5
4	2.1	24.4	27.6	3.2	13.0
5	1.3	32.3	38.5	6.2	19.2
6	1.2	31.8	36.9	5.2	16.3
7	1.7	31.9	40.1	8.3	25.9
8	1.9	31.8	40.7	8.9	28.1
9	1.1	37.0	46.3	9.3	25.2
10	1.7	26.8	30.8	4.0	14.9

HR	nRMSE	SV original [mL]	SV WK model [mL]	SV error [mL]	SV error [%]
1	1.1	42.0	64.0	22.0	52.5
2	1.1	41.2	55.5	14.3	34.7
3	1.3	36.0	45.7	9.6	26.7
4	1.6	28.8	34.5	5.7	19.6
5	1.7	25.7	30.3	4.7	18.1

RV	nRMSE	SV original [mL]	SV WK model [mL]	SV error [mL]	SV error [%]
1	1.5	30.7	38.5	7.8	25.2
2	1.5	28.8	36.7	7.9	27.2
3	1.5	22.7	31.6	8.9	39.3

AS	nRMSE	SV original [mL]	SV WK model [mL]	SV error [mL]	SV error [%]
1	1.5	31.8	39.1	7.3	23.1
2	1.5	30.5	38.2	7.6	25.0
3	1.5	27.8	35.6	7.8	27.9

MR	nRMSE	SV original [mL]	SV WK model [mL]	SV error [mL]	SV error [%]
1	1.5	30.7	38.2	7.5	24.4
2	1.4	27.9	35.6	7.8	28.0
3	1.4	25.3	33.6	8.4	33.1

C Results for compliance estimations in cardiovascular simulators

Table 14: The original compliance C_{or}, the compliance determined using the adapted time-decay method C_{decay} and $\Delta C = C_{decay} - C_{or}$ for the UT simulator, the UT simulator with constant ECMO flow (UTc), the Harvi simulator and Aplysia in mL/mmHg.

UT			UTc			Harvi			Aplysia		
C_{or}	C_{decay}	ΔC	C_{or}	C_{decay}	ΔC	C_{or}	C_{decay}	ΔC	C_{or}	C_{decay}	ΔC
1.21	1.28	0.07	1.21	1.31	0.10	1.2	1.25	0.05	1.23	1.84	0.61
1.21	1.28	0.07	1.21	1.31	0.10	1.2	1.17	-0.03	1.23	2.91	1.68
1.21	1.26	0.05	1.21	1.28	0.07	1.2	1.19	-0.01	1.23	3.85	2.62
1.21	1.30	0.09	1.21	1.32	0.11	1.2	1.25	0.05	1.23	1.40	0.17
1.21	1.31	0.10	1.21	1.33	0.12	1.2	1.25	0.05	1.23	1.28	0.04
0.85	0.90	0.05	0.85	0.92	0.07	0.8	0.86	0.06	0.88	1.52	0.64
0.61	0.64	0.04	0.61	0.66	0.06	0.6	0.67	0.07	0.62	0.97	0.35
1.57	1.67	0.10	1.57	1.70	0.13	1.6	1.63	0.03	1.56	2.39	0.83
1.82	1.93	0.12	1.82	1.96	0.15	1.8	1.82	0.02	1.92	2.67	0.75
0.85	0.90	0.05	0.85	0.92	0.07	0.8	0.79	-0.01	0.88	1.62	0.75
0.85	0.90	0.05	0.85	0.93	0.08	0.8	0.86	0.06	0.85	1.15	0.30
1.21	1.34	0.13	1.21	1.37	0.16	1.2	1.09	-0.11	1.23	2.53	1.29
1.21	1.32	0.11	1.21	1.33	0.12	1.2	1.18	-0.02	1.23	2.21	0.97
1.21	1.32	0.11	1.21	1.34	0.13	1.2	1.23	0.03	1.23	2.11	0.87
1.21	1.30	0.09	1.21	1.32	0.11	1.2	1.27	0.07	1.23	1.88	0.65
1.21	1.36	0.15	1.21	1.37	0.16	1.2	1.25	0.05	1.23	1.87	0.64
1.21	1.29	0.08	1.21	1.32	0.11	1.2	1.25	0.05	1.23	1.99	0.75
1.21	1.30	0.09	1.21	1.33	0.12	1.2	1.27	0.07	1.23	1.90	0.67
1.21	1.35	0.14	1.21	1.38	0.17	1.2	1.38	0.18	1.23	2.15	0.92
1.21	1.29	0.08	1.21	1.31	0.10	1.2	1.25	0.05	1.23	1.87	0.64
1.21	1.29	0.08	1.21	1.32	0.11	1.2	1.25	0.05	1.23	1.98	0.75
1.21	1.29	0.08	1.21	1.32	0.11	1.2	1.23	0.03	1.23	2.00	0.77
1.21	1.29	0.08	1.21	1.32	0.11	1.2	1.24	0.04	1.23	1.97	0.74
1.21	1.29	0.08	1.21	1.32	0.11	1.2	1.21	0.01	1.23	2.13	0.90
1.21	1.31	0.10	1.21	1.34	0.13	1.2	1.15	-0.05	1.23	2.08	0.85

D Effects of changing parameters in cardiovascular simulators

(a) Resistance

(b) Compliance

(c) Heart rate

(d) Right ventricular function

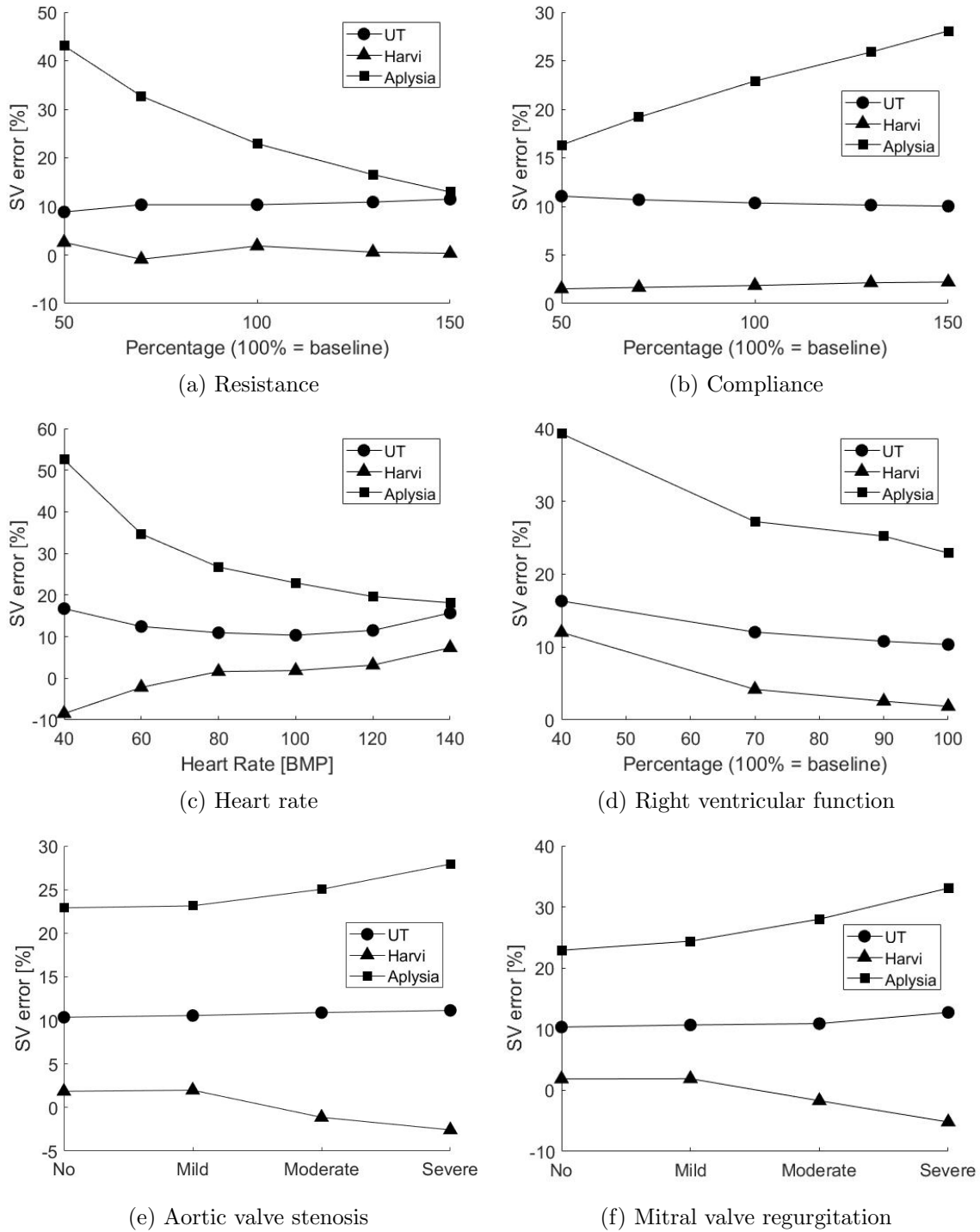(e) Aortic valve stenosis

(f) Mitral valve regurgitation

Figure 24: Change in SV error [%] due to changes in parameters in the three different cardiovascular simulators.

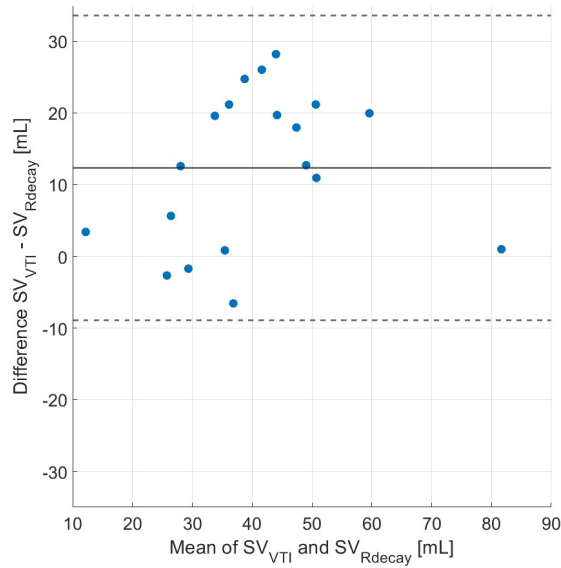## E   Left ventricular flow calculations using R_{decay} and C_{echo}

Figure 25: Bland-Altman plot, the solid line indicating the mean difference, the dashed line the limits of agreement. Shows the agreement between SV_{VTI} and SV_{Rdecay} with a mean difference of 12.36 mL and limits of agreement of -8.89 and 33.60 mL.

F   Resistance estimated with the adapted time-decay method using C_0
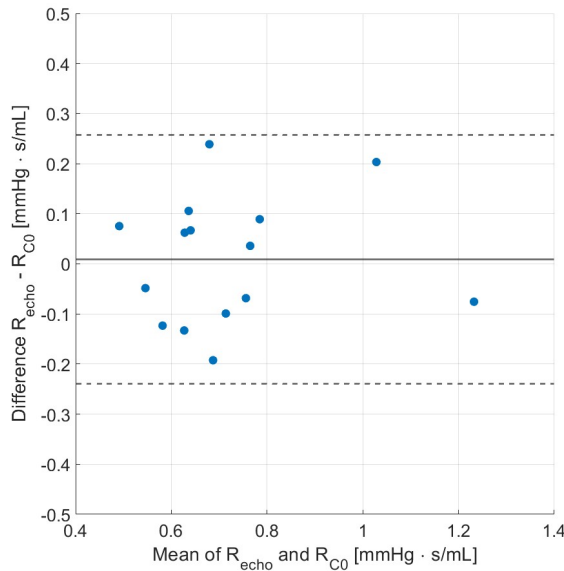

Figure 26: Bland-Altman plot, the solid line indicating the mean difference, the dashed line the limits of agreement. Shows the agreement between R_{echo} and R_1, determined with the adapted time-decay method, using C_0. With a mean difference of 0.01 mmHg·s/mL and limits of agreement of -0.24 and 0.26 mmHg·s/mL.